EMPLACEMENT STYLES OF OBSIDIAN LAVAS: AN INTEGRATED FIELD AND LABORATORY STUDY

A Dissertation

presented to

the Faculty of the Graduate School

at the University of Missouri-Columbia

In Partial Fulfillment

Of the Requirements for the Degree

Doctor of Philosophy

---

by

STUART M. KENDERES

Dr. Alan Whittington, Dissertation Supervisor

JULY 2021

The undersigned, appointed by the dean of the Graduate School, have examined the dissertation entitled

EMPLACEMENT STYLES OF OBSIDIAN LAVAS:
AN INTEGRATED FIELD AND LABORATORY STUDY

Presented by Stuart M. Kenderes,

a candidate for the degree of doctor of philosophy,

and hereby certify that, in their opinion, it is worthy of acceptance.

Dr. Alan G. Whittington

Dr. Francisco Gomez

Dr. John Huntley

Dr. Eric Sandvol

Dr. Thomas Sewell

Acknowledgements

Financial support for the dissertation was provided by the National Science Foundation (NSF) award number EAR 1724581, the American Chemical Society, and the Department of Geological Sciences at the University of Missouri.

I would also like to thank my current and previous committee members for their feedback and encouragement through my graduate exams and hours spent discussing research including Drs. Alan G. Whittington, Paco Gomez, John Huntley, Eric Sandvol, Kevin Shelton, Jeff Ferguson, and Tommy Sewell. I would also like to thank additional current and former faculty members in the Department of Geological Sciences including Miriam Barquero-Molina, Drs. Peter Nabelek, Martin Appold, Cheryl Kelley, Ken MacLeod, Jim Schiffbauer, Bob Bauer, and Mike Underwood. Lastly, I would like to thank external collaborators who I have supplemented the expertise in my department including Drs. Kenny Befus (BU) and Graham D.M. Andrews (WVU), as well as graduate students Shelby Isom (WVU), Tyler N. Leggett (BU), and Jean Marie-Prival (Claremont-Ferand).

Table of Contents

List of Tables

List of Figures

Abstract

Previously accepted models of emplacement dynamics of obsidian lavas have recently been called into question by observations made during the effusive eruptions of Chaitén in 2008-2009 and Cordón Caulle in 2011-2012 in Chile. The eruption of Chaitén was characterized by two distinct styles of emplacement, with the transition between the two resulting in hazardous block and ash flows and periods of dome collapse. Cordón Caulle erupted an obsidian coulée that exhibited behaviors typically associated with eruptions of more mafic lavas such as inflation and advancement via break-out lobe development.

Lava emplacement styles are controlled by the physical properties of the lava which are a function of composition, temperature, and time. Banco Bonito lava, Valles caldera, NM, and Obsidian Dome, Inyo Craters, Long Valley, CA are like the lavas from Cordón Caulle and Chaitén respectively and were the subject of scientific research drilling in the 1980's, providing spatially well-constrained samples that can be used to measure residual water concentrations, thermal histories, and apparent viscosities. These three datasets are then used to infer emplacement behaviors of Banco Bonito and Obsidian Dome.

Thermal histories of obsidian lavas can be constrained experimentally using relaxation geospeedometry. Previous applications of the method used up to five isobaric heat capacity measurements per quantitative cooling rate, requiring multiple days of laboratory work. We present a Monte Carlo inspired numerical solver capable of identifying comparable natural cooling rates using a single experimental measurement.

Preface

This dissertation includes three complementary chapters and one supplemental project. All chapters were written as manuscripts to be submitted for publication with one having been published so far. I am the primary author of all four chapters and will describe the contributions of others in detail below.

Chapter one describes the first attempt to model the viscosity of honey using configurational entropy theory (Adam and Gibbs, 1965). My contribution includes writing and revising the manuscript, performing quantitative isobaric heat capacity measurements, and modeling the resulting data. Other contributors include Alan Whittington and Aaron Morrison. Alan contributed to writing the manuscript including revision, and Aaron performed experimental viscosity measurements as well as providing written feedback on the manuscript.

Chapter two was conceived of and completed entirely during the COVID-19 pandemic and details an improved methodology for implementing relaxation geospeedometry for the purpose of determining natural cooling rates of volcanic glasses. I am responsible for all experimental measurements, numerical modeling, and algorithm development. I am also the primary author of the work with feedback from Alan G. Whittington on writing. A version of the chapter was recently published in *Chemical Geology* and is reproduced here with permission from Elsevier.

Chapter three classifies the likely emplacement style of Banco Bonito lava, Valles caldera, New Mexico. I am responsible for a majority of experimental measurements including FTIR and DSC for samples from Banco Bonito. I am also the primary author

with contributions from Drs. Alan Whittington and Kenny Befus. Alan is also responsible for approximately five DSC measurements included in the final draft. Additional experimental measurements for the VC-1 Rhyolite were conducted by undergraduate student Lexie Bryson under my supervision.

Chapter four explores the emplacement history of Obsidian Dome, Inyo Craters, Long Valley, California. I am the primary author of the work, and responsible for all experimental measurements, data analysis, and numerical modeling. Dr. Alan Whittington has provided some feedback on the manuscript.

Chapter 1

1. Introduction

Some of the largest explosive volcanic eruptions in the geologic record originated from rhyolite magmas. Reconciling the observation that rhyolitic magmas can also *sometimes* generate effusive lavas, has puzzled volcanologists for decades. The 2008-2009 eruption of Chaitén volcano in Chile reminded the world how hazardous rhyolitic eruptions can be (Carn et al., 2009). The volcano experienced little precursor activity and a highly mobilized magma ascended the conduit in ~4 hours (Castro and Dingwell, 2009). The eruption was designated a 5 on the volcanic explosivity index (VEI) and surprised many since its most recent previous eruption occurred ~9400 years ago. The explosive phase waned, and a lava dome began growing in the crater. The lava dome experienced two distinct styles of emplacement. The first style can be described as exogenous or "tank-tread" and is characterized by younger lava being emplaced on top of older lava and requires that the effusion rate of the magma exceeds the cooling rate of the crust. Next a spine was extruded before the style shifted to what is described as endogenous emplacement. This style is characterized by younger lava intruding older lava, and typically occurs when effusion rates are slower than cooling rate of the crust.

A second eruption of rhyolitic magma occurred in Chile at Puyehue-Cordón Caulle in 2011-2012 which also exhibited limited precursor activity and was classified as VEI 4 (Castro et al., 2013). Again, an explosive phase was followed by effusion of a crystal-poor lava. Two observations were made during the eruption that challenged previously accepted ideas regarding eruptions of rhyolite magmas. First, explosive and effusive behavior were observed simultaneously instead of as two distinct eruptive phases (Schipper et al., 2013). Second, the emplacement behaviors of the effusive lava were more like those expected during eruptions of basaltic lava than rhyolite lava (Tuffen et al., 2013). Observed emplacement behaviors included advancement primarily by development of break out lobes (Magnall et al., 2018) and inflation of up to 40 m presumably by the intrusion of younger lava behind the stalled flow front (Farquharson et al., 2015).

The transition between emplacement styles at Chaitén (2008-2009) and previously unobserved emplacement behaviors of silicic lavas at Cordón Caulle are controlled by changes in lava rheology. We can infer the emplacement behaviors of older lavas by understanding how their rheology varies as a function of time, temperature, and composition. Many examples of crystal poor, rhyolite lavas are preserved around the world, but two are unique in that they have been the subject of scientific drilling which has sampled their entire thickness (Eichelberger et al., 1985; Goff et al., 1986).

The first is Obsidian Dome, which is the youngest and largest of several rhyolite lavas in the Inyo Craters, Long Valley, CA. Obsidian Dome is an exceptionally well-studied pancake lava dome that is similar in composition, morphology, and volume to the lava erupted at Chaitén in 2008-2009. Two drill cores collected at Obsidian Dome

sampled the entire thickness, providing spatially well constrained samples both proximal and distal to the vent.

The second is Banco Bonito, the youngest eruptive unit of the El Cajete series from Valles caldera, NM. Banco Bonito is a coulée and is comparable in morphology, volume, and composition to the lava produced during the most recent eruption of Cordón Caulle. The VC-1 drill core sampled the entire thickness of the flow near the western flow margin.

Together these two lavas function as historical case studies to compare to the observations made at Chaitén and Cordón Caulle, whose interiors remain inaccessible.

1.1 Dissertation Structure

The first chapter of this dissertation describes our attempts at applying configurational entropy modeling to describe the temperature dependence of the viscosity of honey. Honey is an excellent analogue material for the study of lava rheology. Honey can crystallize and its viscosity is dependent on dissolved water content just like lava, and comparable viscosities are in a much more accessible temperature range.

The second chapter describes a methodological development made by applying Monte Carlo methods to the Tool-Narayanaswamy geospeedometer for the purpose of determining the natural cooling rate of volcanic glasses. The last two chapters describe case studies of preserved obsidian lava flows that have similar morphologies to those erupted in Chile. Obsidian Dome is comparable to the lava dome at Chaitén from 2008-2009 and Banco Bonito is comparable to the lava at Cordón Caulle from 2011-2012.

Chapter 2

2. A configurational entropy viscosity model for honey with non-Arrhenian behavior

2.1 Abstract

Empirical models including the Williams-Landel-Ferry and Vogel-Fulcher-Tammann equations are often used to understand the effect of temperature on the non-Arrhenian viscosity of honey. Empirical equations can reproduce experimental data with high precision, however empirical model constants often lack a physical meaning, and are less reliable when extrapolating beyond the calibration data set. Configurational entropy modeling using Adam-Gibbs relaxation theory is based in thermodynamics and provides an alternative method to solve for the viscosity of liquids as a function of temperature. We have measured the viscosity and isobaric heat capacity of a clover honey using rotational and oscillatory parallel-plate viscometry and differential scanning calorimetry. The honey viscosity decreased from 1400 Pa s at −5 °C to 4 Pa s at +35 °C at an angular frequency of 1 rad s^{-1}, exhibiting Newtonian behavior. The glass transition was −40.0˚C, where the heat capacity increased from 1.2 to 2.2 J g^{-1} K^{-1}. Experimental viscosity data were reproduced using configurational entropy modeling with a relative uncertainty of

~5%, comparable to leading empirical equations. Advantages of configurational entropy modeling include improved reliability when extrapolating beyond the calibration data set, fewer adjustable parameters than some other models, and the ability to reproduce non-Arrhenian behavior.

2.2 Introduction

Viscosity is an important physical property that controls how honey is extracted from the comb, processed industrially, and stored for consumption (White, 1978). Moisture content (Chataway, 1932; Lothrop, 1939; Munro, 1943; Lazaridou, 2004; Yanniotis et al., 2006), composition (Chirife and Buera, 1997; Oroian et al., 2013), and temperature (Munro, 1943; White, 1975; Junzheng and Changying, 1998) are the dominant variables affecting the liquid viscosity of honey. Measuring the viscosity of each variety of honey can be time consuming, and expensive. Therefore, equations that describe the liquid viscosity of honey as a function of temperature, composition, and moisture content are needed.

2.2.1 Viscosity modeling theory

The Arrhenius equation is commonly used to model the effects of temperature on the viscosity (η) of liquids, including honey (Junzheng and Changying, 1998; Mossel, 2000; Zaitoun et al., 2001; Lazaridou, 2004; Recondo et al., 2006; Telis, 2007; Cohen, 2010; Oroian, 2013; Al-Mahasneh et al., 2014; da Silva, 2017). The Arrhenius equation has a theoretical basis, with two adjustable model parameters:

$$\log_{10} \eta = \log_{10} A_{Arr} + \frac{E_a}{2.303RT} \qquad 2.1$$

where A_{Arr} corresponds to the viscosity intercept at infinite temperature, and the slope of the line is directly related to the activation energy (E_a) required for viscous flow. However, honey does not exhibit Arrhenian behavior (i.e., a linear relationship in log viscosity vs. inverse temperature space) over wide temperature ranges. Therefore, other equations that permit non-Arrhenian behavior are often used. The Vogel-Fulcher-Tammann equation (VFT; Vogel 1921; Fulcher, 1925; Tammann and Hesse, 1926):

$$\log_{10}\eta = log_{10}A_{VFT} + \frac{B_{VFT}}{T - C_{VFT}} \tag{2.2}$$

and Williams-Landel-Ferry equation (WLF; Williams et al., 1955):

$$\log_{10}\eta = log_{10}A_{WLF} - \frac{B_{WLF}(T - T_g)}{D_{WLF} + B_{WLF}(T - T_g)} \tag{2.3}$$

are empirical equations that have been used to model the temperature dependence of the viscosity of honey (e.g., Soesanto and Williams, 1981; Mossel, 2000; Rampp et al., 2000; Sopade, 2002; Recondo et al., 2006; Oroian, 2013; da Silva, 2017). Angell (1997) and Peleg (2017) show the WLF and VFT equations to be mathematically equivalent in fitting viscosity data. Two advantages of the VFT and WLF equations are that they can reproduce the observed non-Arrhenian temperature-dependence of honey viscosity. One disadvantage is that the adjustable model parameters do not have a direct physical meaning that can help explain behaviors observed in experimental viscosity data.

The Adam-Gibbs relaxation theory (Adam and Gibbs, 1965) was used by Richet (1984) to derive an equation relating viscosity and configurational entropy (S^{conf}), that has been widely used in the silicate melt and glass science literature (e.g., Richet, 1984; Neuville and Richet, 1991; Toplis et al., 1997; Sehlke and Whittington, 2016; Robert et al., 2019) to model the relationship between temperature and viscosity for silicate melts of different compositions. The basic form of the Adam-Gibbs (AG) equation is:

$$log_{10}\,\eta = log_{10}A_{AG} + \frac{B_{AG}}{TS^{conf}(T)} \quad 2.4$$

where, A_{AG} is the viscosity intercept at infinite temperature, B_{AG} is the pseudo-activation energy of shear viscosity (Toplis, 1998), T is temperature, and S^{conf} is derived from the isobaric heat capacities of the glass (C_{Pg}) and liquid (C_{Pl}) through the equations:

$$S^{conf}(T) = S^{conf}(T_g) + \int_{T_g}^{T} \frac{C_P^{conf}}{T} dT \quad 2.5$$

and

$$C_P^{Conf} = C_{Pl} - C_{Pg}(T_g) \quad 2.6$$

where T_g refers to the temperature of the glass transition of the material in Kelvin, and C_P^{conf} is the configurational heat capacity. For congruently melting compounds whose heat capacity and glass transition temperatures are known, there are only two adjustable parameters: A_{AG} and B_{AG}. If a material is incongruently-melting, we can treat $S^{conf}(T_g)$ as

a third adjustable model parameter. Because S^{conf} increases with temperature, non-Arrhenian behavior follows automatically. So-called "fragile" liquids have large configurational heat capacities and rapid increases in S^{conf} with T, leading to markedly non-Arrhenian behavior, which is the case for most organic liquids (Angell, 1995). Stronger liquids have smaller configurational heat capacities and slower increases in S^{conf} with T, with pure SiO_2 being the archetypal "strong" liquid (Urbain et al., 1982). Most honeys go through the glass transition around −40°C, meaning that C_{Pg}, C_{Pl} and T_g can be readily measured using differential scanning calorimetry (DSC; Sopade et al., 2002).

Mauro et al., (2009) present a modified version of the AG equation, hereafter referred to as the MYEGA equation:

$$log_{10}\eta(T) = log_{10}A_{MY} + \left(log_{10}\eta_{T_g} - log_{10}A_{MY}\right) \frac{T_g}{T} exp\left[\left(\frac{m}{log_{10}\eta_{T_g} - log_{10}A_{MY}} - 1\right)\left(\frac{T_g}{T} - 1\right)\right] \quad 2.7$$

where A_{MY} is again the viscosity intercept at infinite temperature, m is the fragility of the liquid, T_g is the glass transition temperature in K, and η_{Tg} is the viscosity of the liquid at T_g. The fragility of the melt is described as the gradient of the $\eta(T)$ curve when $T = T_g$ by the equation (Angell, 1995):

$$m = \left.\frac{\partial log_{10}\eta(T)}{\partial\left(T_g/T\right)}\right|_{T=T_g} \quad 2.8$$

where m is the fragility, and $\eta(T_g) = 10^{12}$ Pa s (Yue, 2009). The main advantage of the MYEGA equation over the original formulation is that quantitative C_P measurements to determine $C_P^{Conf}(T)$ are no longer required. Both theoretically based models provide additional confidence in extrapolating the model outside the temperature range of the calibration dataset. Connecting viscosity to thermodynamics can lead to the development of a unified viscosity model for honey as a function of temperature (T) and composition (X). Below we present the first attempt, to our knowledge, that uses the S^{conf} theory in the form of the AG and MYEGA equations to describe the temperature-viscosity relationship for the non-Arrhenian behavior of honey.

2.3 Materials & Methods

2.3.1 Sample

The sample honey used in this study is store-brand clover honey from a local supermarket (Hy-Vee® brand). The primary purpose of our study is to model the relationship between temperature and the liquid viscosity of honey. Therefore, the effects of variable moisture content, composition, and crystallization were not considered.

2.3.2 Differential scanning calorimetry

Quantitative isobaric heat capacity (C_P) measurements were made using a Perkin Elmer DSC 8500 differential scanning calorimeter fitted with an intracooler II, that works on the power-compensation principle. The operational temperature range of the

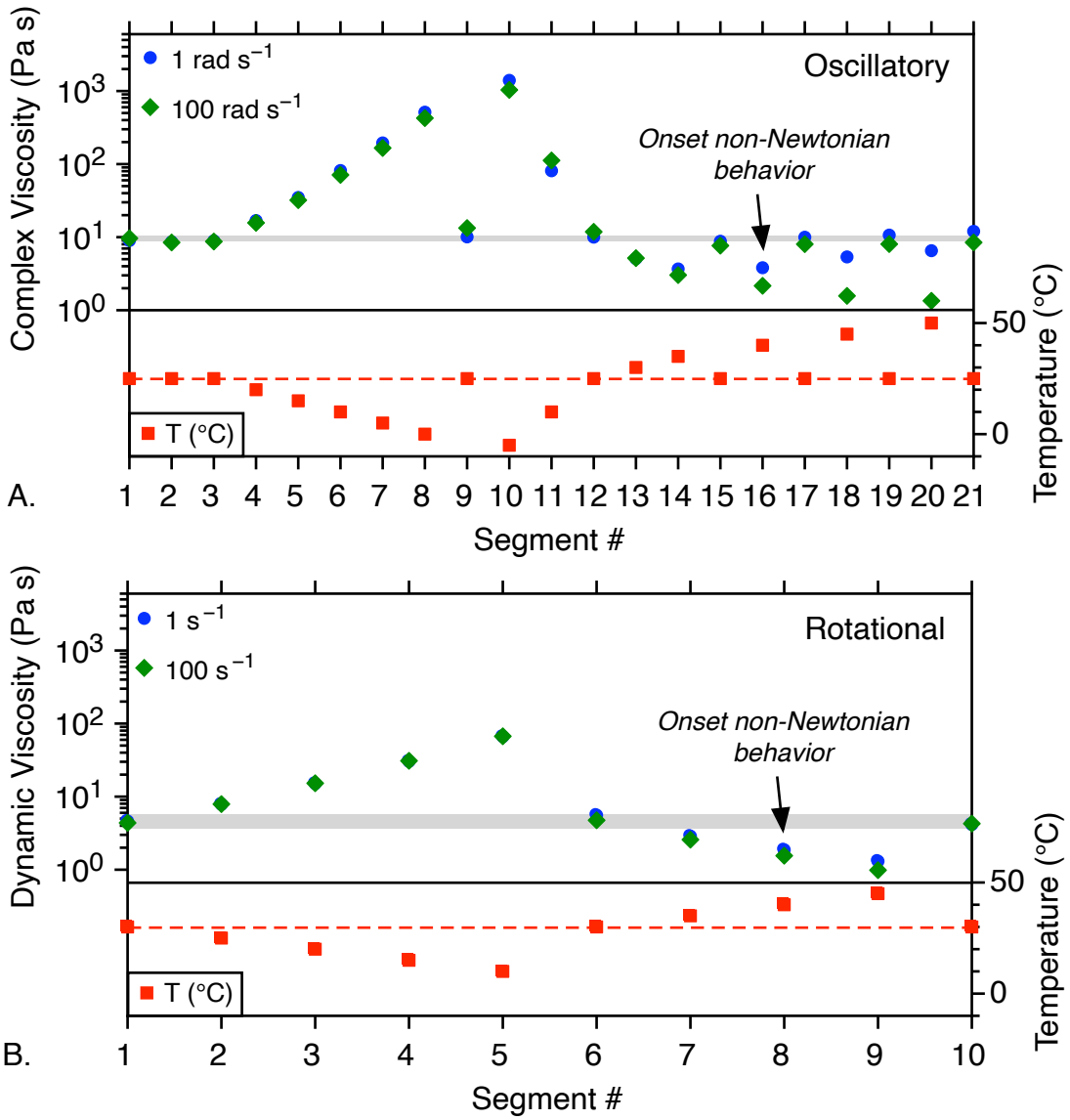

Figure 2.1 Temperature-time profile for experimental viscosity measurements (red squares) of (A) oscillatory and (B) rotational viscosity measurement segments. (A) Complex viscosities (η*) when ω = 1 rad s⁻1 (blue circles) and ω = 100 rad s⁻1 (green diamonds) shows consistent Newtonian behavior until segment 16. (B) Dynamic viscosities (η) when $\dot{\gamma}$ = 1 s⁻1 (blue circles) and $\dot{\gamma}$ = 100 s⁻1 (green diamonds) shows consistent Newtonian behavior until segment 8, again at high temperature. Dashed red lines and gray boxes correspond to oscillatory (25°C) and rotational (30°C) measurements used to monitor for sample changes during measurement.

instrument is from −70°C to 750°C. The calorimeter was calibrated using the melting points and enthalpies of fusion of In and Zn metals. We used 25 μL volatile aluminum sample pans, and temperature scanning rates of 20°C min^{-1}. Pure sapphire (Al_2O_3) was used as the heat capacity reference (Ditmars et al., 1982).

Table 2.1 Experimental isobaric heat capacity values of honey used in S^{conf} modeling.

Temperature (T)		Heat Capacity (C_P)
°C	K	J mol^{-1} K^{-1}
Liquid C_P		
50.0	323.2	335.9
40.0	313.2	325.2
30.0	303.2	317.6
20.0	293.2	310.9
10.0	283.2	304.5
0.0	273.2	298.4
–10.0	263.2	292.2
–20.0	253.2	286.3
–30.0	243.2	286.1
–40.0	233.2	222.7*
Glass C_P		
–50.0	223.2	160.5
–55.0	218.2	153.3
–60.0	213.2	148.5

*Corresponds with the measured T_g

2.3.3 Rheology

The viscosity of the honey was measured using an Anton-Paar MCR-302 rheometer. A Peltier plate heating device (with hood) was used to control temperature to ±0.1°C within the device. A cone-and-plate measuring device was used to maintain constant shear across the diameter of the sample. The steel cone was 50 mm in diameter with a 0.5° angle and the bottom plate was quartz glass. Viscosity was measured in both

oscillatory and rotational modes. Oscillatory measurements produce complex viscosity (η*) data which can be converted to dynamic viscosity (η) by the Cox-Merz rule $\eta(\dot{\gamma})=\eta^*(\omega)$ (Cox and Merz, 1958; Milner, 1996).

Oscillatory measurements were made across 21 isothermal measurement segments (Fig. 2.1A) using angular frequencies (ω) from 0.5 rad s^{-1} to 100 rad s^{-1}. Oscillatory measurements are made using finite strains <5%, allowing measurements to be made over a wider temperature range (−5 °C to 50°C). Nine interspersed measurements at 25°C were made to monitor for compositional and textural changes in the sample over the course of the measurement.

Ten isothermal temperature segments (Fig. 2.1B) were measured in rotational mode at strain rates ($\dot{\gamma}$) of 0.1 s^{-1} to 100 s^{-1}. Three interspersed measurements made at 30°C were again used to monitor the sample for changes during the measurement.

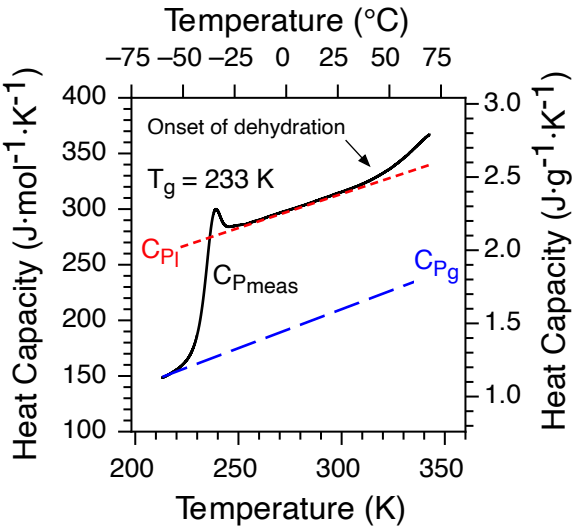

Figure 2.2. Isobaric heat capacity vs. temperature for honey sample from −60°C to 70°C, with an observed T_g at −40°C or 233 K. The temperature dependence of the C_P of the liquid (C_{Pl}; short red dash) is modeled using equation 2.10, and the C_P of the glass (C_{Pg}; long blue dash) is modeled using equation 2.9.

Rotational measurements require infinite relative strains, which can only be achieved at higher temperatures from 10 °C to 45°C.

2.3.4 Uncertainty estimates

Confidence intervals (2σ; 95%) were determined using bootstrap resampling techniques, where the experimental data were randomly resampled 1000 times before fitting equations (2.1), (2.2), (2.4)-(2.6), and (2.7). Confidence intervals are shown as shaded regions in figure 4.

2.4 Results

2.4.1 Isobaric heat capacity

Heat capacity of the honey was measured from −63°C to +70˚C. The C_{Pg} of the honey increased with increasing temperature from −63 to −50˚C and was fitted to the Maier-Kelley equation (Maier and Kelley, 1932). The resulting fit is:

$$C_{P,\mathrm{g}} = 1.0\times10^{-5} + 0.70T + 99.93T^{-2} \qquad 2.9$$

where C_{Pg} is in J mol^{-1} K^{-1}, and T is temperature in Kelvin. The molar mass of the honey was calculated to be 131 g mol^{-1}, by assuming its composition was ~30 wt.% H_2O, with the remaining ~70 wt.% comprised of fructose and glucose, which both have molar masses of 180.15 g mol^{-1}. The root-mean-squared deviation (RMSD) of the fit is 1.7 J mol^{-1}K^{-1}, or about 1% relative. Between −50°C and −27˚C, the heat capacity increases dramatically, reflecting the glass transition (T_g), and was identified using the half-height

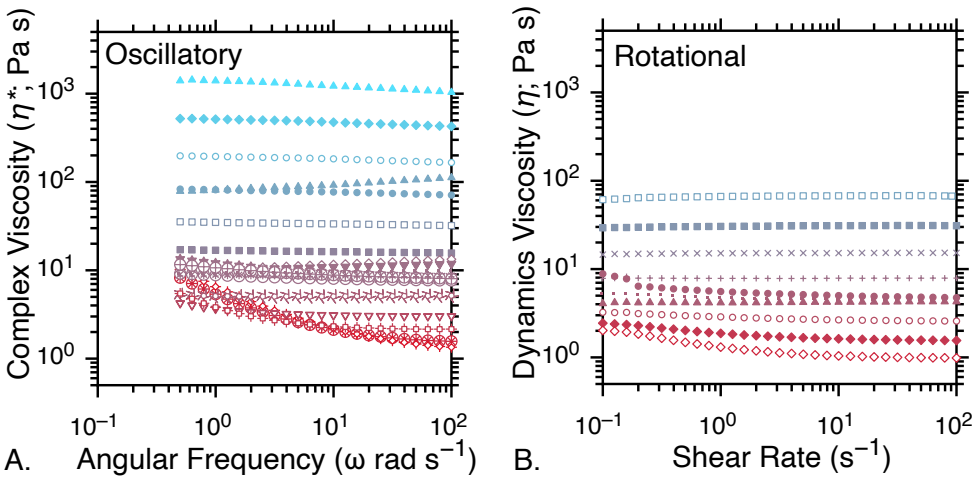

Segment #	1	2	3	4	5	6	7	8	9	10	11	12	13	14	15	16	17	18	19	20	21
Oscillatory	·	+	×	■	□	●	○	◆	◇	◂	◃	▸	✲	▹	⊙	✲	⌑	❋	⊕	✧	✸
Temp. °C	25	25	25	20	15	10	5	0	25	−5	10	25	30	35	25	40	25	45	25	50	25
Rotational	·	+	×	■	□	●	○	◆	◇	◂											
Temp. °C	30	25	20	15	10	30	35	40	45	30											

Figure 2.3. Experimental Viscosity values. (A) Complex Viscosity vs angular frequency for oscillatory measurements of honey at −5° to 50°C. (B) Dynamic Viscosity vs strain rate for rotational measurements of honey from 10°C to 45°C.

method at −40.0˚C (Fig. 2.2; Table 2.1 Experimental isobaric heat capacity values of honey used in *Sconf* modeling.). Above about −27˚C, C_{Pl} of the liquid honey increased linearly with increasing temperature:

$$C_{P,l} = 127.75 + 0.6254T \qquad 2.10$$

The RMSD of the fit is 7.3 J mol−1K−1, or about 2% relative, between −27 and +35˚C. Above about 35˚C, the heat capacity curve deviated upwards from the linear trend. We interpret this deviation as the onset of dehydration (Fig. 2.2), which was confirmed after the measurement by a change in sample mass of ~30%.

2.4.2 Viscosity

The range in complex viscosities measured using oscillatory shear was from 1400 Pa s (at −5 °C and $\omega = 0.5$ rad s^{-1}) to 3.026 Pa s (at 35 °C and $\omega = 100$ rad s^{-1}). The viscosity of the honey was largely Newtonian, with a linear relationship between stress and strain rate (Fig. 2.3A). Some deviations from Newtonian behavior are observed during viscosity measurements at or above 35°C at low angular frequencies (< 1 rad s^{-1}; Fig. 2.3A). We attribute the non-Newtonian behavior to the onset of dehydration also observed in the quantitative C_P measurements at about this temperature (Fig. 2.3A) At temperatures below −5˚C, deviations from Newtonian behavior were also observed that are attributed to crystallization.

Dynamic viscosities (Fig. 2.3B) ranged from 67.01 Pa s at 10°C to 2.577 Pa s at 35°C for a shear rate of 100 s^{-1}. Results are mostly Newtonian, except again at higher temperatures (45 °C; Fig. 2.3B), likely the result of sample dehydration. The measured dynamic viscosities agreed well with complex viscosity values over the temperature range where both methods were operable (Fig. 2.3B).

2.4.3 S^{conf} modeling

We chose to model complex viscosity values measured with angular frequencies of 1 rad s^{-1}, 10 rad s^{-1}, and 100 rad s^{-1}, from measurement segments 1, 4-8, 10, and 13-14 because (i) measurements for these segments and temperatures appear Newtonian at these angular frequencies; (ii) the corresponding strain rates cover most consumer and industrial processing for honey (Steffe, 1992) including human mastication (~1 s^{-1}), stirring (~10-1000 s^{-1}), and extrusion (~1-1000 s^{-1}); and (iii) oscillatory measurements cover a wider temperature range than rotational measurements.

The viscosity data in Table 2.2. Experimental Complex viscosity values of honey used for modeling the effect of temperature on the non-Arrhenian viscosity of honey. were fitted to equations (2.1), (2.2), (2.4)-(2.6), and (2.7) and results are shown in Fig. 2.4 and Table 2.3. The Arrhenius equation cannot reproduce the observed non-Arrhenian behavior, and so produced the worst fits to the experimental viscosity data (+14% / −17%). The MYEGA equation using a fixed T_g (233 K, determined by calorimetry) reproduced experimental data marginally better (+12% / −14%) than the Arrhenius equation and was able to reproduce non-Arrhenian behavior. The VFT, AG, and MYEGA (allowing T_g to be adjusted as a fit parameter) equations reproduced experimental data the best with similar precision (± 5%) and were able to reproduce the observed non-Arrhenian behavior.

Table 2.2. Experimental Complex viscosity values of honey used for modeling the effect of temperature on the non-Arrhenian viscosity of honey.

Segment	Temperature		Complex Viscosity (η*; Pa s)		
#	°C	1/K	1 rad s^{-1}	10 rad s^{-1}	100 rad s^{-1}
14	35.0	0.00325	3.671	3.096	3.026
13	30.0	0.00330	5.100	5.066	5.162
1	25.0	0.00335	8.995	9.336	9.652
4	20.0	0.00341	16.87	16.23	15.70
5	15.0	0.00347	34.91	33.55	32.09
6	10.0	0.00353	81.62	76.95	71.09
7	5.0	0.00360	194.8	182.8	166.1
8	0.0	0.00366	513.3	486.0	425.9
10	–5.0	0.00373	1400	1220	1036

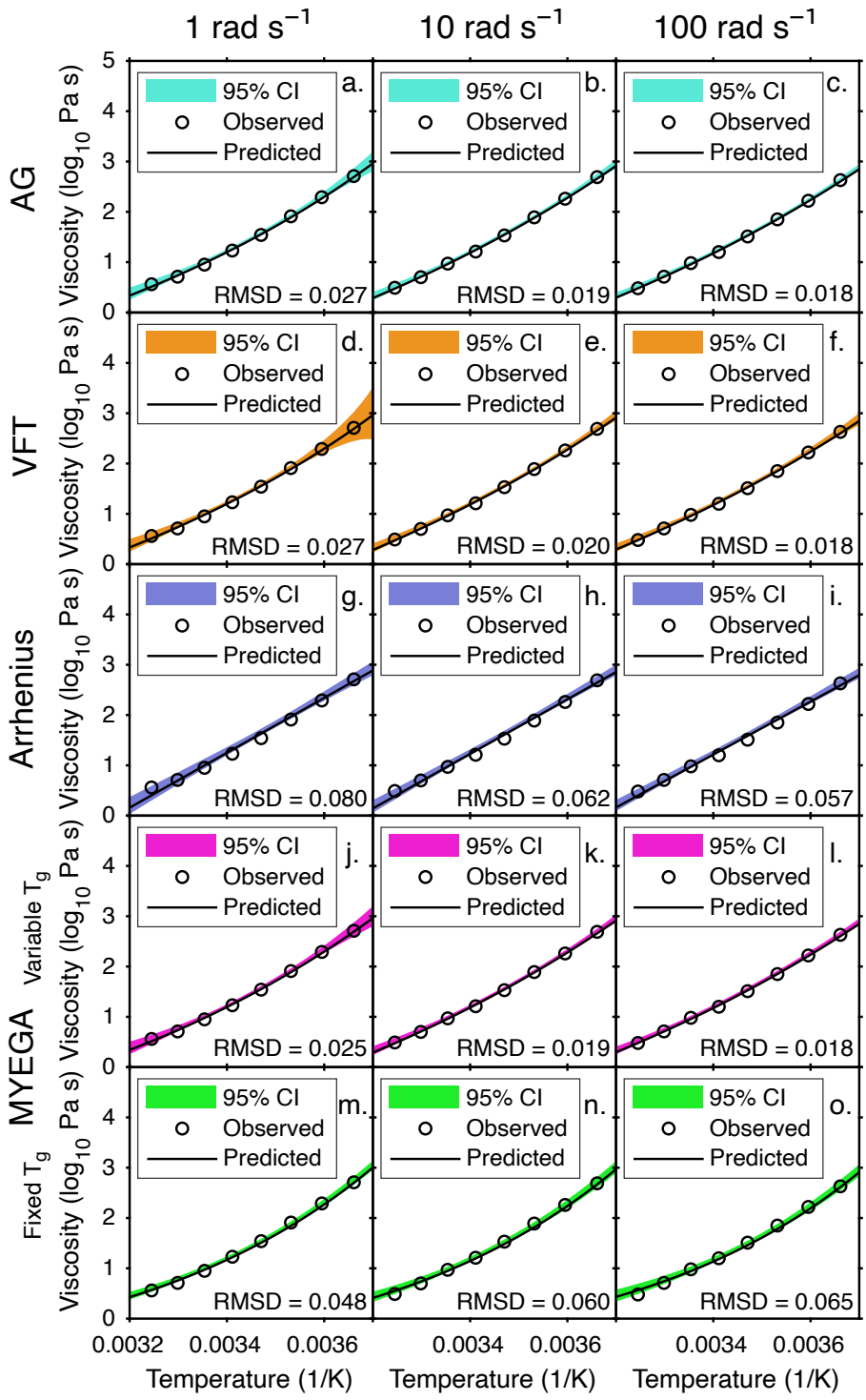

Figure 2.4 log complex viscosity vs inverse temperature with viscosity models using the AG (a, b, c), VFT (d, e, f), Arrhenius (g, h, i) and MYEGA equations with variable T_g (j, k, l) and constant T_g (m, n, o) for experimental viscosity values determined at angular frequencies of 1 rad s^{-1} (a, d, g, j, m), 10 rad s^{-1} (b, e, h, k, n), and 100 rad s^{-1} (c, f, i, l, o).

Table 2.3 Model parameters and goodness of fits for viscosity models and to experimental viscosity data with angular frequencies (ω) of 1 rad s^{-1}, 10 rad s^{-1}, and 100 rad s^{-1}.

Model Name		Model Parameters						Units
Theoretical Models		Symbol	ω 1 rad s^{-1}	± 2σ	ω 10 rad s^{-1}	± 2σ	ω 100 rad s^{-1}	± 2σ	
Arrhenius (Arr)		A_{Arr}	−17.3	1.9	−17.2	1.4	−16.7	1.3	$\log_{10}$ Pa s
		E_a	104	10	104	8	101	7	kJ mol^{-1}
		RMSD		**0.080**		**0.062**		**0.057**	
Adam-Gibbs (AG)		A_{AG}	−3.15	1.73	−3.81	1.71	−3.83	1.34	$\log_{10}$ Pa s
		B_{AG}	84	79	114	123	119	94	kJ mol^{-1}
		$S^{conf}(T_g)$	27.8	29.0	39.6	36.2	42.7	29.8	J mol^{-1}
		RMSD		**0.027**		**0.019**		**0.018**	$\log_{10}$ Pa s
MYEGA	Variable T_g	A_{MY}	−2.39	2.19	−3.32	2.95	−3.45	4.57	$\log_{10}$ Pa s
		m	82.2	31.0	71.4	18.5	68.7	18.4	
		T_g	224	11	219	9	217	14	K
		RMSD		**0.025**		**0.018**		**0.017**	$\log_{10}$ Pa s
	Fixed T_g	A_{MY}	−1.06	0.30	−1.04	0.40	−0.90	0.41	$\log_{10}$ Pa s
		m	110	4	110	6	113	6	
		RMSD		**0.048**		**0.060**		**0.065**	$\log_{10}$ Pa s
Empirical Models									
Vogel-Fulcher-Tammann (VFT)		A_{VFT}	−4.28	2.57	−5.22	2.91	−5.28	2.49	$\log_{10}$ Pa s
		B_{VFT}	536	502	720	921	748	703	
		C_{VFT}	196	37	182	41	178	38	K
		RMSD		**0.027**		**0.020**		**0.018**	$\log_{10}$ Pa

Discussion

2.4.4 Configurational Entropy vs Empirical viscosity models

The experimental viscosity data clearly show non-Arrhenian behavior, and modeling results are similar for the empirical VFT equation, and configurational entropy-based AG and MYEGA equations (Fig. 2.4). The $S^{conf}(T_g)$ for the AG equation can be measured using calorimetry, but only if the material is a congruently melting compound and C_P is known from ~0 K to the liquidus for crystal and glass/liquid (Richet et al., 1984). In this case, the AG equation only has two adjustable model parameters compared to three for the VFT equation. However, for incongruently melting compounds, $S^{conf}(T_g)$ becomes a third adjustable parameter like the C_{VFT} parameter.

Application of the AG equation to experimental viscosity data requires quantitative C_P measurements. Many rheological studies (Sopade et al., 2002; Lazaridou et al. 2004; Recondo et al., 2006; Oroian et al., 2013) of honey already use semi-quantitative heat flow measurements to determine T_g using DSC, but not quantitative C_P measurements required for S^{conf} modeling using the AG equation. The MYEGA equation can be used in place of the AG equation in cases where quantitative C_P is not available, since only the T_g temperature is needed.

We applied the MYEGA equation to our honey dataset in Fig. 2.4. If T_g is known, the MYEGA equation is reduced to two unknown parameters: A_{MY}, and m (Fig 2.4. m, n, o). If T_g is unknown, the MYEGA equation has three adjustable model parameters (A_{my}, m, and T_g) like the VFT and AG equations (Fig. 2.4 j, k, l). The MYEGA equation also requires the viscosity at T_g (η_{Tg}). Fig. 2.4 assumes $\eta_{Tg} = 10^{12}$ Pa s, which is often

described as the viscometric T_g for many liquids (Yue, 2009). The results from varying A_{MY} and m show RMSDs that are less than the Arrhenius equation, but greater than AG and VFT equations. If T_g is also allowed to vary, RMSDs are very similar to the AG and VFT equations, without requiring the quantitative C_P measurements that are needed to apply the AG model.

Discrepancies between predicted T_g (224 K to 217 K) values from the MYEGA equation and the reported half-height temperature (233 K) from our DSC measurements are likely because of the scanning rate used in the DSC measurements of 20°C min^{-1} and reporting the half-height T_g value instead of the onset temperature. The observed T_g temperatures in DSC measurements increase as scanning rates increase, and Yue (2009)

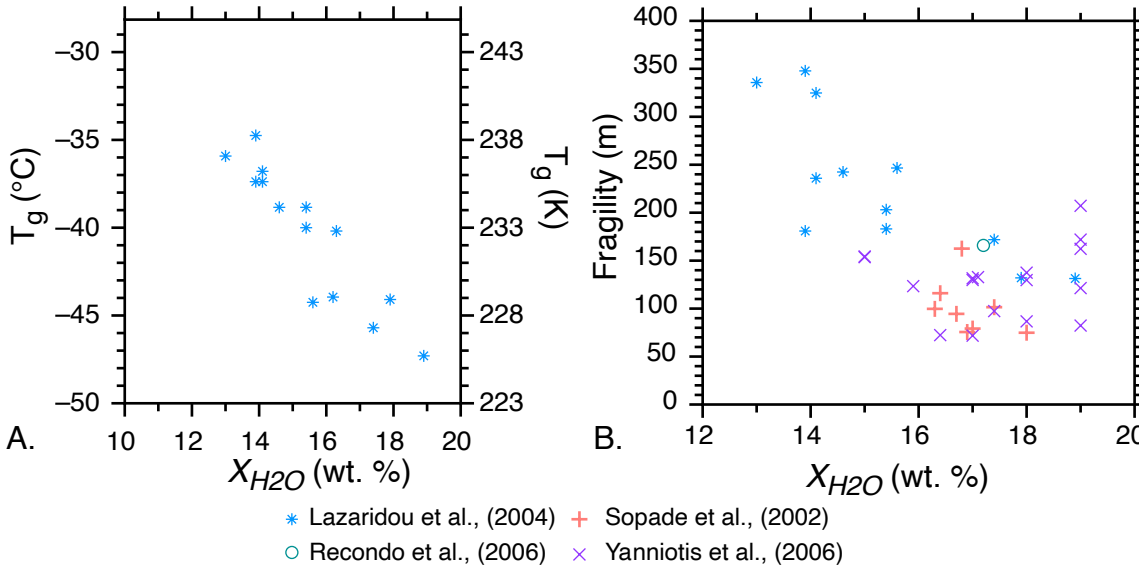

Figure 2.5 Compositional dependence of the glass transition. (A) T_g as a function of X_{H2O} from Lazaridou et al., (2004) shows a negative correlation. (B) Liquid fragility (m) as a function of X_{H2O} also showing a negative correlation and possibly non-linear behavior at high X_{H2O} (>18 wt. %; Sopade et al., 2002; Lazaridou et al., 2004; Recondo et al., 2006; Yanniotis et al., 2006).

shows the viscometric T_g is equal to the onset T_g temperature with a scanning rate of 10°C min^{-1}.

The relative uncertainties of Fig. 2.4 demonstrates that the VFT equation has larger uncertainties at the edges of the calibration dataset. Therefore, the AG and MYEGA equations are better suited to estimating viscosity values beyond its calibration dataset than the VFT equation.

2.4.5 Viscosity as a function of Temperature (T) and Composition (X)

The A_{AG}, B_{AG}, and $S^{conf}(T_g)$ terms of the AG equation have exhibited compositional dependence when modeling the viscosity of inorganic liquids (e.g., Neuville & Richet, 1991; Toplis et al., 1997; Toplis, 1998; Robert et al., 2019), suggesting a thermodynamically-based model for the viscosity of honey as a function of temperature (T) and composition (X) is achievable. After temperature, moisture content (X_{H2O}) is the most important control on the viscosity of honey. Previous studies have shown that the E_a and T_g (Fig. 2.5A) change linearly, and A_{Arr} changes exponentially with moisture content (Lazaridou et al., 2004; Yanniotis et al., 2006). To date, these variations have been expressed through empirical models for the effects of X_{H2O} on the viscosity of honey (Lazaridou et al., 2004; Yanniotis et al., 2006). We have demonstrated that the AG equation successfully describes the effects of temperature on the viscosity of honey. Parameterizing A_{AG}, B_{AG}, and $S^{conf}(T_g)$ as a function of moisture content could yield a model capable of predicting the viscosity of honey as a function of T and X. A similar approach has been shown to work for the effect of water on granitic magma viscosity

(Whittington et al., 2009), and honey has the advantage that it can incorporate large amounts of water at ambient pressure, making experimental measurements easier.

The A_{MY} term in the MYEGA equation is comparable to the A terms in the Arrhenius, AG, and VFT equations, and therefore may be expected to exhibit variation as a function of moisture content (Lazaridou et al., 2004; Yanniotis et al., 2006). The fragility (m) of the liquid is also dependent on X_{H2O}. A compilation of results from Sopade et al., (2002), Lazaridou et al., (2004), Recondo et al., (2006), and Yanniotis et al., (2006), shows a negative correlation between X_{H2O} and m (Fig. 2.5B). Similar trends are observable for glucose and fructose content, but X_{H2O} is the strongest correlation. Again, this suggests that A_{MY}, T_g, and m could be parameterized as a function X_{H2O}, yielding a thermodynamically based model for the viscosity of honey as a function of T-X.

2.5 Conclusions

The AG and MYEGA equations reproduce the non-Arrhenian temperature-dependence of honey viscosity to a similar degree of uncertainty as the empirically based VFT equation and are based in thermodynamics. Theoretical equations, like AG and MYEGA, provide greater confidence for extrapolation to lower temperatures, and could be parameterized for the purpose of a general viscosity model for honey as a function of T-X. The AG equation requires quantitative C_P measurements, and therefore future studies of honey that utilize DSC should measure quantitative C_P whenever possible.

Chapter 3

3. Faster geospeedometry: A Monte Carlo approach to relaxational geospeedometry for determining the cooling rate of volcanic glasses.[1]

3.1 Abstract

The thermal history of natural glasses is critical to understanding a wide range of geologic processes. Relaxation geospeedometry has been used to infer the cooling rate of naturally formed glasses across a wide range of compositions and geologic settings. However, using the Tool-Narayanaswamy (TN) geospeedometer is time consuming, requiring multiple isobaric heat capacity (C_P) measurements to constrain four sample-specific model parameters, before quantifying natural cooling history of a sample. Here we present a Monte Carlo-inspired numerical solver called *CoolMonte*, which automates the fitting procedure of experimental C_P measurements, and can determine an unknown cooling rate using a single C_P measurement. We compare quantitative cooling rates of

[1] Kenderes, S.M. and Whittington, A.G., 2021, Faster geospeedometry: A Monte Carlo approach to relaxational geospeedometry for determining cooling rates of volcanic glasses: Chemical Geology, v. 581, n. 120385, p. 1-12. Reprinted here with permission from Elsevier.

four naturally cooled obsidian lava samples determined using the traditional approach with multiple C_P measurements, to cooling rates determined using a single C_P measurement without sample-specific model calibration. Cooling rates calculated using a single C_P measurement are within 0.1 to 1.3 log10 K s^{-1} of cooling rates determined using multiple C_P measurements. We also assessed *CoolMonte* using 50 synthetic datasets with known cooling rates ($\gtrsim$0.1 K per year) and 10 previously published natural cooling rates which were reproduced within 0.8 log10 K s^{-1}. *CoolMonte* reduces the time necessary to determine cooling rates of natural samples, improves the reproducibility of cooling rate estimates, and makes relaxational geospeedometry a more accessible method for the study of thermal histories of geologic systems.

3.2 Introduction

Relaxation geospeedometry has been revolutionary for quantifying the cooling dynamics of a wide range of geologic processes and products, including lava flows (Wilding et al., 1996a; Gottsmann and Dingwell, 2001a; Gottsmann and Dingwell, 2001b; Gottsmann and Dingwell, 2002; Gottsmann et al., 2004), volcanic bombs (Wilding et al., 1996a), ignimbrite emplacement (Wilding et al., 1996a; Lavallée et al., 2015), submarine volcanism (Wilding et al., 2000; Potuzak et al., 2008; Nichols et al., 2009), subglacial volcanic deposits (Wilding et al., 2004), tektite formation (Wilding et al., 1996b), impact glasses (Rantzsch et al., 2013) and lunar glass droplets (Hui et al., 2018).

The most common method used to determine the cooling rates of natural glasses is the Tool-Narayanaswamy (TN) geospeedometer (Tool, 1946; Narayanaswamy, 1971;

Wilding et al. 1995). The TN-geospeedometer is ideal for samples that have experienced cooling rates that are less than or equal to experimental heating and cooling rates (~10^1 K min^{-1}). Glasses that experience faster than experimental cooling rates are more suited by the Moynihan-Yue (MY) geospeedometer (Moynihan et al., 1976; Yue et al., 2002; Hue et al., 2018).

Both geospeedometers require repeat quantitative isobaric heat capacity (C_P) measurements to model the enthalpy of relaxation of a sample using the concept of the fictive temperature (T_f) to determine quantitative natural cooling rates. The T_f represents the contribution of structural relaxation to a structurally dependent property (e.g., H or V) through the glass transition (T_g) and is presented in the units of temperature (Moynihan, 1995).

The MY-geospeedometer uses an area-matching method of C_P measurements to estimate the T_f of a naturally cooled sample. The first C_P measurement, which contains natural cooling rate information in the form of a trough observed before T_g, is compared to a second C_P measurement with an experimentally controlled thermal history. Next T_f of additional repeat C_P measurements with matched heating and cooling rates ($q_c = q_h$) are used to extrapolate a cooling rate for the naturally cooled sample (Potuzak et al., 2008; Nichols et al. 2009).

The TN-geospeedometer instead models relaxation behavior on heating directly but requires four-sample specific model parameters to be determined before extracting natural cooling rate information. Again, the first C_P measurement contains natural cooling information that manifests as a tall peak at T_g, where peak height typically increases as cooling rate decreases. Multiple measurements with known matched heating

and cooling rates ($q_c = q_h$) are then used to constrain four-sample specific model parameters before solving for the unknown cooling rate of the first C_P measurement. For this study, we focus on an improved implementation of the TN-geospeedometer because it is preferred for modeling slow ($<10^{-4}$ K s^{-1}) to moderately fast ($\sim10^{1}$ K s^{-1}) cooling of natural rhyolite obsidians.

Implementing the TN-geospeedometer however, includes significant technical challenges. Requiring four to six C_P measurements of the same sample aliquot to a temperature ~50°C above the T_g ensuring the glass can relax fully increases the likelihood of significant compositional changes to the sample, such as dehydration or crystallization, that can compromise attempts at constraining the sample-specific relaxation parameters. Also predicting T_g *a priori* is challenging because T_g is a function of composition (Giordano et al., 2008), volatile content (Stevenson et al., 1998; Romine and Whittington 2015), thermal history, and experimental heating rate (Moynihan, 1995).

Performing multiple C_P measurements on a single sample also requires considerable time. Each quantitative C_P measurement requires ~1 day to complete, consisting of repeat runs with an empty pan, sapphire standard, and then the sample. If constraining sample-specific model parameters requires three to five C_P measurements, in addition to the original measurement through T_g containing natural cooling information, then to gather the data necessary to calculate a single natural cooling rate can require between four and six days.

Determination of natural cooling rates from a single C_P measurement would therefore yield several benefits, including saved time, and the ability to more confidently measure volatile-rich or crystallization-prone glasses. However, constraining cooling

rates from a single C_P measurement requires understanding the influence of the model parameters on predicted cooling rates and is computationally intensive.

Monte Carlo simulations are a computationally efficient way to solve multi-dimensional problems. Here we present *CoolMonte*, a Monte Carlo inspired numerical solver for the TN-geospeedometer written in MATLAB. Our algorithm works in three steps: (1) Randomized input relaxation parameters between reasonable fixed upper and lower bounds are used to simulate a user-defined number of model outputs that can be compared to experimental C_P data using a goodness-of-fit measure such as the root mean square deviation (RMSD). (2) Model simulations with an RMSD less than two-times the lowest RMSD are stored, producing distributions of each previously unconstrained model parameter. (3) The mean and standard deviation of these distributions can then be assessed, including cooling rates of natural volcanic glasses.

To assess the performance of *CoolMonte* we first solved for quantitative cooling rates of four natural obsidian samples by constraining sample specific relaxation parameters using multiple C_P measurements. Then we solved for natural cooling rates using only the first C_P measurement through T_g without sample-specific calibrations with *CoolMonte*. We further tested *CoolMonte* using 50 synthetic datasets generated using known input relaxation parameters and 10 previously published natural cooling rates.

Table 3.1. Natural Sample Selection

Sample Name	Depth (m)	Location	Texture
RDO-2A-2.5	0.8	Obsidian Dome	FVP
RDO-2A-36.5	11.1	Obsidian Dome	CVP
RDO-2A-87	26.5	Obsidian Dome	DO
VC-1-369.5	112.7	Banco Bonito	DO

3.3 Methods

3.3.1 Natural Sample Selection

We selected four samples of naturally cooled obsidian, collected from two drill cores from young obsidian lava domes and coulées in the western United States as part of the Continental Scientific Drilling Program (CSDP). Obsidian Dome is the largest (0.17 km^3) and youngest (~600 a) of the rhyolite to rhyo-dacite (~71 wt. % SiO_2) lava domes associated with the Inyo Craters, CA (Miller, 1985). In the field season of 1984, scientific drilling produced two cores. The first was near the southern flow margin (RDO-2A) and the second intersected the conduit feeding the lava dome (RDO-2B; Eichelberger et al., 1985). The VC-1 drill core samples the entire thickness (~150 m) of Banco Bonito, a large (~4 km^3; Wolff et al., 2011) high-silica rhyolite (~75% SiO_2) coulée and the youngest eruptive unit of the El Cajete series from the Valles caldera, NM at 68.3 ± 1.5 ka (Zimmerer et al., 2016).

Three samples were selected from drill core RDO-2A (-2.5, -36.5, -87) and one from the VC-1 (-369.5) drill core (Table 3.1). The sample ID suffix corresponds to drill depth from the surface in feet. Samples represent the three glassy textures often observed at obsidian lavas, including fine vesicular pumice (FVP; RDO-2A-2.5), coarse vesicular pumice (CVP; RDO-2A-36.5) and dense obsidian (DO; RDO-2A-87 & VC-1-369.5; Manley and Fink, 1987).

The samples chosen from different depths and proximity to crystallizing core should yield a range in cooling rates. RDO-2A-2.5 likely cooled the fastest (~10^{-1} to 10^{1}

K s^{-1}) being at the surface of the lava flow and sample VC-1-369.5 likely cooled the slowest (<10^{-5} K s^{-1}) being near the crystalline core in the center of Banco Bonito.

Aliquots of all four samples were drilled using a diamond core drill bit with an interior diameter of ~6 mm, from which discs ~2 mm thick were cut with an average mass of ~70 mg and polished for improved thermal contact during measurement.

3.3.2 Differential Scanning Calorimetry

A Netzsch Pegasus 404F1 differential scanning calorimeter (DSC) was used to measure C_P as a function of temperature for the four samples from Obsidian Dome and Banco Bonito. Scanning rate-specific temperature and sensitivity calibrations were made using the melting point and enthalpy of fusion of metals In, Sn, Zn, Al, and Au for scanning rates of 10 K min^{-1}, 20 K min^{-1}, 30 K min^{-1}, 40 K min^{-1}, and 50 K min^{-1}. The faster the heating rate, the higher the signal-to-noise ratio. A pure ~84 mg sapphire standard (Al_2O_3) was used to calibrate the heat flow of each sample measurement to quantitative C_P (in units J g^{-1} K^{-1}; Ditmars et al., 1982).

The sample was heated at a constant 30°C min^{-1} to ~50°C above T_g, and then cooled at −30°C min^{-1} to room temperature for the first DSC measurement. The same glass disc was then heated at the same rate as the cooling segment of the previous measurement, so that multiple thermal treatments with experimentally controlled thermal histories were completed. Thermal treatments were completed using rates in non-sequential order to monitor for irreversible sample changes during the measurements, like how experimental viscosity measurements are made using a uniaxial parallel-plate viscometer (Whittington et al., 2009).

Each experimental C_P measurement can be divided into three temperature segments: the glass heat capacity (C_{Pg}) where $T < T_g$, the C_P through the glass transition interval, and the liquid heat capacity (C_{Pl}) where $T > T_g$. The C_{Pg} increases non-linearly with increasing temperature and is modeled effectively by the three-parameter equation (Maier and Kelley, 1932):

$$C_{P_g}(T) = a + \frac{b}{T} + \frac{c}{T^2} \qquad 3.1$$

where T is temperature in Kelvin, a b and c are empirical parameters, and C_{Pg} is in J g^{-1} K^{-1}. The C_{Pl} is not temperature-dependent for most lava compositions and is effectively described by a constant.

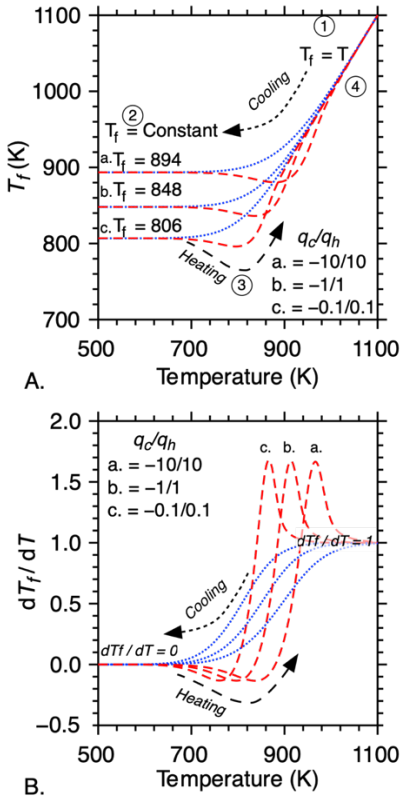

Figure 3.1 Evolution of the fictive temperature (T_f; A) of a glass as a function of temperature (T) and thermal history calculated using eq. 3.6 where $\tau_0 = 10^{-14}$ s, $\Delta H =$

300 kJ mol^{-1}, $\beta = 0.7$, $\xi = 0.7$, $q_c = [-0.1, -1.0, -10.0$ K min$^{-1}]$, and $q_h = [0.1, 1.0, 10.0$ K min$^{-1}]$. Long-dashed lines represent cooling paths and short-dashed lines represent heating paths. (B) The corresponding evolution of the derivative of T_f as a function of T (dT_f/dT), which is directly comparable to normalized C_P using eq. 3.3.

3.3.3 The glass transition

The glass transition (T_g) describes the temperature region where, on cooling, a material changes from a super-cooled liquid to an amorphous solid. This microscopic change is observable in macroscopic physical properties of the material, like volume (V) and enthalpy (H). Since T_g is a second-order thermodynamic transition, a discontinuous or very rapid jump is observable in the derivatives of these properties with respect to temperature, such as thermal expansivity (dV/dT; α) and isobaric heat capacity (dH/dT; C_P). We can use the C_P curve as a geospeedometer because the relaxation of the sample is controlled by kinetics, which imprints information about the thermal history of the glass in its structure as it cools through T_g.

We can define the relaxation of a glass using the Maxwell relation (Maxwell, 1867), where the characteristic relaxation time (τ, in s) is related to the melt viscosity (η, in Pa s) and shear modulus (G_∞, in Pa) through the equation:

$$\tau = \eta/G_\infty \qquad 3.2$$

where η, and therefore τ, are temperature dependent. For silicate melts, G_∞ is of the order of 10 GPa (Dingwell and Webb, 1990; Webb, 1992). However, there appears to be some compositional dependence, and the best average value of G_∞ for a wide range of dry and hydrous melt compositions is about 30 ± 5 GPa (Whittington et al., 2012). These properties control how quickly a glass can relax to the equilibrium structure for a given

temperature. However, as the glass cools, the relaxation time increases, until the cooling rate exceeds the rate of relaxation, quenching in a structure that can no longer equilibrate at lower temperatures.

Unlike crystalline materials, which form ordered repeating structures as they solidify, the structure of a glass is controlled by the rate at which it is quenched to a solid. The structural contribution to relaxation of a structurally dependent property (e.g., H or V; Moynihan, 1995) of the glass can be described using the concept of the fictive temperature (T_f; Tool, 1946), which is presented in units of temperature. The T_f models the structure of the glass between an equilibrium and disequilibrium state. The phenomenological evolution of T_f and its derivative as a function of temperature (dT_f/dT) are shown in Figure 3.1 Evolution of the fictive temperature (Tf; A) of a glass as a function of temperature (T) and thermal history calculated using eq. 3.6 where $\tau 0 = 10^{-14}$ s, $\Delta H = 300$ kJ mol^{-1}, $\beta = 0.7$, $\xi = 0.7$, $qc = [-0.1, -1.0, -10.0$ K min$^{-1}]$, and $qh = [0.1, 1.0, 10.0$ K min$^{-1}]$. Long-dashed lines represent cooling paths and short-dashed lines represent heating paths. (B) The corresponding evolution of the derivative of Tf as a function of T (dTf/dT), which is directly comparable to normalized CP using eq. 3.3. At temperatures greater than T_g, $T_f = T$ ($dT_f/dT = 1$; Fig. 3.1B) because relaxation times are fast, and the structure is in equilibrium (Fig. 3.1A-1). As the liquid cools, relaxation times increase, and the structure of the liquid begins to deviate from equilibrium ($T_f \neq T$), until relaxation times are so long that the structure of the glass can no longer change and $T_f =$ constant ($dT_f/dT = 0$; Fig. 3.1A-2), and the sample has become glass. The value of T_f of the glass is a function of cooling rate (Fig. 3.1A-a, b, c). On reheating, relaxation times decrease, allowing the glass structure to re-equilibrate slowly at first, and then quickly

(Fig. 3.1A-3), until the glass is above T_g, and relaxation times are fast so that T_f again is in equilibrium with T (Fig. 3.1A-4).

The derivative of T_f as a function of temperature (dT_f/dT; Fig. 3.1B) is directly related to structurally dependent properties such as H, through its derivative C_P (dH/dT), by the equation (DeBolt et al., 1976):

$$\frac{dT_f}{dT} = \frac{\left(C_P - C_{P_g}\right)|_T}{\left(C_{P_l} - C_{P_g}\right)|_{T_f}} \tag{3.3}$$

which connects a readily measurable structurally dependent property like H to the concept of T_f, and therefore the determination of cooling rates of glasses.

3.3.4 Modeling the fictive temperature

Modeling the fictive temperature first requires defining the form of the relaxation equation, and relaxation time as a function of structure and temperature. A commonly used relaxation equation is the Kohlrausch-William-Watts function (KWW; Kohlrausch, 1854; Williams and Watts; 1969; DeBolt, 1976; Scherer, 1984) which has been shown to fit a wide range of relaxation processes and is sometimes referred to as the stretched exponential function:

$$p = p_0 \, exp\left[-(t/\tau_k)^{\beta}\right] \tag{3.4}$$

where p is some property (e.g., H or V), t is time, τ is the characteristic relaxation time, and β is an order parameter that describes the structural contributions to relaxation and is

constrained to be 0<β<1. The TN-geospeedometer uses an Arrhenian form of the relaxation time, to account for the effects of temperature on τ, which is expressed as (Narayanaswamy 1971; Narayanaswamy, 1988):

$$\tau_k = \tau_0 \, exp\left[\frac{\xi \Delta H}{RT} + \frac{(1-\xi)\Delta H}{RT_{f_{k-1}}}\right] \quad 3.5$$

where R is the gas constant (8.314 J K^{-1} mol^{-1}) and ξ is an empirical constant (0<ξ<1), ΔH is the enthalpy of relaxation (J mol^{-1}) and τ_0 is the limiting relaxation time (s).

The equation from DeBolt et al., (1976) combines equations 3.4 and 3.5 and is the preferred method for modeling the evolution of T_f as a function of T is using the equation:

$$T_{fm} = T_0 + \sum_{j=1}^{m}\left(T_{f_{j-1}} - T_j\right)\left[1 - e^{-\left(\sum_{k=j}^{m}\frac{\Delta T_k}{|q_k|\tau_k}\right)^{\beta}}\right] \quad 3.6$$

where T_{fm} is the T_f at step (m), and ΔT_k is the temperature step ($\Delta T = 1$ for this study). Equation 3.6 is first used to simulate cooling using a negative q value, quenching a T_f into a glass from an equilibrium temperature above T_g (T_0 = 1500 K). Next, heating is simulated using a positive q value, with T_0 equal to the lowest T_f value determined from the cooling calculation.

Equation 3.3 allows the direct comparison of the output of eq. 3.6 to experimental C_P measurements. The left side of eq. 3.3 is equal to the derivative of the output from eq. 3.6 with respect to temperature (dT_f/dT), and the experimental C_P data are normalized using the right side of eq. 3.3. Normalizing experimental C_P data makes C_{Pg} and C_{Pl} constant where C_{Pg} = 0 and C_{Pl} = 1. The normalized C_P is also dimensionless.

3.3.5 Quantifying natural cooling rates using the TN Geospeedometer

Previous studies have determined quantitative natural cooling rates of volcanic glasses by first constraining four sample-specific model parameters in equations 3.4, 3.5, and 3.6, including τ_0, ΔH, β and ξ, using multiple C_P measurements with experimentally controlled thermal histories ($q_c = q_h$).

The ΔH (J mol^{-1}) and τ_0 (s) are determined using the Arrhenius relationship between the T_g (10000 K^{-1}) and experimental quench rate q_c ($-\log_{10}$ K s^{-1}) of multiple thermal treatments:

$$-log_{10}|q_c| = -log_{10}(\tau_0) + \frac{\Delta H}{2.303RT_g} \quad 3.7$$

where R is the gas constant (8.314 J K^{-1} mol^{-1}) and T_g is defined as the temperature (K) that corresponds to the maximum peak height in the C_P curve. Uncertainties on ΔH and τ_0 are defined as two-times the standard deviation of 1000 bootstrap resampling iterations.

Empirical parameters ξ and β are then constrained using C_P measurements, where $q_c = q_h$ and ΔH and τ_0 are known from equation 3.7. Fitting is usually accomplished by minimizing a goodness-of-fit measure such as χ^2 (Wilding et al., 1995) or the root-mean square deviation (RMSD). Fitting ideally produces consistent values of β and ξ for all thermal treatments of a given sample, but often this is not the case, especially if ΔH and τ_0 are allowed to vary within their 2σ uncertainties.

Once ΔH, τ_0, ξ, and β are constrained using multiple C_P measurements, the last remaining unknown model parameter is cooling rate (q_c) for the original C_P measurement through T_g, which can again be optimized by allowing q_c to vary and minimizing a goodness-of-fit metric such as χ^2 or RMSD.

3.3.6 Challenges of the TN-Geospeedometer

Solving for unknown natural cooling rates using the TN-geospeedometer requires multiple experimental thermal treatments ($q_c = q_h$) to constrain four sample-specific model parameters as previously discussed, which are time-consuming. First, each thermal treatment requires approximately one day to complete, consisting of repeat runs of an empty pan, sapphire standard, and then the sample. Second, the minimum number of thermal treatments to adequately constrain the model parameters is about three measurements, which means a single quantitative cooling rate requires a minimum of four days of measurement.

There are also significant experimental challenges that must be considered. For thermal treatments to be useful for constraining model parameters, samples must not undergo any compositional changes during measurements, such as dehydration or crystallization. Measurements are designed to minimize the likelihood of these changes by only heating samples to ~50 °C above T_g. However, the T_g of the sample is difficult to identify prior to measurement because T_g is itself a function of glass composition (especially water content), thermal history, and experimental heating rate. Viscometry measurements, which reflect variations due only to composition, show that T_g can vary by >50˚C even for nominally degassed rhyolitic lavas (Stevenson et al., 1998; Romine and Whittington, 2015).

Information about the natural cooling rate is preserved in the initial DSC measurement through T_g, and if it were possible to extract that information without

requiring additional C_P measurements, these practical problems with applying the TN-geospeedometer would be resolved.

3.3.7 Optimization algorithms

Two algorithms preceded *CoolMonte* and were called *CoolBrute* and *OptRigor*. *CoolBrute* was designed as a grid-search algorithm that systematically calculates permutations of all five previously constrained relaxation parameters within their estimated uncertainties until a global minimum in RMSD is found. This algorithm can reliably identify the lowest RMSD, however it cannot be used effectively when model parameters are poorly constrained without requiring weeks to months for computation. Select natural cooling rate distributions from *CoolBrute* are indistinguishable ($p < 0.05$) from those determined using *CoolMonte*.

The second algorithm, *OptRigor*, uses a slightly different approach to optimization. *OptRigor* relies on a non-linear numerical solver to identify the lowest RMSD between equation 3.6 and observed data. One concern however, when using a numerical solver is the influence of the initial guess on predicted model parameters. To address that concern, we performed 100 optimizations using a randomized initial guess for each optimization. The most common result should be the global minimum. *OptRigor* performs reasonably well, however *CoolMonte* achieves comparable results faster, and is simpler by design.

CoolMonte was originally developed to optimize model parameters ξ and β using experimental thermal treatments with poorly constrained ΔH and τ_0 parameters, by using a Monte Carlo approach to fitting experimental C_p data with equations 3.3 and 3.6. The

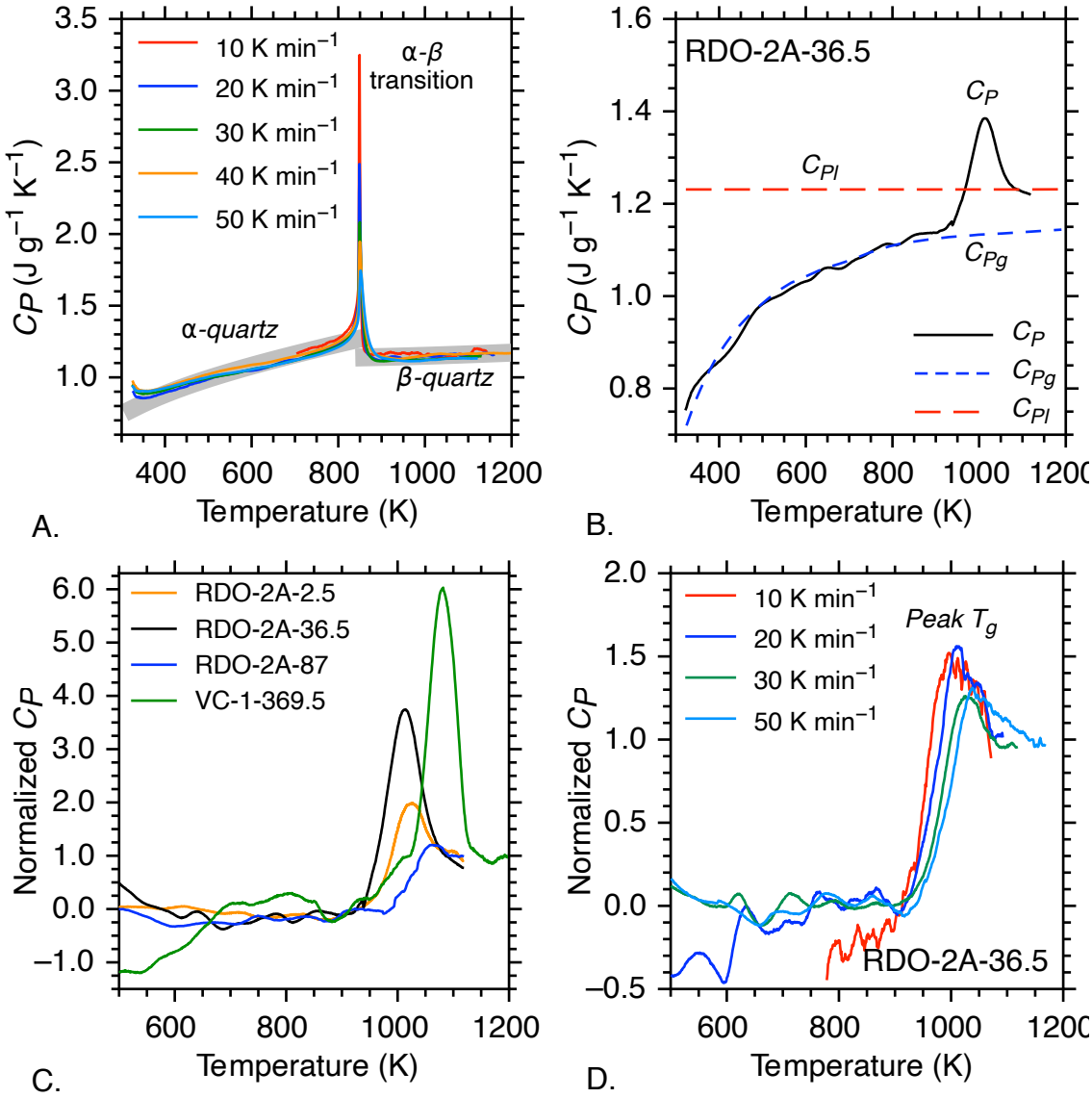

Figure 3.2 DSC performance. (A) Isobaric heat capacity (CP) vs temperature (K) for reference quartz sample measured at five different heating rates, gray fields represent reference CP values for α- and β-quartz ± 3% relative. (B) Isobaric heat capacity (CP) vs temperature (K) for sample RDO-2A-36.5, with glass heat capacity (CPg) and liquid heat capacity (CPl). (C) Normalized CP vs temperature (K) for naturally cooled obsidian samples RDO-2A-2.5, RDO-2A-36.5, RDO-2A-87, and VC-1-369.5. (D) Normalized CP vs temperature (K) for experimental thermal treatments (qc = qh) of sample RDO-2A-36.5.

user can define upper and lower boundary conditions for the five model parameters ΔH, τ_0, β, ξ, and q_c. For single C_P measurement optimization, the boundary conditions were

defined as $200 \leq \Delta H \leq 800$ (kJ mol^{-1}), $10^{-30} \leq \tau_0 \leq 10^{-5}$ (s), $0 < \beta < 1$, $0 < \xi < 1$, and $10^{-14} \leq q_c \leq 10^4$ (K min^{-1}) which more than exceeds the range of probable natural values. Within these bounds, the algorithm generates a randomized set of input parameters with replacement, and then uses equations 3.3—3.6 to generate a model C_P curve. If the predicted peak falls within ±10 K of the observed peak, the set of input parameters is stored with a corresponding estimate of fit or RMSD. The algorithm will continue until a user defined number of outputs are achieved, which for this study was defined as 10,000.

Once the optimizations are complete, the results are reduced to the combinations of model parameters that correspond to an RMSD less than or equal to two-times the lowest RMSD resulting in distributions for each relaxation parameter. The lowest RMSD obtained reflects a combination of the signal-to-noise ratio of the calorimeter, and how much the C_P curve deviates from the ideal relaxation model. The mean of each distribution defines the best fit value and uncertainties are equal to two-times the standard deviation of each parameter. Uncertainty envelopes in figures 4-6 are defined as the maximum (+2σ) and minimum (−2σ) value at each temperature value produced by model outputs within two-times the lowest RMSD.

3.4 Results

3.4.1 DSC measurements

Twenty-one DSC measurements were completed, including four measurements of naturally cooled volcanic glasses, 17 additional measurements of the samples with laboratory-controlled thermal histories to constrain sample-specific model parameters,

and five additional C_P measurements of a reference natural quartz sample are presented to demonstrate the performance of the DSC. Fig. 3.2A shows repeat measurements of the same piece of quartz made under identical conditions as natural glass samples. Quartz is an ideal reference mineral because it has C_P for α- and β-quartz and the α-β transition temperature. Quantitative C_P values for α- and β-quartz are reproduced within 3% of reference values (Robie and Hemingway, 1995) and the α-β transition temperature is reproducible <0.3% relative uncertainty.

Fig. 3.2B shows the first quantitative C_P measurement of sample RDO-2A-36.5 through T_g which includes natural cooling information. The height of the peak suggests relatively slow cooling. Fig. 3.2B also shows the best fit C_{Pg} using eq. 3.1, and the C_{Pl} used in eq. 3.3 (C_{Pg} = 0 and C_{Pl} = 1) to normalize the C_P measurement.

Normalized quantitative C_P measurements for the four naturally cooled obsidian samples are shown in figure 3.2C and measurements for sample RDO-2A-36.5 with experimentally controlled thermal histories are shown in figure 3.2D. Naturally cooled samples exhibit a range in normalized peak heights, defined as the maximum normalized C_P within the T_g region. Sample RDO-2A-87 has the smallest normalized peak height, and sample VC-1-369.5 has the largest peak height (Fig. 3.2C). Measurements of samples with experimentally controlled thermal histories are characterized by a subtle dip and generally smaller peak when passing through T_g (Fig. 3.2D). Signal to noise ratio generally improves as experimental q_h increases. The signal was considerably noisier for sample VC-1-369.5 (Fig. 3.2C) which is likely due to Banco Bonito being considerably older than Obsidian Dome.

Table 3.2 Peak Tg temperatures and experimental quench rates used for determining ΔH and τ_0 from the Arrhenius relationship.

Sample		Quench Rate °C min^{-1}	Peak T_g °C
RDO-2A-2.5		−10	769.8
		−20a	832.4
		−20b	824.3
		−30	808.8
		−50a	848.9
		−50b	833.8
	H	177 ± 650	kJ mol^{-1}
	τ_0	−8.0 ± 30.7	$\log_{10}$ s
RDO-2A-36.5		−10	723.2
		−20	740.7
		−30	759.2
		−50	766.6
	H	300 ± 181	kJ mol^{-1}
	τ_0	−15.0 ± 9.2	$\log_{10}$ s
RDO-2A-87		−10	747.1
		−20	767.0
		−30	781.3
		−50	806.5
	H	251 ± 90	kJ mol^{-1}
	τ_0	−12.1 ± 4.5	$\log_{10}$ s
VC-1-396.5		−20	801.0
		−30	817.9
		−50	835.6
	H	274 ± 175	kJ mol^{-1}
	τ_0	−12.9 ± 8.4	$\log_{10}$ s

3.4.2 Determining unknown cooling rates using multiple C_p measurements

Experimental quench rates ($-\log_{10} q_c$) for thermal treatments are plotted against peak T_g (as 10000 K^{-1}) in Fig. 3.3. These data are used to estimate ΔH and τ_0 using equation 3.7, and the results are listed in Table 3.2. Predicted ΔH and $\log_{10}\ \tau_0$ values vary inversely, with RDO-2A-2.5 having the smallest ΔH value (177 ± 650 kJ mol^{-1}) and largest $\log_{10}\ \tau_0$ value (−8.0 ± 30.7 $\log_{10}$ s), and RDO-2A-36.5 having the largest ΔH value

(300 ± 181 kJ mol^{-1}) and smallest $\log_{10}$ τ_0 value (−15.1 ± 9.2 $\log_{10}$ s). The large uncertainties observed for sample RDO-2A-2.5 are likely the result of dehydration, inferred from an observed mass loss of ~0.6 wt. % for sample RDO-2A-2.5. The mass of samples RDO-2A-36.5, RDO-2A-87, and VC-1-369.5 changed by <0.1 wt. % between measurements.

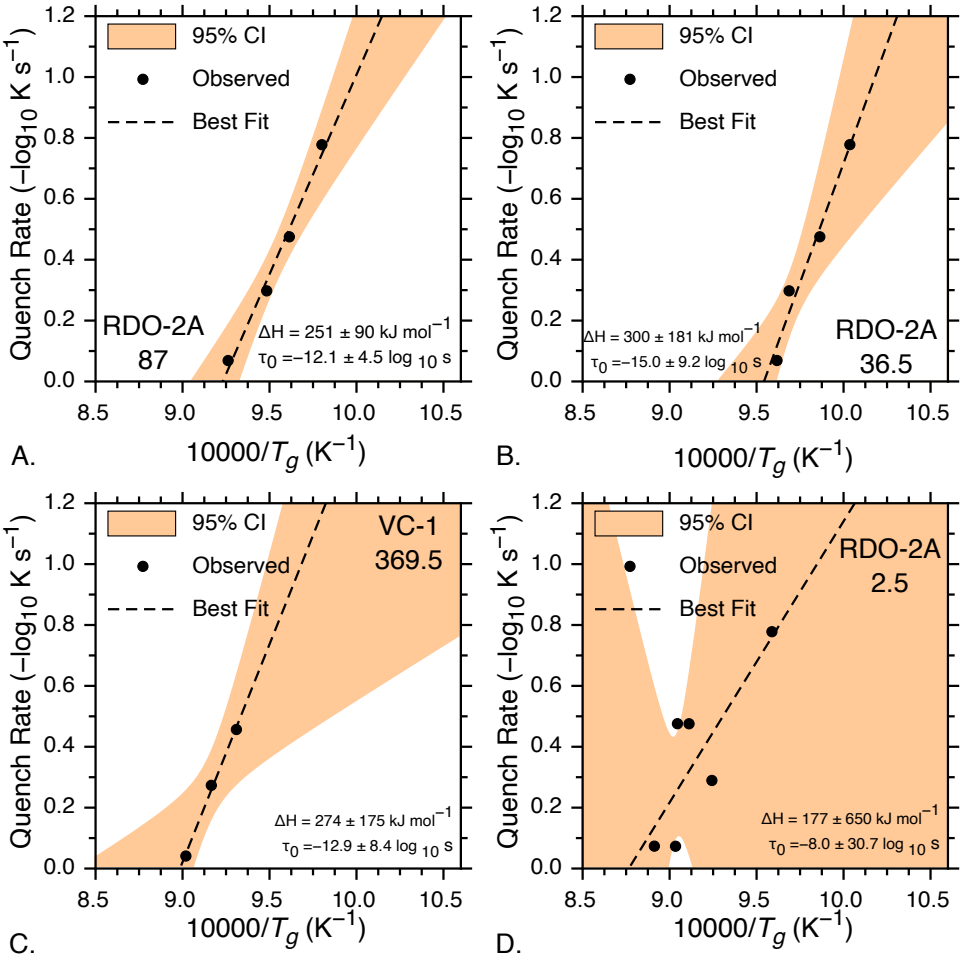

Figure 3.3 Arrhenius diagram for four obsidian samples. Experimental quench rate and inverse T_g for samples (A) RDO-2A-87, (B) RDO-2A-36.5, (C) VC-1-369.5, and (D) RDO-2A-2.5 to constrain enthalpy of relaxation (ΔH; slope) and limiting relaxation time (τ_0; y-intercept) with 95% confidence intervals as orange fields calculated using 1000 bootstrap resampling iterations (Eq. 3.7).

Collectively these four samples represent the most likely outcomes when trying to constrain ΔH and τ_0 experimentally. The best-case scenarios have a very convincing (Fig. 3.3A) and reasonably convincing (Fig. 3.3B) Arrhenius relationship observed for up to four measurements. Fig. 3.3C & 3.3D show less optimal scenarios. In figure 3.3C a convincing Arrhenius relationship exists but shows how the uncertainty envelope changes when fewer measurements are used. The worst-case scenario is shown in figure 3.3D. Here the sample has experienced irreversible change during measurements, calling into question any attempts to estimate natural cooling rates using the TN-geospeedometer.

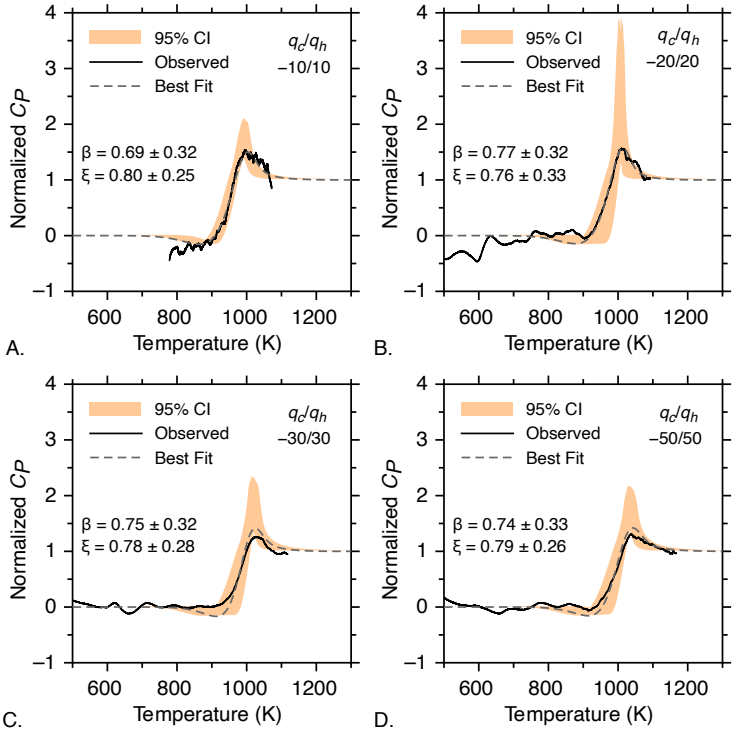

Figure 3.4 β and ξ values determined using CoolMonte for thermal treatments ($q_c = q_h$; K min^{-1}) from sample RDO-2A-36.5. Black solid lines represent measured experimental data, dashed gray lines represent the model output with the lowest RMSD, and 95% confidence intervals are represented by orange fields correspond to the maximum and minimum value for models with RMSD ≤ two-times the lowest RMSD.

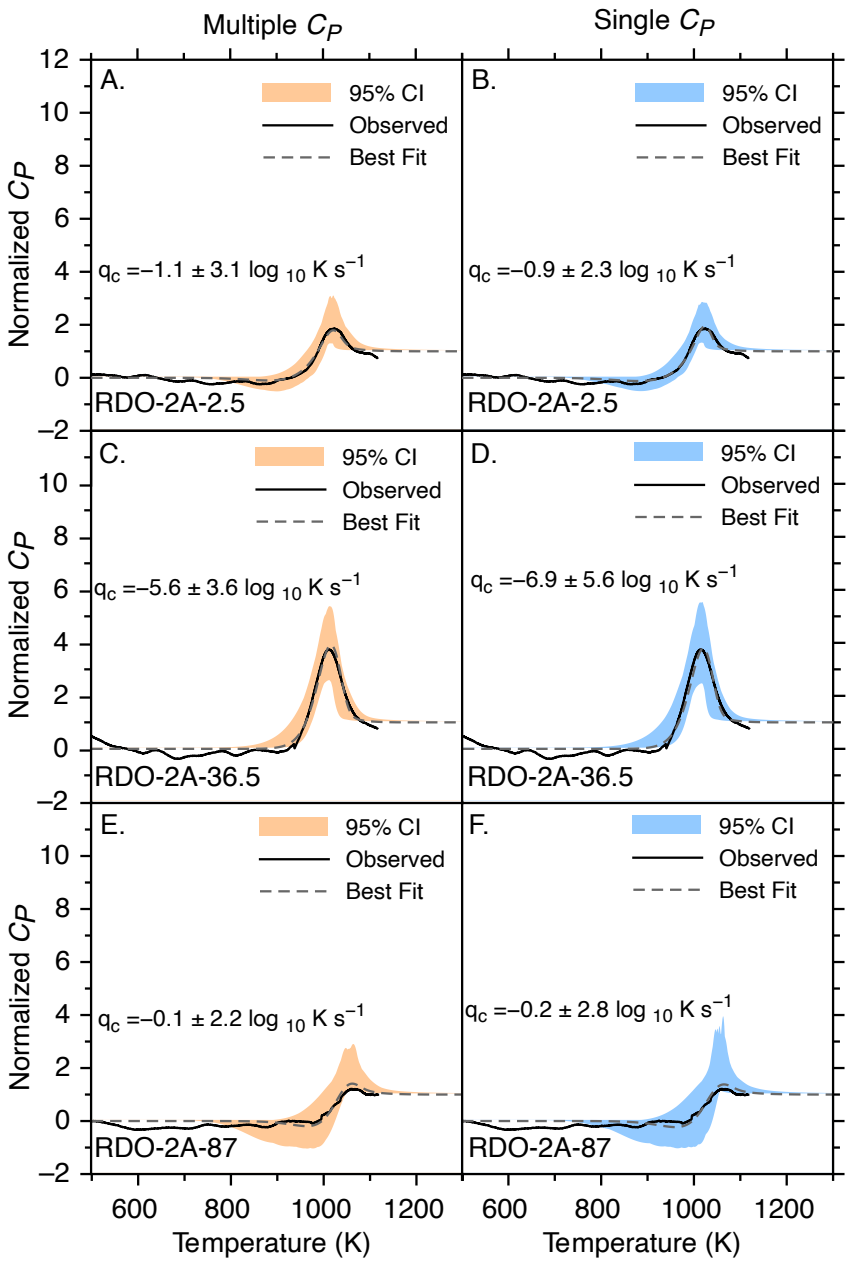

Figure 3.5. Quantitative cooling rates determined using *CoolMonte* with sample-specific parameters constrained using multiple C_P measurements (A, C, E), and optimizations fitting a single C_P curve (B, D, F) for samples from Obsidian Dome RDO-2A-2.5 (A, B), RDO-2A-36.5 (C, D), and RDO-2A-87 (E, F). Solid black lines represent measured normalized C_P data, dashed gray lines represent the model output with the lowest RMSD, and 95% confidence intervals are represented by orange fields (maximum and minimum value for models with RMSD ≤ two-times the lowest RMSD) for cooling rates determined using multiple C_P measurements and blue fields for cooling rates determined using a single C_P measurement.

Table 3.3 Geospeedometric model parameters determined using *CoolMonte* using multiple and single C_P measurements from Obsidian Dome (RDO-2A) and Banco Bonito (VC-1).

Sample	q_c/q_h K min^{-1}	H kJ mol^{-1}	±	τ_0 log$_{10}$ s	±	β	±	ξ	±	q_c log$_{10}$ K s^{-1}	±	n	*RMSD*
RDO-2A-2.5													
Step 1: Calibration	−10/10	549	329	−23.8	15.0	0.54	0.39	0.82	0.22			3172	0.1113
	−20/20a	602	308	−26.3	14.5	0.64	0.41	0.75	0.31			7597	0.2226
	−20/20b	595	307	−26.2	14.5	0.63	0.40	0.73	0.33			7325	0.1354
	−30/30	612	300	−27.8	14.5	0.66	0.42	0.74	0.33			8770	0.1411
	−50/50a	606	309	−26.5	14.4	0.66	0.41	0.74	0.32			8161	0.1140
	−50/50b	634	281	−24.4	14.6	0.57	0.39	0.75	0.29			4982	0.1071
Step 2: Multiple C_P	NAT/30	635	301	−30.0	14.6	0.52	0.39	0.78	0.30	−1.1	3.1	1496	0.1123
Step 3: Single C_P	NAT/30	490	204	−23.0	9.9	0.62	0.38	0.77	0.32	−0.9	2.3	1287	0.1049
RDO-2A-36.5													
Step 1: Calibration	−10/10	363	146	−16.8	7.3	0.69	0.32	0.80	0.25			5646	0.1056
	−20/20	387	140	−18.3	7.3	0.77	0.32	0.76	0.33			9999	0.1823
	−30/30	384	140	−18.0	7.1	0.75	0.32	0.78	0.28			9204	0.0946
	−50/50	378	143	−17.5	7.1	0.74	0.33	0.79	0.26			8376	0.0834
Step 2: Multiple C_P	NAT/30	401	150	−18.6	7.5	0.66	0.30	0.88	0.19	−5.6	3.6	843	0.1866
Step 3: Single C_P	NAT/30	480	228	−22.8	10.6	0.55	0.38	0.87	0.19	−6.9	5.6	908	0.1966
RDO-2A-87													
Step 1: Calibration	−10/10	289	76	−12.5	3.9	0.82	0.26	0.81	0.26			10000	0.2731
	−20/20	289	76	−12.6	3.9	0.81	0.26	0.81	0.27			10000	0.2339
	−30/30	289	75	−12.1	3.7	0.80	0.27	0.80	0.27			9910	0.1454
	−50/50	287	78	−12.5	3.8	0.80	0.26	0.82	0.24			8743	0.0890
Step 2: Multiple C_P	NAT/30	305	78	−13.4	3.9	0.78	0.25	0.82	0.23	−0.1	2.2	1900	0.1922
Step 3: Single C_P	NAT/30	516	202	−23.2	10.0	0.65	0.41	0.75	0.35	−0.2	2.8	2193	0.1929
VC-1-369.5													
Step 1: Calibration	−20/20	362	129	−15.9	6.4	0.77	0.32	0.76	0.33			9998	0.2147
	−30/30	359	121	−16.9	6.2	0.77	0.31	0.78	0.30			10000	0.3815
	−50/50	361	131	−15.5	6.3	0.76	0.33	0.75	0.33			10000	0.2388
Step 2: Multiple C_P	NAT/30	376	136	−16.3	6.7	0.70	0.31	0.83	0.24	−6.5	5.0	3178	0.4517
Step 3: Single C_P	NAT/30	483	251	−21.0	11.7	0.60	0.39	0.83	0.24	−7.2	5.0	2688	0.4550

The β and ξ values for samples RDO-2A-36.5 (Fig. 3.4), RDO-2A-2.5, RDO-2A-87, and VC-1-369.5 were determined using sample-specific ΔH and τ_0 values from Table 3.2 Peak Tg temperatures and experimental quench rates used for determining ΔH and $\tau 0$ from the Arrhenius relationship., known experimental heating (q_h) and cooling (q_c) rates, and solved using *CoolMonte*. The values are consistent across thermal treatments and are typically $\gtrsim 0.5$ for β and $\gtrsim 0.7$ for ξ (Tables 3.3). The values for β are unique for each sample despite very similar bulk compositions whereas ξ is consistent across all samples. The four sample-specific model parameters (ΔH, τ_0, β, and ξ) are now constrained.

The last remaining unknown model parameter is q_c for the initial C_P measurement through T_g that contains natural cooling information. Figures 3.5 (A, C, E) and 3.6 (A) show the result of fitting the initial C_P measurement using *CoolMonte* with sample-specific values of ΔH, τ_0, β, and ξ constrained using multiple thermal treatments. Peak height generally has an inverse relationship with cooling rate, where taller peaks correspond to slower cooling (Fig. 3.5). Quantitative cooling rates vary from ~0.6 K per second for samples RDO-2A-87 (Fig. 3.5E), to ~2 K per year for sample VC-1-369.5 (Fig. 3.6A).

3.4.3 Using a single C_P measurement to determine quantitative cooling rates

We then solved for all five unknown model parameters (ΔH, τ_0, β, ξ, and q_c) simultaneously using *CoolMonte* on the first C_P measurement of each sample through T_g (Fig. 3.5 B, D, F; 3.6B; Table 3.3). Again, sample RDO-2A-87 has the fastest predicted cooling rate of ~0.8 K per second, and VC-1-369.5 has the slowest cooling at ~10 K per year. Best fit, resulting RMSDs, and uncertainty envelopes are very similar between

calibrated (multiple C_P) and uncalibrated (single C_P) cooling rate estimates (Fig. 3.5 & 3.6), suggesting experimental signal quality is the largest contributor to uncertainties. Cooling rate estimates for both methods fall within uncertainty of the other (Fig. 3.7).

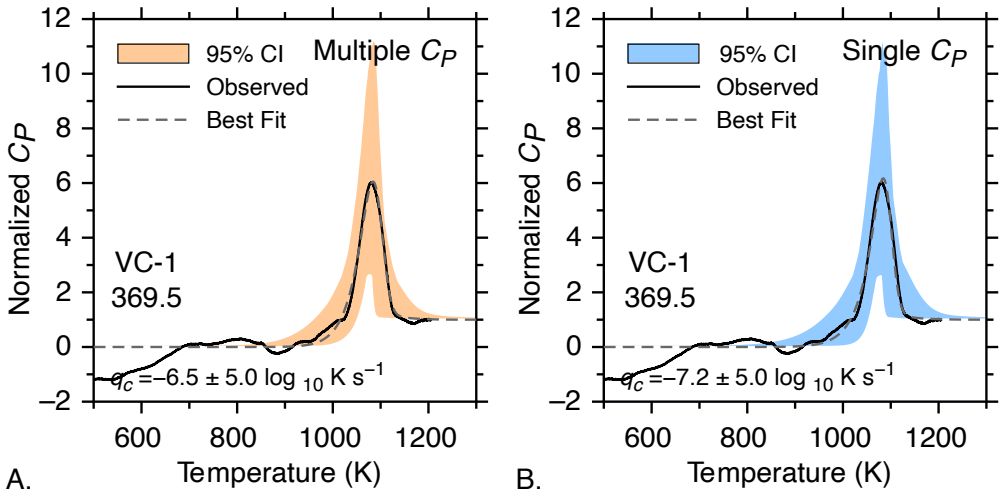

Figure 3.6 Quantitative cooling rates determined using CoolMonte for sample VC-1-369.5 with parameters constrained using multiple C_P measurements (A) and optimizations fitting a single C_P curve (B). Solid black line represents experimental C_P data, dashed gray line represents the best fit and 95% confidence interval is shown as fields correspond to the maximum and minimum value for models with RMSD ≤ two-times the lowest RMSD.

3.5 Discussion

3.5.1 Efficacy of determining cooling rates using a single C_P measurement

We have demonstrated that solving for five model parameters simultaneously using a single C_P curve and the *CoolMonte* algorithm produces comparable cooling rate estimates to those determined using multiple C_P measurements for natural samples. Advantages of being able to estimate cooling rates of natural glasses using a single C_P measurement include, 1) ability to more confidently measure samples prone to irreversible change (i.e., crystallization or volatile loss), and 2) determining up to five

cooling rates over the same period that it would have previously taken to determine one cooling rate. *CoolMonte* also standardizes and simplifies the modeling of experimental C_P data for determining natural cooling rates making it easier to collect and measure cooling rates at higher spatial resolutions, by processing more samples from a single locality in each time; estimating cooling rates from previously collected C_P data, not originally collected for the purposes of geospeedometry; and functioning as a standard characterization procedure when studying natural volcanic glasses. In effect, the energy barrier of using the TN-geospeedometer has been lowered.

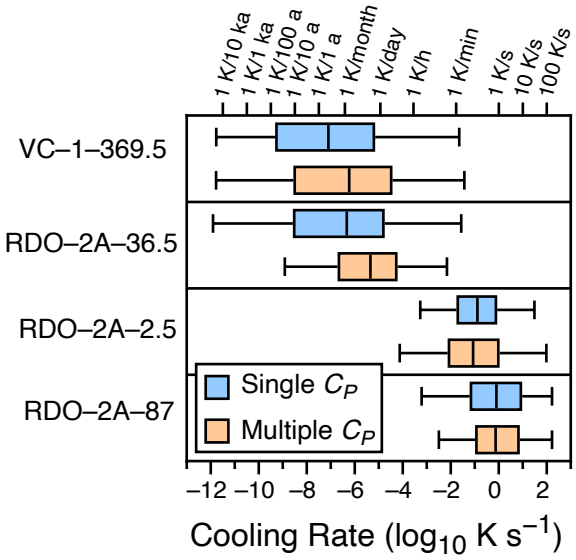

Figure 3.7. Box plot comparing natural cooling rate estimates for samples from Banco Bonito and Obsidian Dome comparing cooling rates constrained using multiple C_P measurements (orange) to those constrained using a single C_P curve (blue). Box plots are defined for this figure and additional figures as the line in the center of the box represents the median of the data, with the upper box boundary representing the 75th percentile, and the lower box boundary representing the 25th percentile, defined as the interquartile range. Whiskers, i.e., lines extending from the boxes, are terminated with line caps that represent the highest and lowest values that lie within a factor of 1.5 outside the interquartile range. Circles are outliers that exceed the interquartile range by a factor of 1.5 to 3.

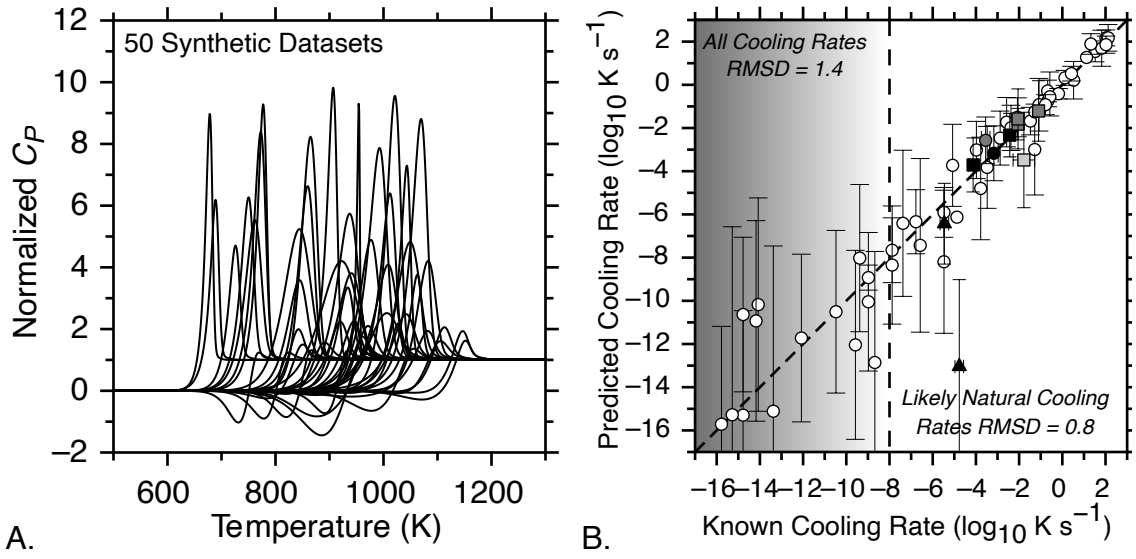

Figure 3.8 Assessment of *CoolMonte*. (A) Fifty normalized C_P curves generated using equations 3—6 with known input parameters. (B) Unity plot showing predicted vs. known cooling rates determined using *CoolMonte* for the 50 synthetic C_P curves (white circles) and previously published cooling rates (black and gray shapes). Error-bars represent two-times the standard deviation (2σ). Range of likely natural cooling rates (> 10^{-8} K s^{-1}) with an RMSD = 0.8 $\log_{10}$ K s^{-1} and for cooling rates of all 50 synthetic C_P has an RMSD = 1.7 $\log_{10}$ K s^{-1}. Shaded area in (B) represents range of unlikely natural cooling rates. Symbols for previously published cooling rates: Gottsmann and Dingwell (2001a = black square, 2001b = black circle, 2002 = black triangle); Wilding et al., (1996a = dark gray square, 2004 = dark gray circle); Lavallée et al., (2015 = light gray square).

The four natural obsidian samples presented in this study demonstrate the relative precision of using multiple C_P or single C_P measurements for determining natural cooling rates using *CoolMonte.* A way to assess the accuracy of *CoolMonte* is to generate synthetic normalized C_P curves using equations 3.3—3.6 with known input parameters and treat the synthetic data as unknowns. Fifty synthetic C_P curves (Fig. 3.8A) were generated and fit using *CoolMonte* as single unknown C_P curves. Results suggest known cooling rates $\gtrsim 10^{-8}$ K s^{-1} or ~0.31 K per year are reproduced well (RMSD = 0.8 $\log_{10}$ K s^{-1}; Fig. 3.8B) and more than cover the range of likely and previously reported natural cooling rates of rhyolite obsidians determined using the TN-geospeedometer (Wilding et

al., 1995; Gottsmann and Dingwell, 2001a; Gottsmann and Dingwell, 2001b; Gottsmann and Dingwell, 2002; Wilding et al, 2004). However, for cooling rates $\lesssim 10^{-8}$ K s^{-1} uncertainties increase with an RMSD = 1.4 $\log_{10}$ K s^{-1} for all 50 synthetic C_P curves. The increase in uncertainty as cooling rates decrease in figure 3.8B is expected because the number of potential parameter combinations that can match experimental data well should increase, resulting in larger uncertainties between known and predicted cooling rates.

We also tested *CoolMonte* by solving for natural cooling rates of previously published calorimetric data from Wilding et al., (1996a; 2004), Gottsmann and Dingwell (2001a; 2001b; 2002), and Lavallée et al., (2015) with corresponding cooling rates determined using the traditional implementation of the TN-geospeedometer (Fig. 3.8B). Nine out of 10 cooling rates determined using *CoolMonte* on previously published C_P data are within uncertainty of their reported natural cooling rates (Fig. 3.8B) The published cooling rate for sample UOBS1080 from Gottsmann and Dingwell (2002) was not reproduced well by *CoolMonte*. Our analysis yielded a convincing best fit but also a non-lognormal distribution resulting in an unlikely natural cooling rate of ~10^{-13} K s^{-1}. However, the normalized peak height observed for sample UOBS1080 (~7) suggests slower cooling than the published cooling rate (e.g., VC-1-369.5), but likely faster cooling than *CoolMonte*'s estimate.

3.5.2 Assessment of the model parameters

The five variables in equations 3.4, 3.5, and 3.6 affect the modeled C_P curve in two ways: 1) peak position and 2) curve shape. Parameters ΔH and τ_0 are linearly

correlated and shift the model peak to higher or lower temperature, ξ mostly controls whether the peak is broad or narrow, and q_c controls the peak height. The β parameter is unique because of how it affects both the peak position and shape, which

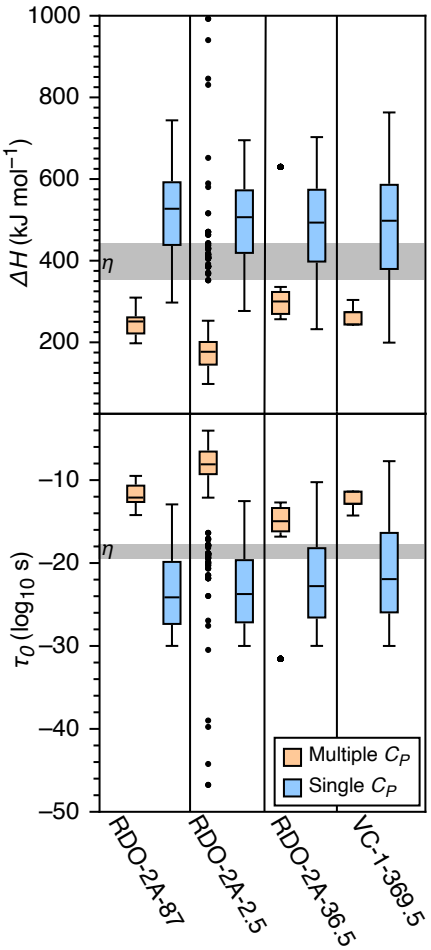

Figure 3.9 Boxplot of enthalpy of relaxation and limiting relaxation times; enthalpy of relaxation (ΔH; top) and limiting relaxation time (τ_0; bottom) comparing values determined using the Arrhenius relationship (left) and *CoolMonte* algorithm on a single C_P measurement (right) with natural cooling thermal history (q_c = unknown) for samples from Obsidian Dome and Banco Bonito. Gray field labelled "η" corresponds to estimated values of ΔH and τ_0 estimated using the viscosity model of Romine and Whittington (2015) for a rhyolite with water contents between 0.1 and 0.5 wt.% H_2O and an average shift factor of 10.5 for τ_0 from Stevenson et al., (1995) and Gottsmann et. al. (2002).

should make β the most important parameter to constrain when identifying cooling rates, however ξ was observed as the most consistent parameter between samples (Table 3.3) and was often correlated with cooling rate estimates.

Figure 3.9 compares values for ΔH and τ_0 constrained using the Arrhenius relationship (Eq. 3.7) to those resulting from using *CoolMonte* to solve a single C_P measurement. Differences exist between the results of the two methods, with *CoolMonte* systematically returning larger values for ΔH, and lower values of τ_0, compared to the Arrhenius relationship.

One concern regarding values for ΔH and τ_0 predicted using equation 3.7 is that the four samples used in this study are compositionally similar being relatively dry (<0.2 wt. % H_2O) high-silica rhyolitic obsidians, yet predicted values for ΔH and τ_0 vary significantly, with RDO-2A-2.5 having $\Delta H = 177$ kJ mol^{-1} and $\tau_0 = -8.0$ $\log_{10}$ s to RDO-2A-36.5 having $\Delta H = 300$ kJ mol^{-1} and $\tau_0 = -15.0$ $\log_{10}$ s. In contrast, values predicted using *CoolMonte* are very consistent with $\Delta H \simeq 525$ kJ mol^{-1} and $\tau_0 \simeq -24$ $\log_{10}$ s.

The principle of thermorheological simplicity (Narayanaswamy, 1988) suggests the equivalency of relaxation behavior across multiple material properties (e.g., shear viscosity and enthalpic relaxation) and Stevenson et al., (1995) and Gottsmann et al., (2002) demonstrated this principle for rhyolites. Therefore, we can use melt viscosity to estimate ΔH and τ_0 to compare to those estimated from calorimetric measurements. We used the viscosity model of Romine and Whittington (2015) for a rhyolite with 0.1 wt. % to 0.5 wt. % H_2O, at 0.1 MPa, over the temperature range 750°C to 900°C to estimate ΔH and an average shift factor of 10.5 (Stevenson et al., 1995; Gottsmann et al., 2002) to estimate τ_0. The ranges in ΔH and τ_0 from viscosity models are represented as gray fields

in figure 9. The medians of ΔH determined using the multiple C_P measurements and equation 3.7 are systematically lower than ΔH of shear viscosity and τ_0 values are greater than those estimated from the viscosity model. The ΔH values determined using a single C_P measurement with *CoolMonte* are systematically higher and τ_0 are systematically lower than those from the viscosity model but the values determined with *CoolMonte* are in better agreement with viscosity estimates than values determined using the Arrhenius equation (Eq. 3.7).

One possible explanation for the discrepancy between estimates is that, since the Arrhenius relationship is constrained using a very narrow range in experimentally matched heating and cooling rates (~10^1 K min^{-1}), and if the values for ΔH and τ_0 are actually non-Arrhenian, then C_P measurements with thermal histories outside of the calibration range might have significantly different values for ΔH and τ_0. However, if this were the case there would be a systematic relationship between predicted cooling rates and differences between ΔH and τ_0 values predicted from equation 3.7 and those predicted with *CoolMonte*, but this is not observed.

Another possible explanation includes the effects of thermal inertia during DSC measurements using relatively fast experimental heating rates (~50 K min^{-1}), which could systematically decrease ΔH and increase τ_0 values. However, total masses of reference materials used during scanning rate specific temperature calibrations are comparable to total masses used for natural samples, which should minimize the effects of thermal inertia during experimental measurements. Also, repeat measurements of the α-β transition of a reference quartz sample under identical conditions as natural obsidian samples show no discernable effects from thermal inertia (e.g., Fig. 3.2A).

A third possibility is that predicted values of τ_0, ΔH, and β are conflated with one another since all three affect the peak position in the relaxation model output, effectively obscuring the true values of these three parameters. One possible solution to this problem is to estimate τ_0 and ΔH using an appropriate viscosity model (Giordano et al., 2008; Romine and Whittington, 2015) and corresponding shift factors (Gottsmann et al., 2002) to fix τ_0 and ΔH and solve only for parameters β, ξ, and q_c. Another possible solution to this problem is to optimize parameters individually. Preliminary attempts to solve for each parameter individually using sample RDO-2A-36.5 show promising results, producing τ_0 and ΔH more like estimates from viscosity, without affecting cooling rate estimates. Future work will try to improve estimates of τ_0, ΔH, and β parameters using *CoolMonte*.

3.5.3 Exceptionally slow cooling of natural rhyolite obsidians

All previously published natural cooling rates of rhyolite and pantellerite obsidians determined using the TN-geospeedometer (Wilding et al., 1996a; Gottsmann and Dingwell, 2001a; Gottsmann and Dingwell 2001b; Gottsmann and Dingwell, 2002; Wilding et al., 2004) have been $\gtrsim 10^{-5}$ K s^{-1}. Two cooling rates determined in this study are slower than 10^{-5} K s^{-1} including samples RDO-2A-36.5 ($\sim 10^{-6}$ K s^{-1}) and VC-1-369.5 ($\sim 10^{-7}$ K s^{-1}; Fig. 3.7; Table 3.3), likely because Obsidian Dome and Banco Bonito are thicker than previously studied lavas.

Exceptionally slow cooling rates should trigger crystallization, but our samples remain glassy. Wilding et al. (2004) described the critical cooling rate (CCR) of albite as a proxy for anhydrous obsidian using classical nucleation theory (CNT; Volmer and

Weber, 1926; Becker and Döring, 1935; Turnbull and Fisher, 1949; Debenedetti, 1996) which yielded a CCR of $10^{-1.3}$ K s^{-1}. The estimated CCR is four to six orders of magnitude faster than cooling rates determined using the TN-geospeedometer, suggesting glassy obsidians with apparent cooling rates slower than the CCR should have experienced devitrification.

Quasi-isothermal annealing (Gottsmann et al., 2002; Wilding et al., 2004) is often invoked to explain the discrepancy between CCRs determined using CNT and quantitative cooling rates measured using the TN-geospeedometer. Quasi-isothermal annealing requires the glass to be reheated to elevated temperatures for a period so that the relaxation time of the glass is roughly the same as the time spent at high temperature to lower T_f, however temperatures cannot be so high or dwell times so long that the glass crystallizes. The most often cited mechanism responsible for buffering cooling and annealing the glass is the release of latent heat during the crystallization of the center of obsidian lavas.

However, some melts do not readily crystallize. Schairer and Bowen (1956) failed to crystallize albite from a Na_2O-Al_2O_3-SiO_2 melt held at 1025°C for five years. Also, a recent study by Rusiecka et al. (2020) expanded the range of possible natural CCRs using crystallization experiments of hydrated rhyolite obsidian. The authors found that CNT alone underestimated nucleation delay times and therefore overestimated CCRs compared to experimental observations and addressed this discrepancy by modifying CNT with diffuse interface theory (DIT). The modeled cooling of a rhyolite obsidian lava with 0.5 wt. % H_2O required a cooling rate of ~10^{-8} K s^{-1} at 30 m depth with the melt

undercooled by approximately −75 °C to nucleate feldspar crystals, which is significantly slower than previous estimates for a CCR.

Additionally, Romine et al., (2012) measured temperature-dependent thermal properties of variably hydrous rhyolitic obsidians and used them to model the emplacement of a 10-m wide glassy rhyolite sheet intruding country rock with an ambient temperature of 30°C. The authors found cooling rates as slow as ~10^{-5} K s^{-1} at T_g without the addition of latent heat of crystallization. Enlarging the model domain to thicknesses appropriate for subaerial obsidian lavas (50-150 m) and the inclusion of latent heat would likely result in slower predicted cooling rates. This suggests quantitative cooling rates determined for samples RDO-2A-36.5 and VC-1-369.5 using *CoolMonte* are possible in nature without invoking quasi-isothermal annealing. Lastly, *CoolMonte* enables rapid geospeedometric analysis of large, naturally cooled, spatially well-constrained samples from large silicic lava flows can be used to assess and validate conductive cooling models in the future.

3.6 Conclusion

We developed a time-saving numerical approach to determine quantitative cooling rates of natural glass samples, using a single C_P measurement. We find that natural cooling rates determined using the *CoolMonte* algorithm agree with traditionally determined and previously published quantitative cooling rates. Our new algorithm will make relaxational geospeedometry a more accessible method, enabling the characterization of cooling rates of natural samples over greater spatial distributions, and the extraction of cooling rate information from previously collected calorimetric scans.

Chapter 4

4. Experimental constraints on the thermal histories and emplacement dynamics of the rhyolitic obsidian lava Banco Bonito and the VC-1 Rhyolite, Valles Caldera, NM.

4.1 Abstract

Emplacement styles and associated mechanisms driving obsidian lava emplacement are still unclear despite many preserved examples around the world and recent observations made during two recent eruptions of rhyolite magma in Chile. The VC-1 drill core collected during the Continental Scientific Drilling Program from the Valles caldera, New Mexico sampled the entire thickness of two obsidian rhyolite units. Banco Bonito is a large (> 4 km^3; up to 150 m thick) obsidian coulée comparable to the lava from the 2011-2012 eruption of Cordón Caulle, and the VC-1 Rhyolite is a relatively thin (~20 m) obsidian rhyolite that is not exposed at the surface and has an uncertain emplacement history. Evidence of the emplacement style of Banco Bonito and the VC-1 Rhyolite is preserved as spatial trends in volatile content and thermal history as a function of depth. We sampled the entire thicknesses of Banco Bonito and the VC-1 Rhyolite to measure dissolved water concentrations and determine natural cooling rates as a function

of depth. We find that Banco Bonito was likely emplaced in an exogenous or "tank-tread" style because residual water concentrations are at or below predicted solubility values, and measured cooling rates match predicted cooling rates for a single flow unit cooling primarily through conduction. The VC-1 rhyolite was likely emplaced as an effusive lava, that was eroded and rehydrated likely by glaciation before being inundated by the Battleship Rock Ignimbrite. Our observations suggest that the behaviors observed during the 2011-2012 eruption of Cordón Caulle are likely not the result of endogenous inflation by the ingress of younger lava, but more likely vesiculation of modestly hydrated (~0.2 wt. %) obsidian during and post emplacement.

4.2 Introduction

Emplacement dynamics of obsidian lavas have often been inferred, but rarely observed. Detailed observations of eruption dynamics of a large obsidian coulée were first made at Puyehue-Cordón Caulle in 2011-2012 (Tuffen et al., 2013). The lava was seen both inflating (Farquharson et al., 2015) and advancing primarily via break-out lobe development (Tuffen et al., 2013; Magnall et al., 2017; Magnall et al., 2018). It is unclear whether those behaviors are ubiquitous to silicic lava flows, or unique to the 2011-2012 eruption of Puyehue-Cordón Caulle, and what mechanisms are responsible for the observed emplacement behaviors. The observations made during the 2011-2012 eruption of Cordón Caulle have challenged previously accepted ideas on the emplacement dynamics of silicic lavas.

Emplacement behaviors of silicic lavas can be described effectively by two end-member models. The first is a style called exogenous or "tank-tread" emplacement and is

characterized by younger lava being continuously emplaced on top of older lava, as the cold crust is passively carried before cascading over the flow front and eventually being overridden. This style typically occurs when the lava is "volume-limited", meaning the driving force of lava emplacement is effusion of new lava (Walker, 1971).

The second style is called endogenous inflation and is instead characterized by younger lava being forcefully injected into older lava, inflating the lava, insulated by a cool carapace. Younger lava eventually overcomes the strength of the outer carapace, breaking through and the lava advances primarily through break-out lobe development. This style of emplacement is typical when effusion rates are high, and the advance of the lava is slowed by the development of a firm outer carapace or flow front and is often referred to as "cooling-limited" (Walker, 1971).

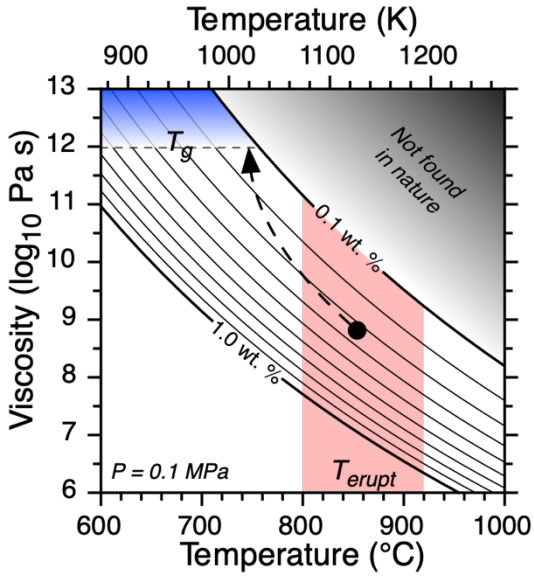

Figure 4.1 Viscosity of a rhyolite as a function of temperature and water concentration (0.1 wt. % contour lines) for a rhyolite at 0.1 MPa estimated using the viscosity model of Romine and Whittington (2015). Hypothetical evolution of the viscosity of an obsidian lava between an eruption temperature (T_{erupt}; ~850°C) and initial ~0.33 wt. % H_2O. As the lava advances, it cools and loses H_2O before quenching to a glass at T_g.

Both styles of emplacement are fundamentally controlled by the viscosity of the lava. Viscosity is a physical property that describes the deformation response of a material to an applied stress. The viscosity of silicate melts is a function of temperature (Bottinga and Weill 1972; Shaw 1972; Murase and McBirney, 1973), composition (Giordano et al., 2008), and texture which includes crystals and bubbles (Mader et al., 2013). Temperature generally exerts the greatest control on the viscosity of silicate melts, with a change in temperature from an estimated eruption temperature to the glass transition (T_g) resulting in a change of viscosity of up to 10^4 Pa s (Fig. 4.1). Composition is the next most important variable. After SiO_2, H_2O is the most important oxide for controlling the viscosity of a rhyolite and can change during eruptions of rhyolite magmas from ~5 wt. % to an equilibrium solubility of 0.1 wt. % at emplacement conditions. A change in H_2O from 0.3 wt. % to 0.1 wt. % at 850 °C results in a change of viscosity of ~$10^{1.5}$ Pa s (Romine and Whittington 2015; Fig. 4.1). Most obsidian lavas preserve low H_2O values (0.1 to 0.3 wt. %), yet small differences in dissolved H_2O and continued water loss during emplacement can result in dramatic contrasts in rheology and surface emplacement dynamics. Crystallization can also increase the bulk viscosity of a lava, however since obsidian lavas are largely crystal poor, this effect is minimized. Spatial distributions of volatile content and natural cooling rates through well-preserved obsidian lavas should therefore be useful for inferring emplacement dynamics of historical lavas.

Relaxation geospeedometry is a method that can extract cooling rates from volcanic glasses using the hysteresis observed when measuring the isobaric heat capacity of a volcanic glass (C_p) through the glass transition (T_g; Wilding et al., 1995). Relaxation

geospeedometry has been used to measure natural cooling rates of natural glasses of many compositions and geologic settings, including obsidian lavas (Wilding et al., 1995; Wilding et al., 1996; Gottsmann and Dingwell, 2001a; Gottsmann and Dingwell, 2001b; Gottsmann and Dingwell, 2002; Wilding et al., 2004). Kenderes and Whittington (2021) improved on previous implementations on relaxation geospeedometry by developing a Monte Carlo numerical solver that allows for determinations of natural cooling rates up to five times faster than the previous methods, enabling rapid cooling rate estimates of obsidians over greater spatial distributions. Volatile contents of rhyolite glasses are easily measured using Fourier-transform infrared spectroscopy (FTIR; Stolper, 1982; Newman et al., 1986).

Evidence of emplacement behaviors is contained within well-preserved examples of silicic lavas. For this study, we constrain the volatile content, and thermal history of Banco Bonito rhyolitic obsidian lava flow that erupted 68.3±1.5 ka from the Valles Caldera, NM (Zimmerer et al., 2016), and the VC-1 Rhyolite, a unit only observable in the VC-1 drill core from Valles caldera. Samples were acquired from the Continental Scientific Drilling Program (CDSP) drill core VC-1, which allowed us to analyze samples collected throughout the entire ~150 m thickness of the lava, and ~20 m of the VC-1 Rhyolite. We measured the amount and speciation of volatile oxides in obsidian samples using Fourier-transform infrared spectroscopy (FTIR) and constrained the thermal history by measuring natural cooling rates using relaxation geospeedometry. We modelled cooling rates of obsidian from Banco Bonito using both the multiple C_P method (Wilding et al., 1995) and the newly developed single C_P method (Kenderes and Whittington, 2021). Together, FTIR and relaxation geospeedometry datasets expose the

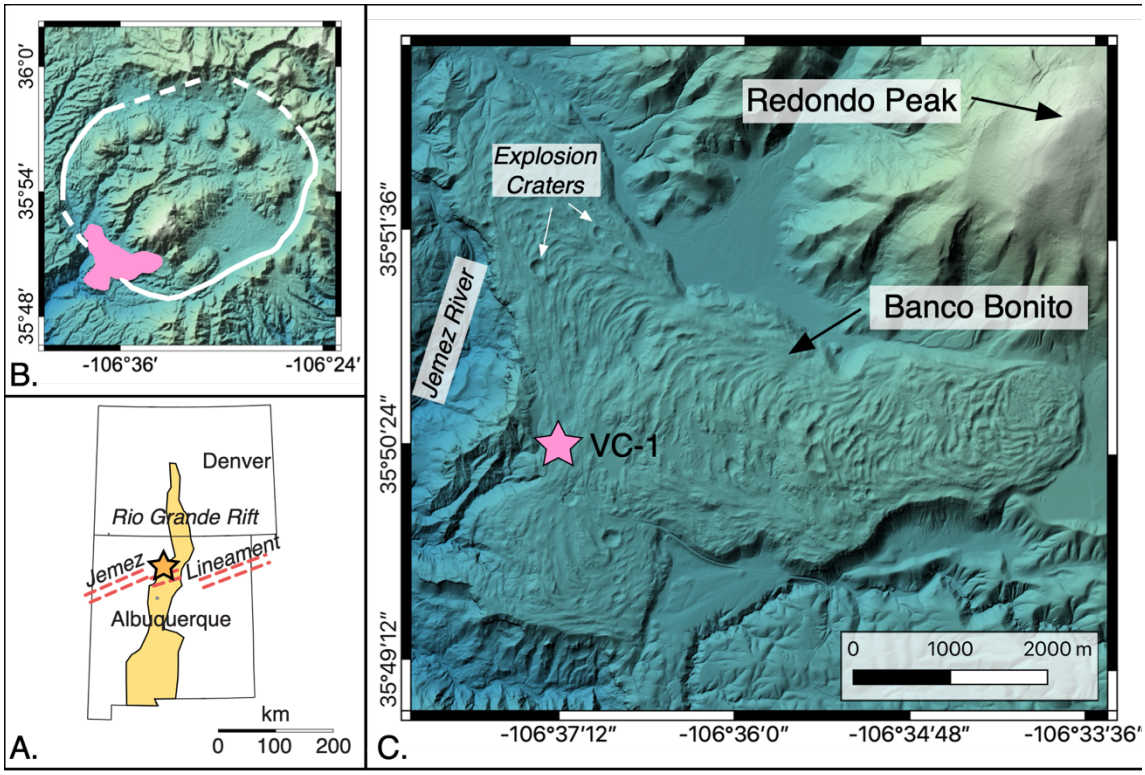

Figure 4.2 Regional map of Valles caldera. (A) Regional map showing the location of Valles caldera (orange star) at the junction of the Rio Grande Rift and Jemez Lineament. (B) Map of Valles caldera outlined in white that formed during the eruption of the Bandelier Tuff (1.74 Ma). (C) Map of Banco Bonito obsidian lava, Valles caldera, New Mexico. The location of VC-1 drill core (pink star) can be seen near the western flow margin where the Jemez River incises into the caldera.

thermo-rheological evolution of the effusive eruption of Banco Bonito and the VC-1 Rhyolite.

4.3 Geologic Background

Banco Bonito rhyolitic obsidian lava is the most recent eruptive product of Valles caldera, NM, erupted at 68.3 ± 1.5 ka ($^{40}Ar/^{39}Ar$ Sanidine; Zimmerer et al., 2016) and the older VC-1 Rhyolite is not exposed at the surface making determinations of its emplacement history difficult. Both units are in the Valles caldera, which is located is in the Jemez Mountains volcanic field of north-central New Mexico, where the Jemez

lineament and Rio Grande Rift intersect (Fig. 4.2A). The Jemez lineament includes a series of Quaternary to Tertiary volcanic fields that generally trend in a northeasterly direction (Wisniewski and Pazzaglia, 2002). The lineament is characterized by anomalously high heat flow and is believed to be a suture penetrating the lithosphere between the Yavapai and Mazatzal crust (Wisniewski and Pazzaglia, 2002; Magnani et al., 2004). The Rio Grande Rift is an active zone of Cenozoic-extension from Leadville, Colorado to Big Bend, Texas and Chihuahua, Mexico, more than 1000 km (Baldridge et al., 2006). Middle Miocene to Holocene basaltic volcanism along the Rio Grande Rift is associated with Basin and Range extension.

The Valles caldera is an important volcanic system as it is one of the three active caldera systems in the United States that has produced large Plinian, super-eruptions(s) that have emplaced >300 km^3 of pyroclastic material in the last 2 Ma (the others are Long Valley and Yellowstone calderas). Two caldera-forming eruptions have occurred at Valles caldera. The Toledo caldera was formed during the eruption of the 216-500 km^3 Otowi member of the Bandelier Tuff at 1.60 Ma (Wolff and Ramos, 2014; Cook et al., 2016). The most recent eruption produced the XX km^3 Tshirege member of the Bandelier Tuff at 1.256 ± 0.010 Ma (Fig. 4.2B; Phillips et al., 2007). The geography of the modern caldera is dominated by post-Tshirege units, including the 1000-m-tall Redondo Peak resurgent dome (Fig. 4.2C; Smith and Bailey, 1968) and a series of "moat rhyolites" erupted along the caldera's bounding ring fractures.

The East Fork Member of Valles caldera is the youngest post-Tshirege unit and was erupted along the southern boundary of the caldera. The East Fork Member includes the El Cajete pyroclastic beds and Battleship Rock Ignimbrite deposited around 74 ka, the

VC-1 Rhyolite, and Banco Bonito rhyolitic obsidian lava at 68.3±1.5 ka ($^{40}Ar/^{39}Ar$ Sanidine; Zimmerer et al., 2016). Banco Bonito advanced west from the vent, towards the caldera margin, and eventually bifurcated into two lobes. Total runout distances are 7.5 to 8 km, which Walker (1973) described as "unusually long" for a rhyolite lava. Banco Bonito is a large silicic lava with an observed thickness of ~150 meters (at the VC-1 drill core site), and an eruptive volume of ~4 km^3 (Wolff et al., 2011). The western margin of Banco Bonito has been incised by the Jemez River, and there is some evidence that the area has experienced glaciation (Fig. 4.2C; Wolff et al., 2011).

In August-September of 1984 the Continental Scientific Drilling Program (CSDP) drilled and collected the 856 m long VC-1 drill core. The core was collected in Valles caldera as part of an exploration for hydrothermal resources in the caldera (Goff et al., 1986). The site of the drill core is near the western flow margin of Banco Bonito (Fig. 4.2C), where the main flow bifurcates into two distinct lobes. The core intersects 4 units, all rhyolitic composition: Banco Bonito, Battleship Rock Tuff, VC-1 rhyolite, and Bandelier Tuff (Fig. 4.3). Rhyolite in the VC-1 drill core preserves many textures, which include fine vesicular pumice, coarse vesicular pumice, dense obsidian, crystalline rhyolite, rhyolite and obsidian breccia, and tuff.

Banco Bonito exhibits a similar pseudo-stratigraphy as described by Manley and Fink (1987) for drill cores collected at Obsidian Dome, Inyo Craters, CA (Fig. 4.3). The stratigraphy is defined by vesicularity and density. Fine vesicular pumice is light gray in color with porosity values ranging from 30-40%, densities >1000 kg m^{-3}, and has small uniform bubbles (<0.5 mm). Coarse vesicular pumice is typically dark gray with porosities up to 80%, densities <1000 kg m^{-3}, and bubbles of varying size and shape.

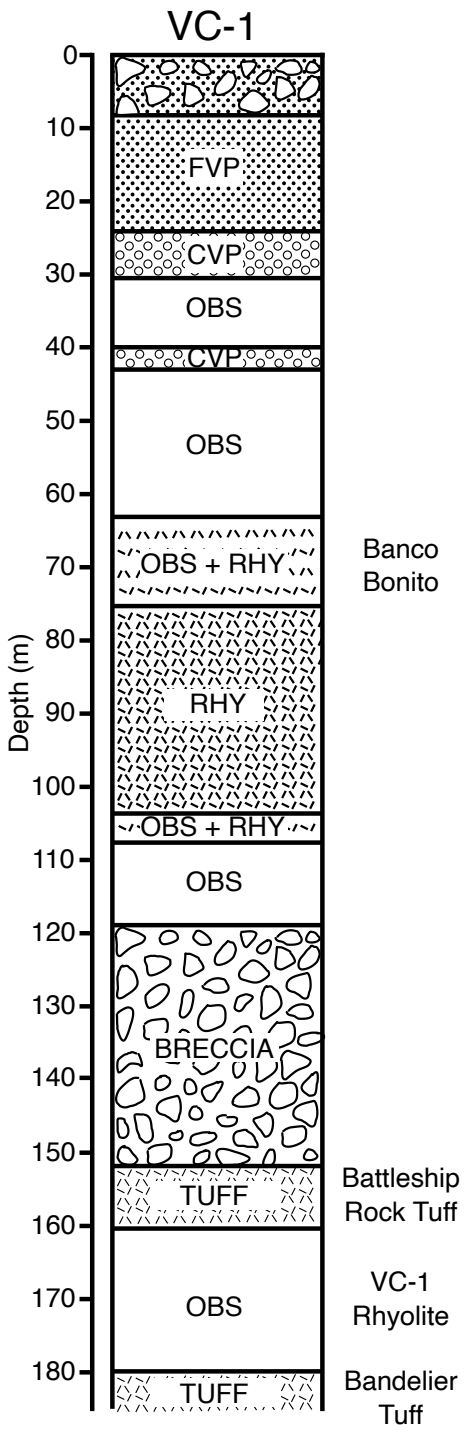

Figure 4.3. Stratigraphy of the VC-1 drill core with textures described by Fink and Manley (1987) including fine vesicular pumice (FVP), coarse vesicular pumice (CVP), dense obsidian (OBS), crystalline rhyolite (RHY), breccia (BRECCIA), and tuff (TUFF). Four lithostratigraphic units of the El Cajete series are observed in the first 185 m of drill including Banco Bonito (0 to 152 m), Battleship Rock Tuff (152 to 160 m), VC-1 Rhyolite (160 to 180 m) and Bandelier Tuff (>180 m).

Dense obsidian has densities ~2330 kg m^{-3}, porosities less than 10%, and can include large phenocrysts. The top of the core preserves unconsolidated rounded fine vesicular clasts in the first 8.2 meters, which is followed by 15.9 meters of consolidated fine vesicular pumice. At 24.1 m the first of two zones of coarse vesicular pumice are intersected, which are separated by a 9.5 m thick layer of dense obsidian. A second horizon of dense obsidian occurs from 42 to 63 m depth. Devitrified to crystalline rhyolite becomes interbedded with dense obsidian at intervals 63 to 75 m and 105 to 108 m. The fully crystalline rhyolite center of the flow exists in the 30 m interval between these gradational zones. Pervasively fractures dense obsidian occurs from 108 to 119 m depth, which transitions to a 32.9-m-thick basal breccia resting upon the Battleship Rock Tuff. The total thickness of Banco Bonito in the VC-1 drill core is 151.8 m.

In the core the Battleship Rock Tuff is 8.5 meters thick and has a sharp contact with the underlying VC-1 rhyolite. The VC-1 rhyolite was an unexpected stratigraphic unit that is only observed in the VC-1 drill core. The dominant texture of the VC-1 rhyolite is 19.5 m thick massive pervasively fractured dense obsidian. Flow banding foliation is observed to be subvertical near the top of the unit and transitions to sub-horizontal near the base of the unit. The Bandelier Tuff is first observed at 179.9 m and continues to ~300 m depth before the core samples volcaniclastics that predate the formation of the caldera and Paleozoic sedimentary rocks (Goff et al., 1986).

4.4 Materials and Methods

Forty-six drill core samples were collected from the VC-1 core at the Energy Geoscience Institute (EGI), University of Utah in Salt Lake City, UT. Thirty-seven

samples were collected from Banco Bonito, eight from the VC-1 Rhyolite, and one from the Battleship Rock tuff. Samples were chosen throughout the depth of the lavas and to best represent a full range of textures. Sample volume was limited to pieces smaller than 2x5x5 cm (roughly ¼ of the drill core diameter) to preserve the VC-1 core for future study. To prepare samples for analysis, a water-cooled, slow speed drill press with diamond-core drill bits with an interior diameter of ~6 mm was used to extract cores up to 15 mm in length. Two wafers, ~2 mm thick each, were then sectioned from the core using a slow-speed water-cooled saw. One wafer from each core was ground and doubly-polished into a disk ~100 μm thick for FTIR spectroscopy (von Aulock et al, 2014). The second wafer from each core was ground and polished to fit inside a Pt-Rh pan for thermal analysis using differential scanning calorimetry (DSC). The remainder of the core was saved for viscosity measurements.

4.4.1 FTIR measurements

Dissolved volatile contents of natural glass samples were measured using a Thermo Scientific Nicolet iN10 FTIR at Baylor University, TX. We used a spot size of 40 × 40 μm and recorded wavenumbers from 675 to 7200 cm^{-1}. Bubble and crystal-free domains were targeted for measurement. To check for homogeneity across the sample, three spatially distributed spots were measured. Apparent thicknesses at each spot were measured optically using a digital micrometer attached to the microscope stage by recording the distance between the focus at the top and bottom of the doubly-polished wafer. Apparent thicknesses must be converted to true thicknesses by correcting for the index of refraction for the glass (~1.5 for rhyolite), which shows little dependence on

glass composition and is calibrated using glasses of known thickness. Thickness measurements were repeated five times at each spot analysis to assess uncertainties in thickness measurements.

Concentrations of H_2O species can be measured in rhyolitic glasses using absorbances at the 4520 cm^{-1} (OH^-) and 5230 cm^{-1} (H_2O_{mol}). The sum of these species represents total water (H_2O_{tot}) content of the sample. We calculated the concentrations of H_2O_{tot}, OH^-, and H_2O_{mol} using the semi-empirical calibrations of Zhang et al. (1997). Absorbances at 2350 cm^{-1} (CO_2), and 3570 cm^{-1} (H_2O_{tot}) were converted to concentrations using the Beer-Lambert law (Stolper, 1982):

$$C = \frac{MW \cdot A}{\varepsilon \cdot \rho \cdot d} \cdot f \qquad 4.1$$

where C is the concentration of the volatile species (H_2O_{tot} in wt. %, and CO_2 in ppm), MW is the molecular weight of the volatile species in g mol^{-1}, A is absorbance, d is thickness in cm, ρ is glass density in g L^{-1}, ε is the molar absorptivity coefficient in L cm^{-1} mol^{-1}, and f is a dimensionless conversion factor (10^2 for H_2O and 10^6 for CO_2). An average glass density determined using the Archimedean principle (Avard and Whittington 2012) of samples VC-1-111.4 and -175.6 were 2356 ± 0.3 and 2397 ± 3.4 kg m^{-3} respectively, was used. The ε value for CO_2 is used 1214 ± 16 L cm^{-1} mol^{-1} from Behrens et al. (2004). The value of ε for H_2O_{tot} exhibits some dependence on speciation, and ranges from 56 ± 4 L cm^{-1} mol^{-1} when H_2O_{mol} is the dominant species to 100 ± 2 L cm^{-1} mol^{-1} when OH^- is the dominant species (Newman et al., 1986). Differences in ε result in small changes in the absolute values of H_2O_{tot} estimated, but spatial trends

remain unchanged if the chosen ε value remains constant. We are most interested in observable spatial trends in volatile content, therefore we opted to minimize the difference between H_2O_{tot} values determined using the 3570 cm^{-1} wavenumber and the absorbances observed at the 5230 cm^{-1} and 4520 cm^{-1} wavenumbers by using $\varepsilon = 73 \pm 4$ L cm^{-1} mol^{-1}.

Experimental uncertainties for volatile concentrations and species calculations were propagated using a generalized form of the variance equation (Ku, 1966):

$$\sigma_f = \sqrt{\sum_1^n \left(\frac{\partial f}{\partial x_n}\sigma_{x_n}\right)^2} \qquad 4.2$$

where σ_f represents the total uncertainty on a function f, x_n represents a variable in function f, and σ_{xn} represents uncertainty on a given variable of f.

4.4.2 Relaxation Geospeedometry

We measured the isobaric C_P of 15 glasses and one tuff using a Netzsch Pegasus 404F1 differential scanning calorimeter (DSC) calibrated using melting points and enthalpies of fusion of metals In, Sn, Zn, Al, and Au. Measurements were conducted using a Pt-Rh sample crucible. The first measurement through T_g for each sample started at 50°C and was heated at 30 K min^{-1} to ~50 °C above T_g before cooling at a controlled rate of −30 K min^{-1}. Next, four to five measurements were performed again starting at room temperature and heated at a rate equal to the previous measurements, however, cooling rates were implemented in the order of −30/+30, −50/+50, −20/+20, −40/+40, −10/+10 K min^{-1} to a temperature ~50°C above T_g. The matched rates were completed

non-sequentially to monitor for irreversible changes in the sample between measurements.

The C_P of a glass can be used to estimate its cooling rate from an initial melt because C_P is the derivative of the structurally dependent property enthalpy (H). The fictive temperature (T_f) is a convenient way to model the structural contributions to relaxation of a structurally dependent property (Moynihan, 1995) which can be modeled as a function of temperature with the following equations (Narayanaswamy 1971; Narayanaswamy, 1988):

$$\tau_k = \tau_0 \, exp\left[\frac{\xi \Delta H}{RT} + \frac{(1-\xi)\Delta H}{RT_{f_{k-1}}}\right] \tag{4.3}$$

and (DeBolt et al., 1976):

$$T_{f_m} = T_0 + \sum_{j=1}^{m} \left(T_{f_{j-1}} - T_j\right)\left[1 - e^{-\left(\sum_{k=j}^{m} \Delta T_k / |q_k| \tau_k\right)^{\beta}}\right] \tag{4.4}$$

where q_k (K s^{-1}) is the heating or cooling rate, τ_0 (s) is the limiting relaxation time, ΔH (kJ mol^{-1}) is the enthalpy of relaxation, ξ and β are empirical relaxation parameters. Additional details of the method using the specific Tool-Narayanaswamy geospeedometer can be found in Kenderes and Whittington (2021).

Previous studies that have applied relaxation geospeedometry to natural volcanic systems using the Tool-Narayanaswamy geospeedometer have required repeat C_P measurements of the same sample with controlled experimental thermal histories. Repeat measurements are used to constrain four model parameters, however, Kenderes and Whittington (2021) demonstrated that similar natural cooling rate estimates can be

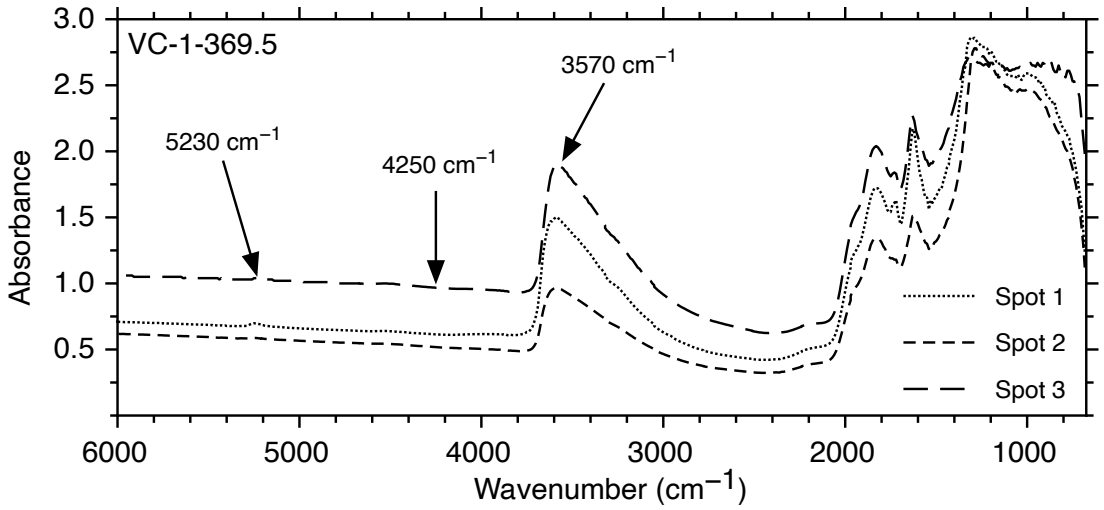

Figure 4.4 FTIR Absorbance spectra. Three absorbance spectra collected for sample VC-1-369.5 using Fourier-transform infrared spectroscopy (FTIR). Peaks observed at 3570 cm^{-1}, 4250 cm^{-1}, and 5230 cm^{-1} are used to measure the concentration of volatile species.

identified using a single C_P measurement. Following this method, the five unknown parameters must be solved simultaneously using a numerical solver called *CoolMonte* written in MATLAB. To compare both approaches, 6 of the 16 cooling rates herein were calibrated using multiple C_P measurements and using a single C_P measurement. The cooling rates of the remaining 10 samples were identified using only a single C_P measurement.

Propagating uncertainties for modeled natural cooling rates using equations 4.3 & 4.4 is cumbersome because of the nature of equations 4.3 & 4.4. Instead, *CoolMonte* uses a Monte Carlo approach to solve for cooling rates, generating distributions of optimal model parameters. Reported natural cooling rates represent the mean of the distributions. The reported 2σ uncertainties represent two times the standard deviation of those distributions output by *CoolMonte*.

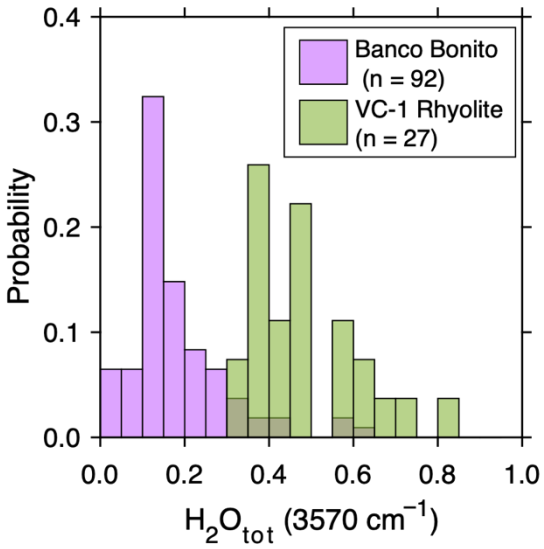

Figure 4.5. Probability density histogram of water concentrations.H_2O_{tot} (3570 cm^{-1}) values for Banco Bonito (n = 92) and VC-1 rhyolite (n = 27).

4.5 Results

4.5.1 H_2O concentrations of Banco Bonito and the VC-1 Rhyolite

We measured 135 absorbances from 46 glassy samples from the VC-1 drill core (Table 4.1). Of the 135 absorbance spectra measured, 119 spectra had measurable peaks at 3570 cm^{-1}, 92 at 4520 cm^{-1}, 45 at 5230 cm^{-1}, and four at the 2350 cm^{-1} wavenumbers (Fig. 4.4). The samples with measurable peaks at the 5230 cm^{-1} and 2350 cm^{-1} wavenumbers are interpreted as having been rehydrated, likely by hydrothermal fluids.

Figure 4.5 shows a probability density histogram showing the differences in measured H_2O_{tot} values for Banco Bonito and the VC-1 Rhyolite. The average H_2O_{tot} value determined using the 3570 cm^{-1} peak is 0.18 wt. % from Banco Bonito, and 0.51 wt. % from the VC-1 Rhyolite.

Table 4.1 Water concentrations (wt. %) for samples from the VC-1 drill core.

Sample*	Depth (m)	H_2O_{tot}[a] (3570 cm^{-1})	±	H_2O_{tot}[b]	±	H_2O_{mol}[b]	±	OH^{-}[b]	±
Banco Bonito									
VC-1-58.7a	17.9			6.94	0.01	6.37	1.08	0.56	0.18
VC-1-58.7b	17.9			4.57	0.00	4.27	0.88	0.30	0.07
VC-1-58.7c	17.9			6.23	0.01	5.74	1.64	0.49	0.15
VC-1-69.5a	21.2			3.91	0.00	3.59	0.33	0.32	0.06
VC-1-69.5b	21.2			2.14	0.00	1.99	0.19	0.16	0.02
VC-1-69.5c	21.2			1.83	0.00	1.54	0.17	0.29	0.04
VC-1-79.0a	24.1	0.15	0.01	0.13	0.00	0.03		0.09	0.01
VC-1-79.0b	24.1	0.31	0.01	0.34	0.00	0.25	0.01	0.10	0.01
VC-1-79.0c	24.1			1.20	0.00	1.00	0.05	0.20	0.02
VC-1-84a	25.6			2.17	0.00	1.95	0.10	0.21	0.02
VC-1-84b	25.6			0.94	0.00	0.78	0.04	0.16	0.01
VC-1-84c	25.6			1.33	0.00	1.12	0.06	0.21	0.02
VC-1-87.5a	26.7			3.23	0.00	3.03	0.15	0.20	0.03
VC-1-87.5b	26.7			3.80	0.00	3.63	0.18	0.17	0.03
VC-1-87.5c	26.7			3.39	0.00	3.24	0.16	0.15	0.02
VC-1-97a	29.6	0.04	0.02	0.06	0.00	0.06			
VC-1-97b	29.6	0.02	0.01	0.07	0.00			0.07	0.00
VC-1-97c	29.6			0.78	0.00	0.60	0.05	0.17	0.02
VC-1-111.4a	34.0	0.14	0.02	0.09	0.00			0.09	0.01
VC-1-111.4b	34.0	0.15	0.02	0.09	0.00			0.09	0.01
VC-1-111.4c	34.0	0.13	0.02	0.11	0.00			0.11	0.01
VC-1-119.8a	36.5	0.11	0.01	0.10	0.00			0.10	0.01
VC-1-119.8b	36.5	0.11	0.01	0.08	0.00			0.08	0.01
VC-1-119.8c	36.5	0.11	0.02	0.09	0.00			0.09	0.01
VC-1-125.2a	38.2	0.14	0.03	0.10	0.00			0.10	0.01
VC-1-125.2b	38.2	0.14	0.02	0.09	0.00			0.09	0.01
VC-1-125.2c	38.2	0.14	0.02	0.09	0.00			0.09	0.01
VC-1-131.4a	40.1	0.15	0.02	0.11	0.00			0.11	0.01
VC-1-131.4b	40.1	0.13	0.02	0.10	0.00			0.10	0.01
VC-1-131.4c	40.1	0.14	0.01	0.10	0.00			0.10	0.01
VC-1-141.2a	43.0	0.19	0.05						
VC-1-141.2b	43.0	0.22	0.05						
VC-1-141.2c	43.0	0.23	0.06						
VC-1-143.2a	43.7	0.15	0.03	0.09	0.00			0.09	0.01
VC-1-143.2b	43.7	0.15	0.02	0.07	0.00			0.07	0.00
VC-1-143.2c	43.7	0.14	0.02	0.12	0.00			0.12	0.01
VC-1-156.2a	47.6	0.10	0.04						
VC-1-156.2b	47.6	0.12	0.06						
VC-1-156.2c	47.6	0.14	0.07						
VC-1-160.4a	48.9	0.27	0.04						
VC-1-160.4b	48.9	0.28	0.07						
VC-1-160.4c	48.9	0.28	0.05						
VC-1-165.4a	50.4	0.15	0.06						
VC-1-165.4b	50.4	0.16	0.04						
VC-1-165.4c	50.4	0.12	0.04						
VC-1-169a	51.5	0.13	0.02	0.08	0.00			0.08	0.01
VC-1-169b	51.5	0.15	0.02	0.13	0.00			0.13	0.01
VC-1-169c	51.5	0.13	0.03	0.13	0.00			0.13	0.01
VC-1-175.6a	53.5	0.12	0.03						
VC-1-175.6b	53.5	0.11	0.04						

VC-1-175.6c	53.5	0.22	0.04						
VC-1-178.6a	54.5	0.10	0.04	0.10	0.00			0.10	0.01
VC-1-178.6b	54.5	0.11	0.05	0.10	0.00			0.10	0.01
VC-1-178.6c	54.5	0.11	0.04	0.14	0.00			0.14	0.01
VC-1-181.6a	55.4	0.15	0.04	0.18	0.00			0.18	0.02
VC-1-181.6b	55.4	0.15	0.02	0.11	0.00			0.11	0.01
VC-1-181.6c	55.4	0.15	0.02	0.10	0.00			0.10	0.01
VC-1-190.8a	58.2	0.27	0.01	0.41	0.00	0.40	0.02	0.01	0.00
VC-1-190.8b	58.2	0.02	0.02						
VC-1-190.8c	58.2	0.01	0.01						
VC-1-201.9a	61.6	0.17	0.04	0.14	0.00			0.14	0.01
VC-1-201.9b	61.6	0.18	0.03	0.15	0.00			0.15	0.01
VC-1-201.9c	61.6	0.18	0.02	0.11	0.00			0.11	0.01
VC-1-216.8a	66.1	0.10	0.06						
VC-1-216.8b	66.1	0.22	0.03						
VC-1-216.8c	66.1	0.09	0.05						
VC-1-220.1a	67.1	0.22	0.03	0.32	0.00	0.21	0.01	0.11	0.01
VC-1-220.1b	67.1	0.33	0.12	0.66	0.00	0.55	0.07	0.11	0.01
VC-1-220.1c	67.1	0.24	0.05	0.43	0.00	0.23	0.02	0.20	0.02
VC-1-230.4a	70.2	0.11	0.08						
VC-1-230.4b	70.2	0.23	0.02						
VC-1-230.4c	70.2	0.14	0.02	0.07	0.00			0.07	0.01
VC-1-240a	73.2	0.05	0.04						
VC-1-240b	73.2	0.05	0.03						
VC-1-240c	73.2	0.05	0.05						
VC-1-299.6a	91.3	0.06	0.17						
VC-1-299.6b	91.3	0.03	0.07						
VC-1-299.6c	91.3	0.04	0.36						
VC-1-342.8a	104.5	0.57	0.09	0.29	0.00			0.29	0.05
VC-1-342.8b	104.5	0.32	0.04	0.23	0.00			0.23	0.02
VC-1-342.8c	104.5	0.40	0.04	0.17	0.00			0.17	0.02
VC-1-354.8a	108.2	0.59	0.07	0.76	0.00	0.63	0.08	0.13	0.02
VC-1-354.8b	108.2	0.18	0.01	0.11	0.00			0.11	0.01
VC-1-354.8c	108.2	0.44	0.05	0.48	0.00	0.30	0.02	0.18	0.02
VC-1-369.5a	112.7	0.43	0.03	0.70	0.00	0.56	0.03	0.14	0.01
VC-1-369.5b	112.7	0.28	0.03	0.33	0.00	0.18	0.01	0.15	0.01
VC-1-369.5c	112.7	0.62	0.07	0.60	0.00	0.30	0.03	0.30	0.04
VC-1-379.6a	115.7	0.14	0.07	0.03	0.00			0.03	0.00
VC-1-379.6b	115.7	0.17	0.08	0.10	0.00			0.10	0.01
VC-1-379.6c	115.7	0.13	0.18	0.16	0.00			0.16	0.02
VC-1-394.7a	120.3	0.11	0.08	0.19	0.00			0.19	0.02
VC-1-394.7b	120.3	0.13	0.08	0.20	0.00			0.20	0.02
VC-1-394.7c	120.3	0.13	0.06	0.29	0.00			0.29	0.02
VC-1-407.0a	124.1	0.30	0.06	0.42	0.00	0.25	0.02	0.17	0.02
VC-1-407.0b	124.1	0.19	0.02	0.23	0.00	0.13	0.01	0.10	0.01
VC-1-407.0c	124.1	0.18	0.02	0.16	0.00	0.05	0.00	0.11	0.01
VC-1-417a	127.1	0.11	0.12						
VC-1-417b	127.1	0.11	0.08	0.14	0.00	0.04	0.00	0.10	0.01
VC-1-417c	127.1	0.09	0.07						
VC-1-427a	130.2	0.25	0.09						
VC-1-427b	130.2	0.24	0.08						
VC-1-456a	139.0	0.15	0.05						
VC-1-456b	139.0	0.19	0.05						
VC-1-456c	139.0	0.27	0.05						

VC-1-472.0a	143.9	0.23	0.05						
VC-1-472.0c	143.9	0.39	0.11	0.51	0.00	0.42	0.07	0.10	0.02
VC-1-486.8a	148.4			2.45	0.00	2.45	0.26		
VC-1-486.8c	148.4		0.04	2.57	0.00	2.40	0.16	0.17	0.02
VC-1 Rhyolite									
VC-1-529a	161.3	0.41	0.05	0.41	0.00	0.10	0.01	0.31	0.02
VC-1-529b	161.3	0.47	0.04	0.35	0.00	0.07	0.00	0.28	0.02
VC-1-529c	161.3	0.35	0.08	0.68	0.00	0.21	0.02	0.48	0.06
VC-1-532a	162.2	0.42	0.05	0.65	0.00	0.22	0.01	0.42	0.03
VC-1-532b	162.2	0.46	0.05	1.08	0.00	0.71	0.04	0.37	0.03
VC-1-532c	162.2	0.39	0.05	0.30	0.00			0.30	0.02
VC-1-534a	162.8	0.41	0.12		0.00				
VC-1-534b	162.8	0.33	0.34	0.24	0.00			0.24	0.06
VC-1-534c	162.8	0.38	0.11	0.31	0.00			0.31	0.02
VC-1-539a	164.3	0.85	0.20	0.95	0.00	0.30	0.02	0.65	0.07
VC-1-539b	164.3	0.63	0.21	0.38	0.00	0.11	0.02	0.28	0.05
VC-1-539c	164.3	0.58	0.07	0.52	0.00	0.14	0.01	0.39	0.03
VC-1-542a	165.2	0.62	0.07	0.69	0.00	0.19	0.01	0.50	0.04
VC-1-542b	165.2	0.60	0.09	0.38	0.00	0.08	0.01	0.30	0.03
VC-1-542c	165.2	0.56	0.06		0.00				
VC-1-553a	168.6	1.38	0.17	1.07	0.00	0.52	0.06	0.55	0.07
VC-1-553b	168.6	0.70	0.04	0.70	0.00	0.17	0.01	0.53	0.04
VC-1-553c	168.6	0.67	0.07	0.75	0.00			0.75	0.08
VC-1-565a	172.3	0.37	0.14	0.25	0.00			0.25	0.03
VC-1-565b	172.3	0.36	0.07	0.27	0.00			0.27	0.02
VC-1-565c	172.3	0.37	0.06	0.28	0.00			0.28	0.02
VC-1-573a	174.7	0.36	0.01	0.38	0.00			0.38	0.03
VC-1-573b	174.7	0.35	0.02	0.25	0.00			0.25	0.02
VC-1-573c	174.7	0.45	0.02	0.31	0.00			0.31	0.03
VC-1-587.6a	179.1	0.47	0.38		0.00				
VC-1-587.6b	179.1	0.48	0.35		0.00				
VC-1-587.6c	179.1	0.47	0.41		0.00				

*a, b, or c suffixes represent different spot analyses on the same sample.

[c]concentrations determined using the Beer-Lambert law

[b]concentrations determined using the empirical calibrations of Zhang et al., (2007)

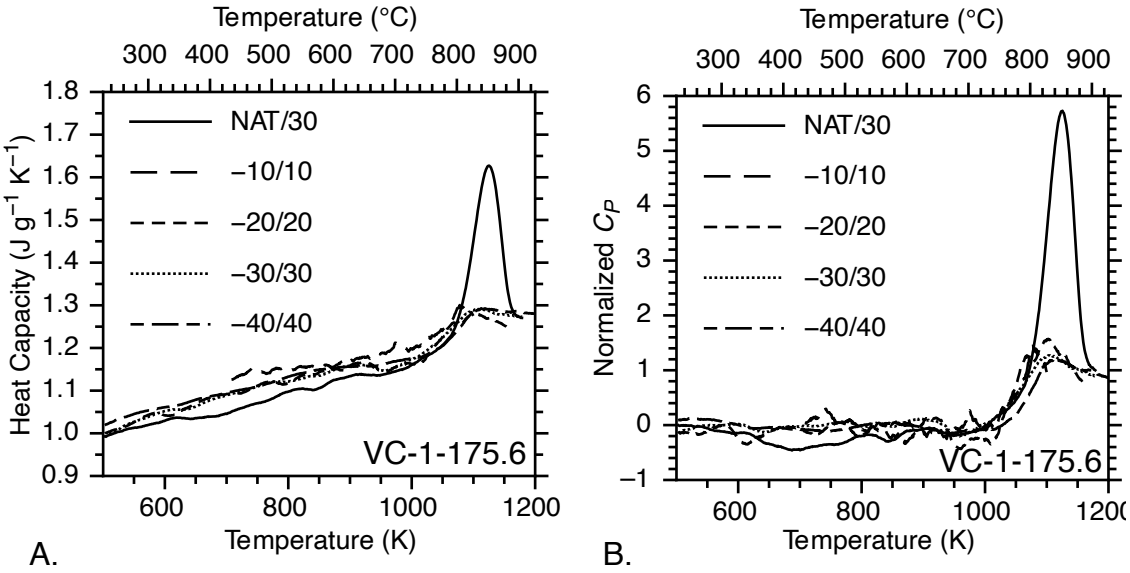

Figure 4.6 Isobaric heat capacity as a function of temperature. Isobaric heat capacity (C_P; A) and normalized C_P (B) curves for sample VC-1-175.6 for use with the Tool-Narayanaswamy (TN) geospeedometer to estimate natural cooling rates.

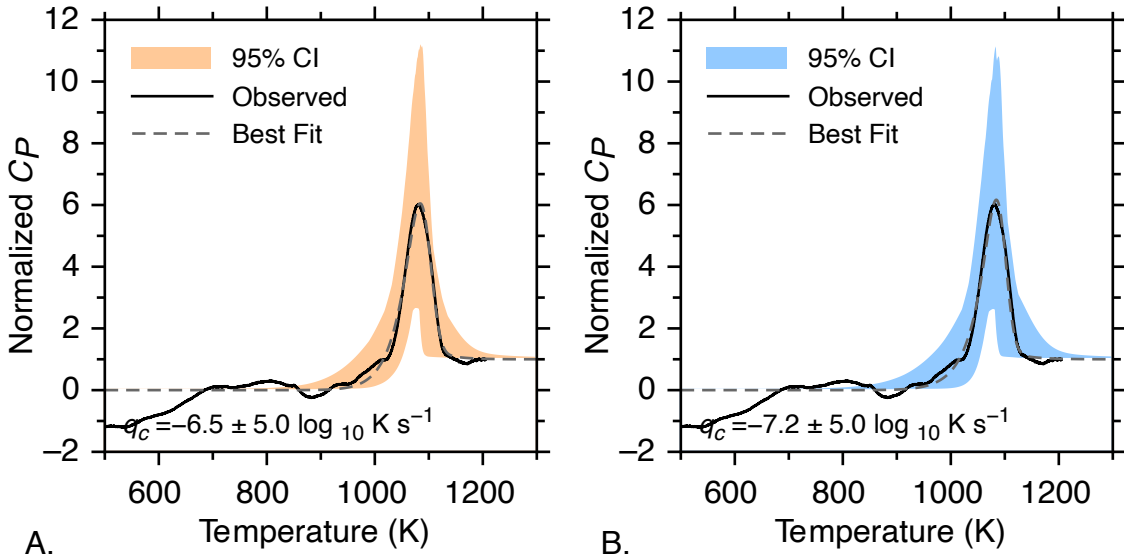

Figure 4.7 Natural cooling rates determined using CoolMonte for sample VC-1-369.5 using multiple C_P measurements (A) and a single C_P curve (B) with best fit ± 2σ uncertainty envelopes.

4.5.2 Natural cooling rates from the VC-1 drill core

Twenty-two natural cooling rates were determined including 13 glassy samples from Banco Bonito (Fig. 4.6, Table 4.2), one tuffaceous sample from the Battleship Rock

Tuff, and eight glassy samples from the VC-1 Rhyolite. Six natural cooling rates from Banco Bonito were determined using both multiple C_P measurements and a single C_P measurement. Five of the six cooling rates determined by both methods are within 1 log unit of each other. Figure 4.7 compares the results determined using a single C_P measurement vs multiple C_P measurements for sample VC-1-175.6, showing both methods produce cooling rate estimates within 0.7 log units of each other. Estimated 2σ uncertainties are very sensitive to the lowest achievable RMSD, which represents the contributions of signal to noise ratio and precision of fitting the relaxation model to experimental data. If the relaxation model deviates from normalized heat capacity data at low and high temperatures, the RMSD increases leading to larger uncertainties.

4.5.3 Variations in volatile content and thermal history as a function of depth

The emplacement dynamics of obsidian lavas are controlled by the thermal and compositional evolution of the lava. The depth profiles of H_2O and natural cooling rates can be used to constrain the emplacement dynamics of Banco Bonito and the VC-1 Rhyolite. The pseudo-stratigraphy, volatile content, thermal history, and modeled viscosity of samples from the VC-1 drill core are summarized in figure 4.8.

Banco Bonito (0-150 m) exhibits the generalized stratigraphy described by Manley and Fink (1987) where with increasing depth we expect to see (1) fine vesicular pumice near the surface, (2) a dense obsidian layer, (3) a coarse vesicular pumice layer, (4) a second dense obsidian layer, (5) syn- to post-emplacement rhyolite core, (6) a third dense obsidian layer, and (7) a basal breccia. The VC-1 Rhyolite is unique however, because the entire thickness is composed of dense obsidian (OBS; Fig. 4.8A).

Table 4.2 Natural cooling rates determined for samples from the VC-1 drill core using single C_P and multiple C_P measurements.

		Single C_P		Multiple C_P	
Sample	Depth (m)	$\log_{10}$ K s^{-1}	±	$\log_{10}$ K s^{-1}	±
Banco Bonito					
VC-1-37	11.3	−0.8	2.9		
VC-1-79	24.1	−0.6	1.9	0.3	2.4
VC-1-111.4	34.0	−13.0	3.7	−13.3	3.9
VC-1-175.6	53.5	−9.1	5.7	−12.3	5.3
VC-1-230.4	70.2	−13.5	3.2	−12.9	4.1
VC-1-342.8	104.5	−3.0	3.4		
VC-1-356.8	108.8	−8.9	3.7		
VC-1-369.5	112.7	−7.2	5.0	−6.5	5.0
VC-1-379.6	115.7	−3.0	6.7		
VC-1-394.7	117.3	−7.5	6.3		
VC-1-394.7	120.3	−4.3	5.3		
VC-1-407	124.1	−12.3	4.3		
VC-1-486.5	148.3	1.7	0.8	1.6	0.7
Battleship Rock Tuff					
VC-1-522	159.1	−0.3	1.8		
VC-1 Rhyolite					
VC-1-529	161.3	−13.3	4.4		
VC-1-532	162.2	−12.7	4.3		
VC-1-534	162.8	−12.9	4.2		
VC-1-539	164.3	−10.8	5.3		
VC-1-542	165.2	−11.9	4.4		
VC-1-553	168.6	−12.5	4.4		
VC-1-565	172.3	−13.2	3.7		
VC-1-587	179.0	−1.0	3.7		

The H_2O concentrations of samples from Banco Bonito are relatively dry being < 0.2 wt. % on average and generally increase with increasing depth following predicted solubility limits using the model of Liu et al., (2005) assuming lithostatic pressure and

temperatures ranging from 700°C to 1000°C (Fig. 4.8B) until intersecting the basal breccia at ~110 m depth. The VC-1 Rhyolite H_2O concentrations, however, exceed the solubility limits using the same assumptions and solubility model.

Figure 4.8C shows the variations in natural cooling rates as a function of depth through the VC-1 drill core. Banco Bonito shows evidence of having cooled quickly near the surface (~0.1 K s^{-1}) and the base of the flow (~50 K s^{-1}), and more slowly in the flow interior (< 1 K a^{-1}). Cooling rates determined using a one-dimensional finite difference conductive cooling model using temperature dependent thermal properties (i.e., thermal diffusivity and heat capacity, Romine et al. 2012) is compared to experimentally determined natural cooling rates in figure 4.8C. Experimental cooling rates occasionally are slower than predicted by the conductive cooling model in the flow interior and are faster at the top and bottom of the flow. This discrepancy is likely due to the contribution of latent heat of crystallization (ΔH_{crys}), slowing cooling in the flow interior, and forced or free convective cooling of the surface of the flow (ΔQ_{conv}), leading to faster cooling rates. Exogenous emplacement causes the surface of the lava, which should cool the quickest, to eventually fracture and cascade over the flow front and be overridden, preserving fast cooling rates in the basal breccia.

One natural cooling rate was determined for the ~8 m thick Battleship Rock tuff. A cooling rate of ~0.5 K s^{-1} was determined using a single C_P measurement. Lavallee et al., (2015) determined the natural cooling rate of the rheomorphic ignimbrite at Grey's Landing, ID and determined a cooling rate approximately two orders of magnitude slower (~0.002 K s^{-1}) than what we observe for the Battleship Rock Tuff. This

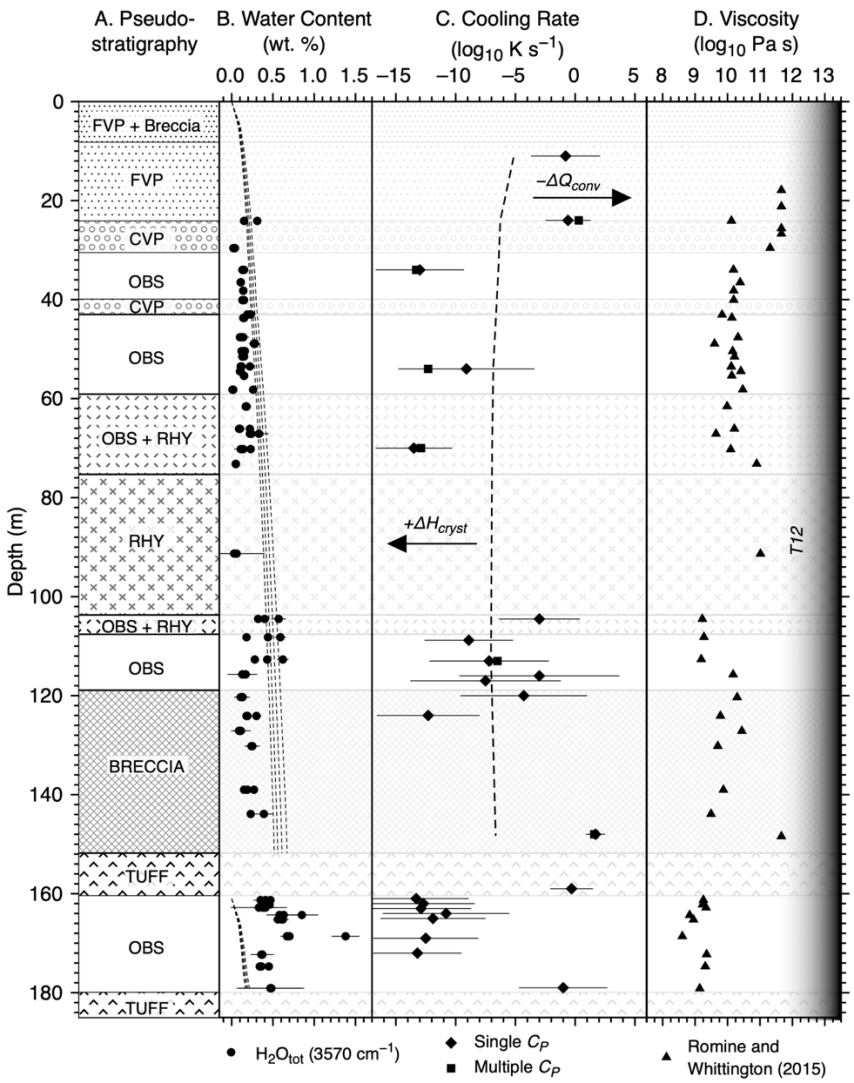

Figure 4.8 Summary figure. (A) Textures after Fink and Manley (1987) observed in the VC-1 drill core. (B) H_2O_{tot} (3570 cm^{-1}) concentrations as a function of depth with predicted solubility from Liu et al (2005; dashed black lines) assuming lithostatic pressure and temperatures between 700 and 1000°C. (C) Natural cooling rates (±2σ) as a function of depth determined using single and multiple C_P measurements with the TN-geospeedometer. Black dashed line represents estimated cooling rates at T12 temperature estimated using the viscosity model of Romine and Whittington (2015) with measured water contents and lithostatic pressure from a one-dimensional finite difference model assuming instantaneous emplacement of a 150-m thick obsidian lava erupted at 834°C that's allowed to cool via conduction with temperature-dependent thermal transport properties (C_P; D). (D) Viscosity values estimated using experimentally determined H_2O_{tot} using the viscosity model of Romine and Whittington (2015) assuming lithostatic pressure and an eruption temperature of 834°C. The shaded region represents *T12* region, or the viscometric glass transition (T_g).

discrepancy is likely because the Battleship Rock Tuff is approximately one-tenth the thickness of the ignimbrite at Grey's Landing.

The natural cooling rates determined for the VC-1 Rhyolite were each determined using a single C_P measurement. Cooling rates for the top and middle of the unit are very consistent at < 1 K a^{-1}. The bottom of the VC-1 Rhyolite cooled as fast as ~0.1 K s^{-1}. The wide range and vertical asymmetry of cooling rates in the VC-1 Rhyolite is unexpected, and further complicates the interpretation of its emplacement history.

The viscosity of Banco Bonito as a function of depth was calculated from the model of Romine and Whittington (2015), using an eruption temperature of 834°C, and measured water concentrations. This was estimated using glass compositions from Ren and Parker (2020), and the glass-pyroxene geothermometer for low-Al rhyolites from Brugman and Till (2019). The viscometric T_g is often defined as the temperature where the viscosity of the melt is equal to 10^{12} Pa s and is referred to as T_{12}. Figure 4.8D shows calculated viscosity as a function of depth. The interior of the flow is relatively constant (~10^{10} Pa s), with higher viscosities at the top and bottom of the flow. The lowest calculated viscosities are ~10^9 Pas, in the lower dense obsidian layer, where water contents are highest. The rate at which the lava cools from its eruption temperature to T_{12} determines how long the lava could remain mobile, and in turn constrains the emplacement behaviors of the lava, such as whether the lava could have advanced as an exogenous "tank-tread" fashion or endogenous "inflation" mode.

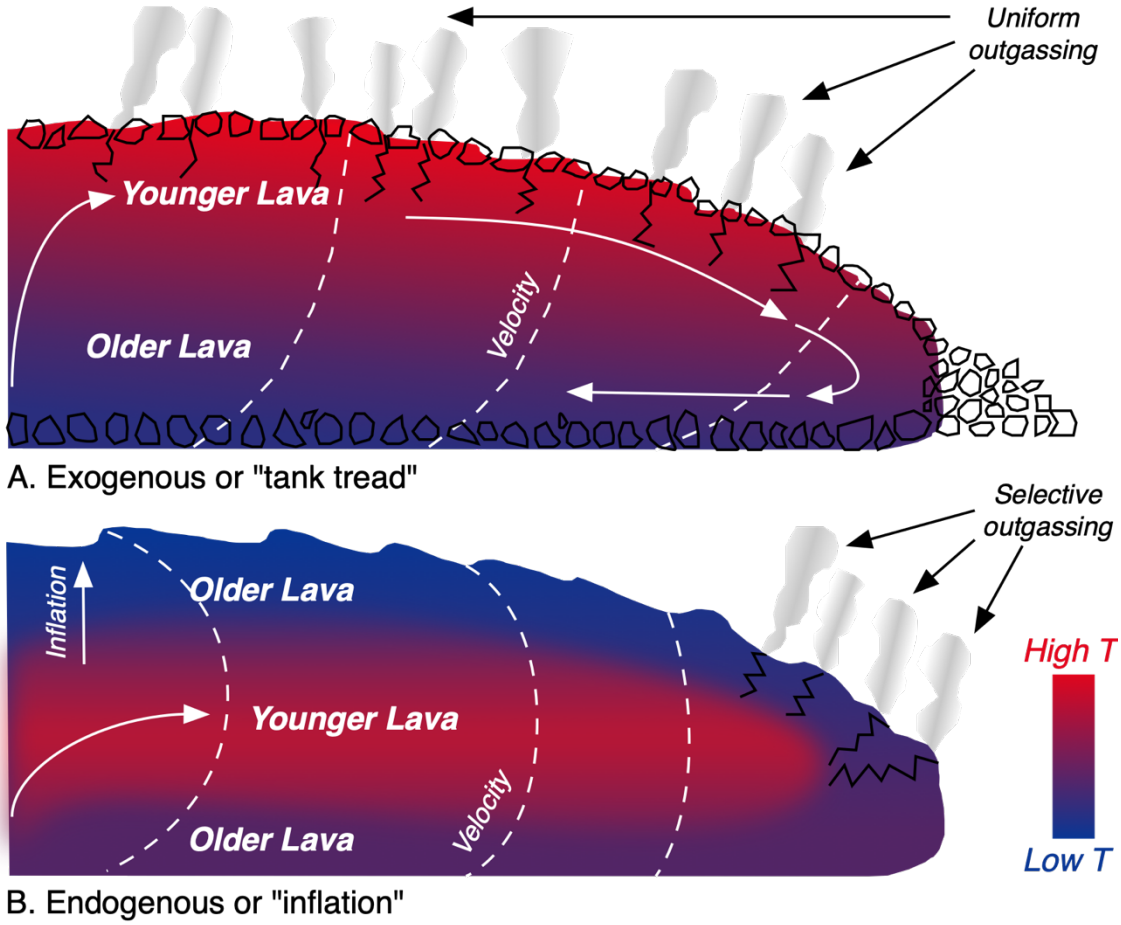

Figure 4.9. Exogenous vs endogenous emplacement styles. (A) Exogenous or "tank-tread" describes emplacement behavior where younger lava is continually emplaced on top of older lava, allowing more uniform outgassing of the lava, and where old lava cascades over the flow front, eventually being overridden and forming a basal breccia. (B) Endogenous or "inflation" behavior is characterized by the forceful intrusion of younger lava into a cold outer carapace, insulating and preserving higher water concentrations through the flow interior.

4.6 Discussion

4.6.1 Endogenous vs exogenous emplacement of Banco Bonito

Evidence from the VC-1 drill core suggests exogenous or "tank tread" style as the dominant mode of emplacement for Banco Bonito. Endogenous emplacement would be

characterized by a discontinuity in water concentrations as a function of depth as younger more volatile rich lava intrudes into an older lava with a protective carapace (Fig. 4.9B).

The water concentrations in Banco Bonito are consistently below predicted solubility limits as a function of depth and temperature, which suggests that the entire thickness of lava equilibrated to pressures lower than present lithostatic conditions. Exogenous or "tank tread" style emplacement is consistent with the observation of water concentrations below predicted solubility limits because exogenous emplacement continually exposes younger lava to low pressures and relatively high temperatures, driving dehydration (Fig. 4.9A).

Two alternate explanations for the observed water contents in the VC-1 drill core of Banco Bonito are that 1) the lava was thoroughly outgassed prior to emergence from the conduit, or 2) the lava actively outgassed while advancing from the vent. The formation of relatively dry (< 1 wt. % H_2O), effusive silicic lavas has been explained by three main models over the last 40 years. The first called the "permeable foam" model described a magma that vesiculated during eruption, but never met the fragmentation threshold. Instead, the magma that emerged from the conduit collapsed onto itself, forming a variably pumiceous and hydrated obsidian lava on the surface (Eichelberger et al., 1986). The second model invoked fractures of variable sizes that act as pathways for volatiles to escape (Gonnermann and Manga, 2003). The third and most recent model calls for *in situ* sintering of ash generated via fragmentation in the conduit (Wadsworth et al., 2020). The welded ash then emerges from the conduit and remains above T_g and can flow away from the vent. The third model efficiently dehydrates the magma prior to

effusion and would likely prevent elevated water concentrations from existing long enough to be injected into younger lava at the surface.

The second possible explanation for the observed water content profile in the VC-1 drill core from Banco Bonito is active outgassing of the lava flow after eruption, during emplacement. Evidence from Banco Bonito and other well preserved obsidian lava flows suggest that water loss continues during lava flow emplacement. Explosion pits that are preserved on the surface of Banco Bonito (Fig. 4.2C) are evidence of volatile overpressure existing up to 6 km from the vent. Tuffisite dikes and veins in the VC-1

Figure 4.10 Photograph of tuffisite vein from VC-1 drill core at 490 ft (149 m) depth. Small tuffisite vein, outlined in black, cross-cutting basal breccia flow texture from Banco Bonito. Scale bar is 4 cm.

drill core (Fig. 4.10) that cross-cut primary textures confirms that outgassing continues during and after emplacement.

The second line of evidence suggesting that Banco Bonito advanced primarily by exogenous or "tank tread" style is the natural cooling rate profile. We hypothesized that exogenous emplacement would be characterized by a relatively symmetric cooling rate profile with the fastest cooling at the top and the bottom, and cooling controlled by conduction and the release of latent heat of crystallization in the center of the flow (Fig. 4.9A). Endogenous emplacement, however, would have slightly asymmetric profile with the fastest cooling at the surface enhanced by radiative and convective cooling, and the base would cool primarily through conduction to the country rock. The center of the flow would experience additional insulation leading to slower cooling than can be explained by conduction alone. We would again expect a discontinuity in the center of the flow in the cooling rate profile where younger lava intrudes the older lava (Fig. 4.9B).

Natural cooling rates determined for Banco Bonito show a pattern consistent with the exogenous emplacement model. The profile is relatively symmetric, with the fastest cooling at the top and bottom of the flow, likely enhanced by convection and radiation as younger lava is emplaced on top of older lava. The cooling rates through the center of the lava are largely consistent with a 1D conductive cooling model of a single flow unit. A few cooling rates are slower than predicted by the 1D conductive cooling model, however these samples likely cooled more slowly due to release of latent heat of crystallization in the center of the flow during or shortly after emplacement.

Lastly, predicted viscosity values using measured volatile contents and the model of Romine and Whittington (2015) approach 10^{12} Pa s near the surface and base of the

flow immediately following eruption. The viscosity contrast between the center of the flow, and the base and surface would promote a tank-tread style emplacement, as well as extensive brecciation observed in the base of the flow (Fig. 4.9A).

One caveat of these interpretations is that they are based on observations made using a single drill core near the flow margin. It is possible that local conditions and distance from the vent may have precluded the possibility of endogenous behaviors observed at Cordón Caulle.

4.6.2 Alternate mechanisms for endogenous style emplacement behaviors

This study suggests that emplacement behaviors of the lava observed during the 2011-2012 eruption of Cordón Caulle are either unique to that eruption, or that a mechanism different from intrusion of younger lava is responsible for the emplacement behaviors observed. We believe evidence of heterogenous water concentrations responsible for tuffisite formation and explosion craters could also inflate the lava through bubble nucleation and growth. Vesiculation during or after emplacement could explain observed inflation during the 2011-2012 PCC eruption (Farquharson et al., 2015) and could also trigger advancement via break-out lobe development due to overpressure (Tuffen et al., 2013; Magnall et al., 2017; Magnall et al., 2018).

Ryan et al., (2015) found that glassy rhyolites with as little as 0.11 wt. % H_2O at 0.1 MPa and temperatures ranging from 900°C to 1100°C can vesiculate yielding final bubble volumes that exceed initial glass volumes by a factor of three. While the experimental temperatures used by Ryan et al., (2015) exceeds the likely eruption temperature from Banco Bonito of ~834°C, the temperature of 2011-2012 PCC eruption

is 900°C (Castro et al., 2014; Farquharson et al., 2015; Magnall et al., 2017). Using the composition of Lava B from Castro et al. (2014) and the cpx-liquid geothermometer of Brugman and Till (2019) also yields an eruption temperature of 898°C, well within uncertainty of previously estimated eruption temperatures of 900°C. Assuming a water content of 0.11 wt. %, like those used in Ryan et al. (2015), the lava at Cordón Caulle could inflate by a factor of 1.5, increasing the volume of the lava and driving break-out lobe development. Assuming an initial flow thickness of 30-60 m and inflation of up to 40 meters observed by Farquharson et al., (2015) would suggest volume increase by 66% to 130%. Wadsworth et al., (2020) also determined that sintering of volcanic ash could preserve up to 0.2 wt. % H_2O in effusive products from silicic eruptions capable of triggering secondary vesiculation. Secondary vesiculation can develop up to 76% bubble volume, further supporting vesiculation as the dominant mechanism capable of triggering endogenous behaviors observed during the 2011-2012 eruption of Cordón Caulle.

4.6.3 Origin of the VC-1 Rhyolite

The VC-1 Rhyolite is only observed in the VC-1 drill core, making morphological and contextual determination of the unit's emplacement history challenging. The dominant texture of the VC-1 rhyolite is dense obsidian, and the pseudostratigraphy proposed by Manley and Fink (1987) is not observed and flow banding foliation transitions from sub-vertical near the top of the unit to sub-horizontal near the base of the unit. These observations are consistent with other small extrusive rhyolite obsidians like the ones at Pietre Cotte, Vulcano, Italy.

The preserved H_2O_{tot} values of the VC-1 Rhyolite as a function of depth (Fig. 4.8B), exceed predicted solubility using the model of Liu et al., (2005) assuming pressure increases with depth. One possible explanation for the discrepancy between predicted solubilities and observed water concentrations is that equilibration to surface pressures was minimal, preserving a magmatic water signature. Another possible explanation is that the water contents are secondary in nature, representing post-emplacement rehydration by hydrothermal fluids.

Water species can be used to help distinguish between primary magmatic and secondary hydration. The VC-1 rhyolite species diagram in figure 4.11, shows how OH^- is the dominant species at low water concentrations, and H_2O_{mol} is the increases as water concentrations increase. The relationship between both species is consistent with a primary magmatic water signature.

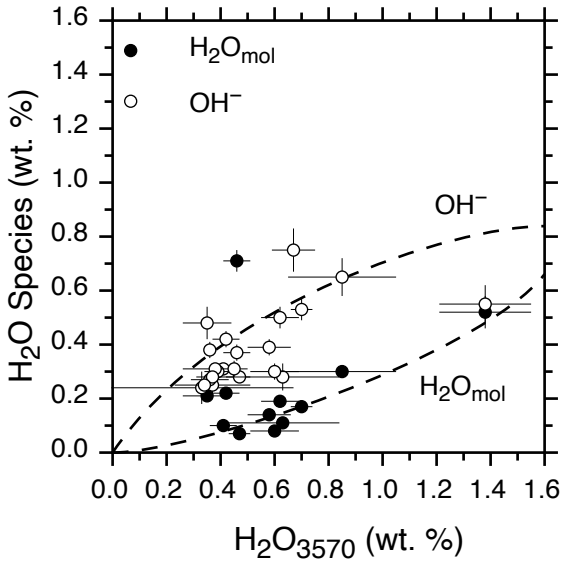

Figure 4.11 Speciation diagram of samples of the VC-1 Rhyolite. Observed concentrations of OH^- and H_2O_{mol} follow trends expected for magmatic speciation.

Spatial distributions of cooling rates can also be used to compare extrusive vs. intrusive emplacement histories. An extrusive emplacement history for the VC-1 Rhyolite would likely have a slightly asymmetric cooling rate pattern as a function of depth, with fastest cooling at the surface aided by radiation and forced convection, and slightly slower cooling at the base of the flow with cooling controlled only by conduction. For an intrusive emplacement, conduction is the primary mode of heat transfer for both the top and the bottom of the intrusion. Large intrusions might see asymmetries due to differences in geothermal gradients of the country rocks into which they intrude, however, the VC-1 Rhyolite is only 20 m thick. The magnitude of upper and lower cooling rates would also be slightly different, with the fastest cooling rate being for the surface of the extrusive emplacement.

Experimental constraints on the thermal history of VC-1 Rhyolite using relaxational geospeedometry suggest an extrusive emplacement history for the VC-1 Rhyolite. Cooling rates determined for the VC-1 Rhyolite are comparable in magnitude to those determined for Banco Bonito. However, no fast cooling is observed near the top of the VC-1 Rhyolite. We attribute this discrepancy to erosion of the surface of the VC-1 Rhyolite, likely by glaciation. Two glacial and interglacial cycles are preserved in the VC-3 drill core through Valles Grande, a Pleistocene lake that formed in Valles caldera when the drainage was dammed by the South Mountain Rhyolite (Fawcett et al., 2006). The glacial cycles have been dated to 552 ka and 380 ka, which is younger than the age of the upper Bandelier Tuff (1.256 ± 0.010 Ma; Phillips et al., 2007) and older than the best age for the Battleship Rock Tuff (74.4 ± 1.3 ka; Zimmerer et al., 2016). Glaciation

could also explain elevated H_2O contents observed in samples from the VC-1 Rhyolite because of secondary rehydration.

4.7 Conclusions

We have constrained the volatile content and thermal history of Banco Bonito, a large obsidian coulée, and the VC-1 Rhyolite, an enigmatic unit that has an unknown emplacement history. Banco Bonito was most likely emplaced as a single flow unit, which advanced primarily in an exogenous or "tank-tread" style, with younger lava being emplaced continuously on top of older lava, which is eventually overridden as the flow advances. The VC-1 Rhyolite was likely an extrusive unit that was eroded by glaciers before being buried by the Battleship Rock Ignimbrite. There is no evidence of endogenous inflation occurring during the emplacement of Banco Bonito, and we suggest the inflation observed during the 2011-2012 eruption of Puyehue-Cordón Caulle was likely driven by vesiculation of minimally hydrated obsidian.

Chapter 5

5. Thermal history and rheological evolution of a rhyolite obsidian lava: Obsidian Dome, Inyo Craters, CA

5.1 Abstract

Obsidian Dome is a well-studied, 600 a rhyolite lava that has been sampled using scientific drilling and is comparable in size to the recently emplaced lava dome at Chaitén volcano during the 2008-2009 eruption in Chile. Chaitén experienced transitions in emplacement behavior and therefore changes in hazards associated with the eruption. Evidence of emplacement behaviors should be preserved at Obsidian Dome, and drill core provides a unique opportunity to sample the entire thickness of an obsidian lava. We collected spatially well constrained samples from two drill cores and outcrop to measure residual water content, thermal history, and apparent viscosity as a function of depth through an obsidian lava and connect interior flow dynamics to the flow margin. Evidence from two drill cores suggests at least two distinct stages of emplacement at Obsidian Dome. Early eruptive behavior was most likely exogenous, transitioning to spine extrusion and endogenous growth. These eruptive behaviors are like the sequence observed during the 2008-2009 eruption of Chaitén. Residual water contents preserved in

the RDO-2B drill core are on average greater than predicted solubility limits, suggesting water loss can continue during emplacement. Dehydration, cooling, and changes in texture modulate the evolution of the rheology of the lava, controlling changes in emplacement behavior.

5.2 Introduction

Well preserved examples of silicic lavas are geographically widespread, however the first detailed observations of active effusive silicic eruptions were made during the 2008-2009 eruption of Chaitén (Lara, 2008; Pallister et al., 2013) and 2011-2012 eruption of Puyehue-Cordón Caulle (Tuffen et al., 2013) in Chile. The 2008-2009 eruption of Chaitén was characterized by faster than expected ascent rates of ~1 ms^{-1} (Castro and Dingwell, 2009) and little precursor activity (Carn et al., 2009), suggesting a highly mobilized rhyolitic magma. The eruption was characterized by five events that include 1) an explosive phase, 2) transitional phase, 3) exogenous lava phase, 4) spine extrusion, and 5) endogenous growth phase (Pallister et al., 2013). The transition of effusive behaviors from exogenous to endogenous styles of the obsidian lava dome resulted in episodes of dome collapse and numerous block and ash flows producing hazardous pyroclastic density currents (PDCs). Therefore, understanding the conditions responsible for the transition between emplacement styles is important for understanding hazards associated with effusive silicic domes.

The prevailing model of silicic lava emplacement has been the permeable foam model first proposed by Taylor et al., (1983) and Eichelberger (1986), which attempts to explain the observation that obsidian lavas are water-poor (~0.1 wt. %), despite the

erupting magma being relatively water rich (1 wt. % to 5 wt. %) at storage conditions. The permeable foam model assumes two distinct eruptive phases. First, an explosive phase, followed by an effusive phase that requires water to exsolve from the magma, forming a magmatic foam, but then for permeability pathways to develop, allowing volatile loss (outgassing) to occur without large-scale fragmentation. Without the water vapor to support the bubble walls, the foam collapses on itself, densifying into the textures observed at the surface.

However, problems exist with the permeable foam model. Friedman (1989) argued that the model does not consider the effects of water loss on the viscosity of magma, and that there is a lack of evidence of welding textures preserved in dense obsidian that bubbles previously existed. More recent studies have proposed that transient fracture networks that form during fragmentation can be an efficient mechanism of water loss without manifesting explosive behavior (Gonnermann and Manga, 2003; Tuffen et al., 2003). Also, observations made during the eruptions of Chaitén (2008-2009; Lara, 2008; Pallister et al., 2013) and Cordón Caulle (2011-2012; Tuffen et al., 2013; Farquharson et al., 2015; Magnall et al., 2018) of silicic lava emplacement directly contradict the permeable foam model.

Instead, hybrid activity where explosive and effusive behaviors occurred simultaneously were observed during the 2008-2009 eruption of Chaitén (Pallister et al., 2013) and 2011-2012 eruption of Cordón Caulle (Schipper et al., 2013). Ash sintering has also become the favored mechanism to explain how a hydrous magma transitions into a dry lava (Gardner et al., 2017; Wadsworth et al., 2020). First the magma fragments during an explosive phase of the eruption, as the explosive eruption wanes, ash begins to

aggrade onto the conduit walls where conditions promote welding fragmented ash together. The welded ash is then erupted as an effusive lava with a fraction of the dissolved water that was within the parental magma. Therefore, new models of silicic lava flow emplacement are warranted.

There are two end-member models that can reconcile observations made during the most recent eruptions of Chaitén and Cordón Caulle. The first is called exogenous emplacement which is characterized by continuous emplacement of younger lava on top of older lava that is then transported to the flow front. The lava surface then cascades over the flow front and is overridden as the lava advances in a "tank-tread" fashion. Similar emplacement behaviors have been observed in analogue models (Fink and Griffiths, 1998; Merle, 1998) and dacitic lavas at Santiaguito, Guatemala in 2000 (Harris et al., 2002), and inferred from strain measurements of an obsidian lava on Lipari (Ventura, 2004). Exogenous behaviors are typically associated with high effusion rates during the eruption.

The second end-member model is called endogenous emplacement which is the result of the development of a cool brittle flow carapace which forms as the lava cools and is often the result of "cooling limited" emplacement (Walker, 1971). Endogenous emplacement is usually characterized by *in situ* inflation of the flow by younger lava (Merle, 1998). Eventually the pressure within the lava overcomes the strength of the stalled flow front, which ruptures allowing the lava to advance primarily through break-out lobes. This behavior is often observed in basaltic pahoehoe lavas (Hon et al., 1994; Self et al., 1998) but was observed for the first time for silicic lavas during the 2011-2012

eruption of Cordón Caulle (Tuffen et al., 2013; Farquharson et al., 2015; Magnall et al., 2017; Magnall et al., 2018).

Emplacement dynamics of silicic lavas are largely controlled by a combination of eruption variables (e.g., effusion rate, underlying topography etc.) and by the thermal and rheological evolution of the lava. The viscosity of lavas is primarily a function of temperature, composition, and texture in the form of crystal and bubble content (Giordano et al., 2008; Mader et al., 2013). For high silica rhyolites like those erupted during the 2008-2009 eruption of Chaitén (SiO_2 > 75 wt. %), H_2O content is the most important variable controlling the magma viscosity after temperature (Romine and Whittington et al., 2015).

Therefore, understanding the thermo-rheological evolution of a suite of spatially well-constrained natural obsidian samples can provide insight into the emplacement dynamics of silicic lavas. Obsidian Dome is the largest (0.17 km^3) and youngest (~600 a) eruptive product in the Inyo Craters, Long Valley, CA (Miller, 1985), and is exceptionally well-studied. From 1983 to 1985, Obsidian Dome was explored as part of the Continental Scientific Drilling Program (CSDP; Eichelberger et al., 1984). The first drill core was named RDO-2A and was collected near the southern flow margin of Obsidian Dome. The second was drilled near the hypothesized location of the vent (RDO-2B). These two drill cores provide a unique opportunity to sample the entire thickness of a well-preserved obsidian lava where the flow front typically obscures the lower portions of the lava, and in two locations. Samples collected from drill core can be used to measure residual water concentrations, natural cooling rates, and viscosities at

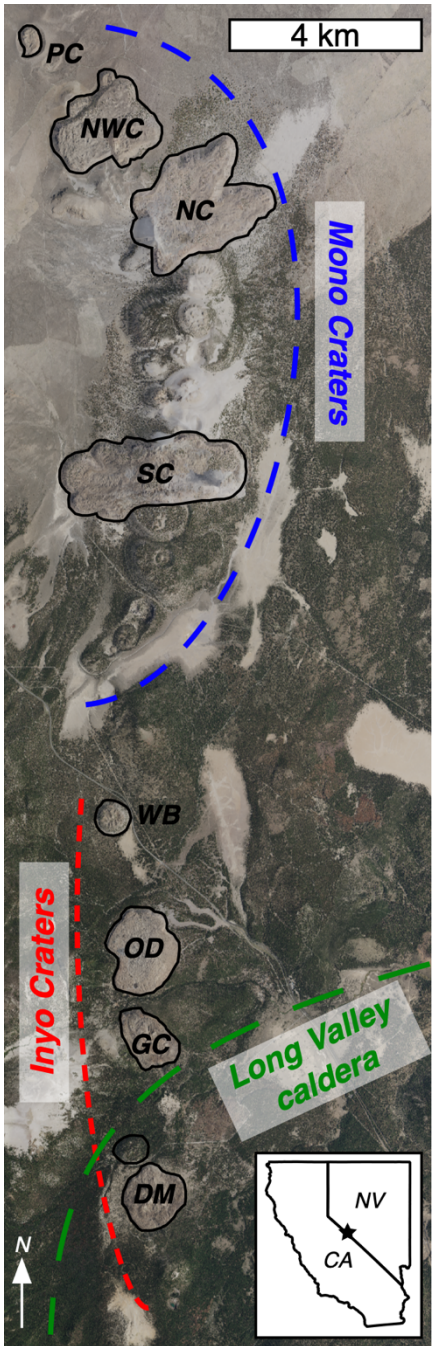

Figure 5.1 Map of Mono-Inyo Craters, Long Valley caldera, CA. Holocene rhyolite lava domes and coulées outlined in black and labelled from north to south: Panum Crater (*PC*), North Coulée (*NC*), Northwest Coulée (*NWC*), South Coulée (*SC*), Wilson's Butte (*WB*), Obsidian Dome (*OD*), Glass Creek (*GC*), Deadman Dome (*DM*). Aerial imagery from NAIP and scale bar is equal to 4 km.

relevant temperatures. These datasets can then be used to assess likely emplacement behaviors as a function of time, temperature, and composition.

We have measured the dissolved water concentrations, natural cooling rates, and apparent viscosities of a suite of samples from outcrop, and drill cores near the vent (RDO-2B) and near the flow margin (RDO-2A). We use these datasets to constrain emplacement dynamics through the thickness of the flow from drill cores and connect interior flow dynamics to behaviors at the flow front with observations from outcrop. We identify volatile loss as an important mechanism for flow front development and therefore transition from largely exogenous emplacement to endogenous emplacement triggering potential hazards such as flow front collapse and block and ash flows.

5.3 Geologic Background

5.3.1 Obsidian Dome, Inyo Craters, Long Valley, CA

The Inyo Craters are a volcanic chain of six magmatic and 15 phreatic volcanic features that extends south from the Mono Craters for 11 km into the Long Valley caldera (Fig. 5.1). Long Valley caldera formed after >600 km^3 of hydrous silicic magma was erupted through ring fractures as the Bishop Tuff around 767 ka (Hildreth and Mahood, 1986; Hildreth and Wilson, 2007; Hildreth and Fierstein, 2017). The magma that supplied the eruptions of the Inyo Craters likely exploited a 16 km long north-south trending fault and fracture zone associated with the Sierra Nevada Mountains that formed during east-west extension of the Basin and Range orogeny. The likely order of eruptive styles includes (1) phreatic explosions above rising dike like body, (2) explosive eruptions, and (3) effusive silicic lavas (Miller, 1986).

Obsidian Dome is the youngest (~600 a), largest (0.17 km^3), and best studied obsidian lava of the Inyo Craters (Miller, 1986; Fig. 5.2). The thickness of Obsidian

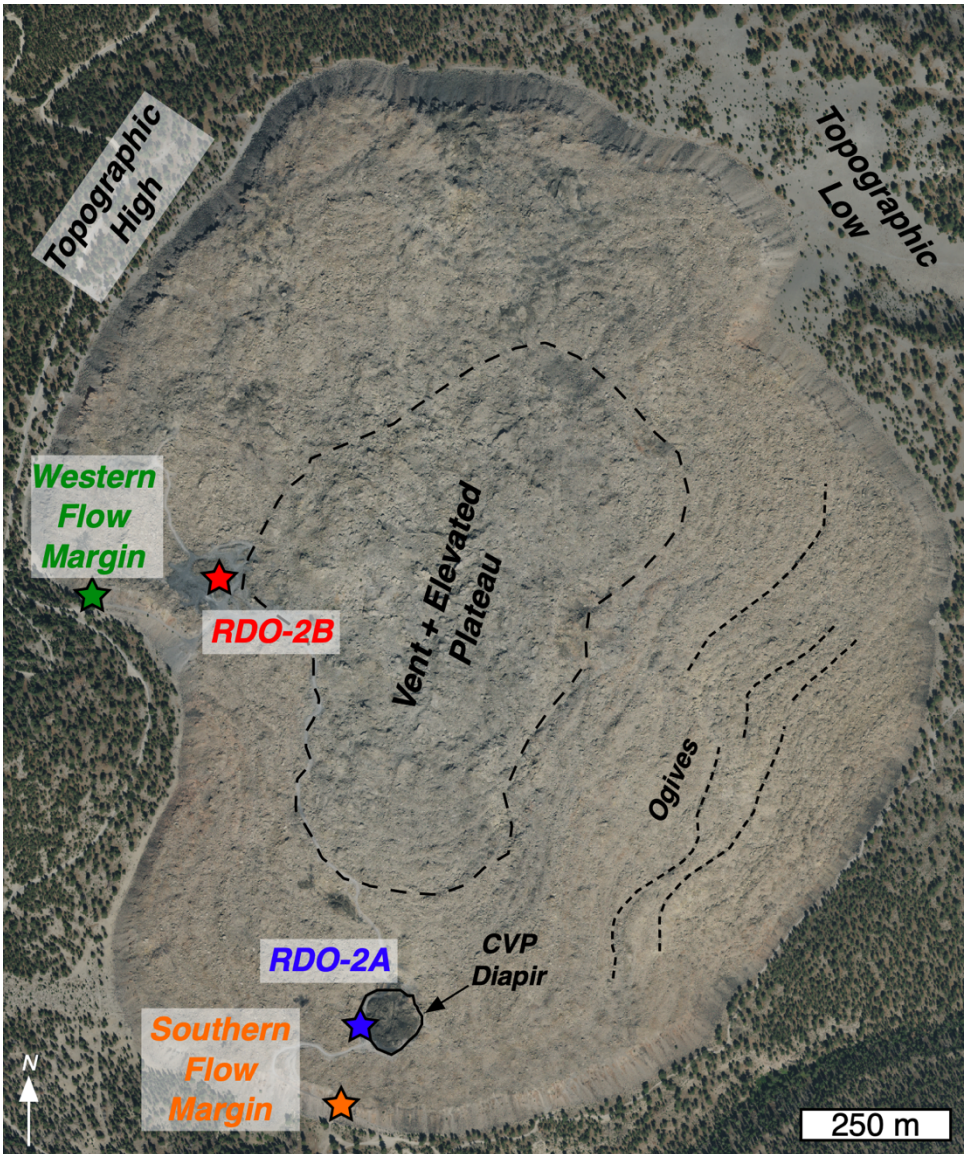

Figure 5.2 Map of Obsidian Dome. Map of general features, sample locations, and drill core sites at Obsidian Dome, Inyo Craters, CA. Stars denote sample locations, including drill core site RDO-2A and RDO-2B. Imagery from NAIP and scale bar = 250 m.

Dome varies from ~30 m near the flow margins to up to 100 m thick near the vent. The lava was emplaced onto nearly flat topography with a uniform slope of ~3°. The northwest margin of Obsidian Dome abuts a hillside, whereas the eastern margin enters a dry stream valley. Ogives or surface ridges exist primarily in the east and southeast portion of the lava (Fig. 5.2). Ogives have often been interpreted as surface folds (Fink,

1980), and used to infer rheological properties of the lava based on Biot's 1961 fold theory (Leggett et al., 2020). However, a recent structural analysis of the surface of Obsidian Dome has concluded that ogives are instead fracture bound ridges that formed primarily by extension of the upper surface because of gravity spreading away from the vent (Andrews et al., 2021).

5.3.2 Scientific Drilling

The Continental Scientific Drilling Program (CSDP) drilled two cores through the entire thickness of Obsidian Dome. In October 1983, a 150-m drill core RDO-2A was completed near the southern flow margin of Obsidian Dome near a feature often referred to as a coarse vesicular pumice or CVP diapir or crease structure (Fig. 5.2). The goal of RDO-2A was to explore the distal portions of Obsidian Dome and to assess the effectiveness of drilling before moving to more complex targets (Eichelberger et al., 1984). The next drill core was collected in 1984 and was drilled at an angle (~55°; Eichelberger et al., 1985) from near the surface expression of the vent to the conduit below and was named RDO-2B. All drill depths in this study are presented in m, and apparent thicknesses have been converted to true thicknesses using the drilling geometry for RDO-2B.

Manley and Fink (1987) observed a standard pseudo-stratigraphy based on textural observations made in drill cores RDO-2A and RDO-2B from Obsidian Dome and the VC-1 drill core from Banco Bonito lava, Valles caldera, New Mexico (Goff et al., 1986). The stratigraphy is characterized by an upper layer of fine vesicular pumice (FVP) that is hypothesized to form as the lava at high temperatures rapidly exsolves dissolved

water as it emerges from the conduit. The next layer is dense obsidian (OBS) followed by coarse vesicular pumice (CVP) that likely forms from bubble coalescence during emplacement (Fink and Manley, 1987). Another layer of dense obsidian followed by crystalline rhyolite (RHY), which likely formed due to slow cooling in the center of the lava. Lastly, another dense obsidian layer is on top of a basal breccia.

The pseudo-stratigraphy is well preserved in drill core RDO-2A, however some deviations from the idealized stratigraphy are observed in drill core RDO-2B. First, there is no observed dense obsidian layer beneath the FVP layer, and the crystalline core is considerably thicker, and only a small dense obsidian layer is preserved between the CVP and RHY layers. The basal breccia features abundant tuffisite dikes and veins, demonstrating continued volatile loss during or shortly after emplacement.

5.4 Materials & Methods

5.4.1 Sample Selection and Preparation

Forty-eight samples from the surface and flow margins of Obsidian Dome were collected during the 2017 field season. Most of the outcrop samples were collected as horizontal and vertical profiles on the western margin of Obsidian Dome, and another set of samples were collected near the large CVP crease structure, across the upper surface and down the southern flow margin (Fig. 5.2). Drill cores RDO-2A and RDO-2B were viewed and sampled at the Energy and Geoscience Institute (EGI), University of Utah, Salt Lake City, UT. Forty-two samples from the entire thickness of the lava were collected from drill core RDO-2A, and 39 samples from the lava were collected from drill core RDO-2B. Photos and detailed observations were made of the core, which has

undergone significant sampling since 1980's. To preserve the core for future study, the total number of samples and amount of material was limited.

Hand samples were first drilled using a water-cooled slow speed drill press with a diamond core bit with ~6 mm interior diameter. Cores ~2.5 cm long were drilled. Two wafers were then cut from the small core sample, both ~2 mm thick. The first wafer was doubly polished for analysis using FTIR and EPMA. The second wafer was ground down to ensure good thermal contact for quantitative C_P measurements. The remaining core was then sectioned into cores ~11 mm long and the ends of the core were made parallel for viscosity measurements.

5.4.2 Sample Characterization

Glass and crystal compositions of select samples were measured using a JEOL JXA-8200 electron microprobe at Washington University in St. Louis, MO. Three repeat measurements were made on glasses with an accelerating voltage of 15 keV, 25 nA current, and a 20 μm beam size. Crystal compositions were measured using the same accelerating voltage and current, but with a 5 μm beam size.

Sample densities were measured using geometric and Archimedean methods. Geometric or bulk densities are measured using a caliper and balance. Repeat measurements of the length and width of sample cores are used to calculate the volume of a cylinder and repeat measurements of the mass of the core can be used to estimate the bulk density of the sample. The bulk density includes dense rock, connected porosity, and isolated porosity.

Archimedean densities measure the density of dense rock including any isolated porosity. Samples are first weighed in air, then submerged in analytical grade ethanol (>99.9% pure) overnight, to ensure all connected pore space is filled. The next day samples are weighed suspended in ethanol. The difference in mass between the two measurements and the known densities of air and ethanol can be used to determine the density of the sample.

5.4.3 Fourier-transform infrared spectroscopy (FTIR)

A Thermo-Scientific Nicolet iN10 FTIR at Baylor University, Waco, TX was used to measure dissolved water concentrations of natural glass samples from Obsidian Dome. We used a spot size of 40 μm by 40 μm and measured wavenumbers from 675 to 7200 cm^{-1}. Zones within the samples with abundant bubbles, crystals, and microlites were avoided to ensure proper measurement of the glass. At least three measurements per sample were made to check for homogeneity of the sample. An optical microscope with a digital micrometer was used to measure apparent thicknesses at each spot analysis by focusing on the top and bottom surface of the doubly polished disc. Apparent thicknesses were then converted to true thicknesses using an empirical index of refraction (~1.5) for rhyolites (Ross and Smith, 1955).

Absorbances were measured at the 5230 cm^{-1}, 4520 cm^{-1}, 3570 cm^{-1}, and 2350 cm^{-1} wavenumbers. We used peak heights and linear baselines for quantifying volatile species concentrations. For peaks measured at the 5230 cm^{-1} and 4520 cm^{-1}, the empirical calibration of Zhang et al., (1997) was used to calculate molecular water

(H_2O_{mol}) and hydroxyl (OH^-) concentrations. The Beer-Lambert equation (Stolper et al., 1982) was used to calculate both total water (H_2O_{tot}) and CO_2 concentrations:

$$C = \frac{MW \cdot A}{\varepsilon \cdot \rho \cdot d} \cdot f \quad 5.1$$

where C is equal to the concentration of the volatile species, MW is the molecular weight of the species of interest, A is the absorbance measured as peak height from a linear baseline, ε is the molar absorptivity coefficient, ρ is density of the sample, d is thickness of the disc at the measured spot, and f is a conversion factor (10^2 for H_2O and 10^6 for CO_2). The ε value is compositionally dependent, and species dependent for H_2O. We used 1214 ± 16 L cm^{-1} mol^{-1} from Behrens et al. (2004) for CO_2 and 73 ± 4 L cm^{-1} for H_2O_{tot} values.

5.4.4 Relaxation Geospeedometry

The thermal history of a glass is preserved in its structure, because unlike crystalline materials, the structure of a glass is temperature dependent. We can therefore use a readily measurable structurally dependent property, like enthalpy (H) or volume (V), to estimate the natural cooling rate of volcanic glasses.

The relaxation time of a structurally dependent property can be estimated using the Maxwell relation (Maxwell, 1867) through the equation:

$$\tau = \frac{\eta}{G_\infty} \quad 5.2$$

where τ is the characteristic relaxation time (s), η is the viscosity (Pa s), and G_∞ is the shear modulus (Pa). Since η is dependent on composition and temperature, so is τ. The

most often used value of G_∞ is 10 GPa (Dingwell and Webb 1990; Webb 1992), however there is some compositional dependence for G_∞ and 30 ± 5 GPa is best for high-silica rhyolites (Whittington et al., 2012).

We can model the relaxation of a structurally dependent property using the concept of the fictive temperature (T_f), which describes the structural contribution to relaxation of a structurally dependent property (Moynihan, 1995). To model the evolution of the T_f as a function of temperature, we must first define the relaxation equation as a function of structure and temperature. An Arrhenius equation is used to model the effects of temperature on the relaxation time (Narayanaswamy 1971; Narayanaswamy 1988):

$$\tau_k = \tau_0 \, exp\left[\frac{\xi \Delta H}{RT} + \frac{(1-\xi)\Delta H}{RT_{f_{k-1}}}\right] \quad 5.3$$

where τ_0 is the limiting relaxation time (s), R is the gas constant (8.314 J K^{-1} mol^{-1}), ΔH is an apparent activation enthalpy of relaxation (J mol^{-1}), ξ is a non-linearity empirical parameter ($0 < \xi < 1$), T is temperature, and T_f is the fictive temperature.

We must also choose an equation to describe the structural contribution to relaxation. The Kohlrausch-William-Watts function (KWW; Kohlrausch, 1854; Williams and Watts; 1969; DeBolt, 1976; Scherer, 1984) describes the non-exponential structural contribution to relaxation and has been shown to adequately fit a wide range of relaxation processes:

$$p = p_0 \, exp\left[-(t/\tau_k)^\beta\right] \quad 5.4$$

where t is time (s), τ is the relaxation time determined from eq. 5.3, β is an order parameter used to constrain the structural contribution to relaxation ($0 < \beta < 1$), and p is a structurally dependent property (e.g H or V).

Debolt et al., (1976) was the first to combine eqs. 5.3 & 5.4 to model the evolution of the T_f as a function of temperature for the purpose of studying annealing, and Wilding et al., (1995) first introduced the equation to the geoscience community as a geospeedometer, where it has since become known as the Tool-Narayanaswamy (TN) geospeedometer:

$$T_{f_m} = T_0 + \sum_{j=1}^{m} \left(T_{f_{j-1}} - T_j\right) \left[1 - e^{-\left(\sum_{k=j}^{m} \frac{\Delta T_k}{|q_k|\tau_k}\right)^{\beta}}\right] \quad 5.5$$

where T_{fm} represents the T_f after m temperature steps ΔT_k from a starting temperature of T_0, cooling rate (q_c; K s^{-1}), relaxation time at step k from eq. 3 (τ_k; s), and β parameter are defined.

The model functions first by simulating cooling from a temperature high enough for the T_f to be in equilibrium with the T (T_0 = 1500 K for this study), where the model cools at a defined q_c by a temperature step (ΔT = 1 K for this study), to a temperature below T_g where the T_f is no longer in equilibrium. Next, the model simulates heating where T_0 is set to the lowest value of T_{fm} from the cooling segment and using a positive q_c value.

Model outputs can be compared directly to experimental C_P measurements through the equation (DeBolt et al., 1976):

$$\frac{dT_f}{dT} = \frac{\left(C_P - C_{P_g}\right)|_T}{\left(C_{P_l} - C_{P_g}\right)|_{T_f'}} \quad 5.6$$

where the left side of the equation is equal to the derivative of the model output of eq. 5 as a function of temperature, and C_P is the measured quantitative isobaric heat capacity (J g^{-1} K^{-1}), C_{Pl} is the liquid heat capacity (J g^{-1} K^{-1}) which is assumed to be constant, and C_{Pg} is the glass heat capacity (J g^{-1} K^{-1}) modelled effectively by the three-parameter empirical equation (Maier and Kelley, 1932):

$$C_{P_g}(T) = a + \frac{b}{T} + \frac{c}{T^2} \quad 5.7$$

where a, b, and c are empirical constants and T is temperature (K). The output of the right side of eq. 5.6 is a normalized C_P that is dimensionless, where the $C_{Pg} = 0$ and $C_{Pl} = 1$, which can then be compared to the output of eq. 5.5 directly.

Previous applications of the TN-geospeedometer use repeat C_P measurements with experimentally controlled thermal histories to constrain four model parameters (e.g., τ_0, ΔH, β, and ξ) prior to solving for q_c for the initial C_P measurement through T_g that includes natural cooling rate information. Parameters τ_0 and ΔH are constrained using an Arrhenius relationship (Wilding et al., 1995) using the peak T_g temperature (K) and the experimental quench rate (q_c; K s^{-1}) with the equation:

$$-log_{10}|q_c| = -log_{10}(\tau_0) + \frac{\Delta H}{2.303RT_g} \quad 5.8$$

where R is the ideal gas constant (8.314 J K^{-1} mol^{-1}) and 2.303 is a conversion factor between base 10 and natural logarithms.

Parameters β and ξ are then constrained using C_P measurements with experimentally controlled thermal histories, using optimized values for ΔH and τ_0 from eq. 5.8. A goodness-of-fit measure such as $\chi^2$is used to minimize the difference between normalized C_P data and outputs from eq. 5.5 by varying β and ξ. Lastly, natural cooling rates are identified using optimal values for τ_0, ΔH, β, and ξ, and varying q_c for the original C_P measurement through T_g.

However, using multiple C_P measurements to determine natural cooling rates of volcanic samples has several technical challenges. (1) Quantitative C_P measurements are time consuming, requiring ~ 1 day to complete, and constraining the four model parameters requires a minimum of three measurements, meaning a single natural cooling rate can require between four and six days to complete. (2) Reheating the same glass sample to a temperature ~50°C above T_g increases the likelihood that the sample will undergo irreversible changes, compromising attempts to constrain the model parameters. (3) Correctly identifying a temperature ~50°C above T_g is difficult because T_g is dependent on a sample's composition, previous thermal history, and experimental heating rate.

Kenderes and Whittington (2021) developed an algorithm capable of identifying cooling rates of natural volcanic glasses using a single C_P measurement while also estimating 2σ uncertainties. The algorithm first generates random combinations of five unknown model parameters (q_c, τ_0, ΔH, β, and ξ) with replacement, calculates a model output using eq. 5.5, compares the output of eq. 5.5 to normalized experimental data, and

assesses a goodness-of-fit using the root mean square deviation (RMSD) and determines if the predicted peak is within ± 10 K of the peak T_g of the sample. If the peak is within ± 10 K, that combination of model parameters is stored, until a user defined number of model parameters are identified. The stored model parameters are then reduced to those that produce curves with RMSD values less than twice the lowest RMSD obtained. The resulting distributions can then be used to identify best-fit model parameters and measures of central tendency can be used to estimate uncertainties on each previously unknown parameter.

A Netzsch 404 F1 Pegasus differential scanning calorimeter (DSC) was used for all quantitative C_P measurements. Temperature and sensitivity calibrations were made using heating and cooling rate specific (± 10 K min^{-1}, ± 20 K min^{-1}, ± 30 K min^{-1}, ± 40 K min^{-1}, ± 50 K min^{-1}) melting temperatures and enthalpies of fusion of In, Sn, Zn, Al, and Au metals. Quantitative C_P values for each sample were determined using pure sapphire (Al_2O_3) reference values from Ditmars (1982). As an additional test of instrument calibration, repeat quantitative C_P measurements of a piece of quartz were made under identical conditions as unknown glass samples. Quartz is an ideal reference material to assess the calibration of a DSC because over the experimental temperature range of interest (~500 to 1300 K), quartz exhibits two distinct heat capacities for α- and β-quartz, and the temperature of the sharp α-β transition is well known (Bragg and Gibbs, 1925). Repeat measurements of quartz for the 40 K min^{-1} heating rates showed variation of the α-β transition peak temperature, and therefore measurements made under the 40 K min^{-1} heating rates are omitted from this contribution.

5.4.5 Uniaxial parallel-plate viscometry

Cylindrical cores of natural obsidian samples with diameters between 5 and 11 mm and lengths between 5 and 14 mm, with parallel ends obtained by polishing, were used for viscosity measurements. We used a Theta Industries Rheotronic III 1000C Parallel Plate Viscometer, which can measure viscosities between $10^{8.5}$ to 10^{14} Pa s, at temperatures up to ~1000°C. Sample temperature was monitored using a K-type thermocouple. Masses of 0.5 kg, 1.0 kg and 1.5 kg were used to apply differential stress to cores of different diameters to identify effects of applied stress on the viscosity of samples. Repeat measurements of NIST standard glasses indicate an experimental accuracy and precision of ± 0.06 log units (Whittington et al., 2009). The viscometer measures change in height using a transducer (± 0.1 μm) as a function of time (s). Assuming perfect slip and conservation of volume, the longitudinal strain rate can be used to calculate the viscosity of the sample through the equation (Neuville and Richet, 1991):

$$\eta_{app} = \frac{\sigma}{3(\partial \ln l/\partial t)} \tag{5.9}$$

where σ is the applied uniaxial stress, l is sample length (m), and t is time (s). The factor of 3 converts longitudinal viscosity to bulk shear viscosity in 3 dimensions.

Measurements were made during a series of isothermal holds. The temperatures of isothermal segments were conducted in non-sequential order to monitor for irreversible changes during measurements, and isothermal holds were held long enough so that sample temperatures varied by less than ± 0.1 °C

Table 5.1 . Glass and crystal compositions (wt. %) of Obsidian Dome samples from the RDO-2A drill core and outcrop samples from the western flow margin.

RDO-2A	*Feldspars*				*Amph.*	*Biotite*	*Oxide*	*Glasses*			
Sample	2A-87	2A-159c[a]	2A-159r[b]	2A-159	2A-159	2A-43	2A-159	2A-159	2A-43	2A-87	2A-156
SiO_2	64.47	62.92	60.57	63.19	42.58	35.46	0.13	74.27	75.49	74.60	74.66
TiO_2	0.02	0.05	0.04	1.44	3.57	5.22	10.30	0.15	0.10	0.11	0.11
Al_2O_3	20.33	24.00	25.12	14.96	10.94	13.66	2.06	14.47	14.21	14.24	14.66
FeO	0.19	0.30	0.32	5.09	13.79	25.63	79.55	1.46	1.25	0.61	1.35
MnO	n.d.	n.d.	n.d.	0.08	0.23	0.32	0.90	0.05	0.05	0.02	0.05
MgO	n.d.	0.01	0.01	2.94	12.82	7.26	0.70	0.08	0.05	0.00	0.08
CaO	2.47	5.10	6.35	1.01	10.72	0.03	0.63	0.72	0.67	0.44	0.74
Na_2O	8.36	7.89	7.59	3.21	2.60	0.65	0.07	4.37	4.31	3.95	4.58
K_2O	1.52	1.35	0.99	6.23	0.93	8.96	0.07	5.54	5.52	6.23	5.45
Total	97.36	101.63	101.00	98.15	98.19	97.20	94.42	101.11	101.65	100.19	101.68

Outcrop	*Glasses*												
Sample	OD06	OD08	OD10	OD12	OD13	OD14	OD16	OD19	OD22	OD25	OD24	OD35	OD39
SiO_2	77.06	74.94	76.01	76.89	75.82	75.40	75.91	74.91	76.12	75.88	75.26	75.16	74.98
TiO_2	0.10	0.11	0.10	0.10	0.10	0.10	0.10	0.12	0.10	0.11	0.11	0.09	0.11
Al_2O_3	14.16	13.88	13.82	13.87	13.98	14.05	13.82	13.92	13.92	13.64	13.74	13.57	14.05
FeO	1.17	1.12	1.11	1.35	1.20	1.11	1.31	1.29	1.00	1.13	1.19	1.10	1.09
MnO	0.04	0.04	0.05	0.04	0.04	0.04	0.06	0.04	0.04	0.05	0.05	0.04	0.04
MgO	0.06	0.04	0.03	0.05	0.05	0.04	0.09	0.06	0.03	0.05	0.03	0.02	0.03
CaO	0.61	0.58	0.55	0.63	0.68	0.61	0.74	0.67	0.55	0.58	0.61	0.54	0.58
Na_2O	4.32	4.15	4.11	4.13	4.22	4.26	4.08	4.18	4.07	3.92	4.00	4.00	4.20
K_2O	5.46	5.48	5.50	5.44	5.48	5.47	5.41	5.43	5.70	5.60	5.54	5.51	5.52
Total	102.97	100.34	101.28	102.48	101.57	101.08	101.52	100.61	101.53	100.97	100.54	100.04	100.60

All compositions presented in weight percent (wt. %); Presented glass compositions are the average of three spot analyses.

[a] Represents analysis of crystal core.

[b] Represents analysis of crystal rim.

Table 5.2 Densities and porosities of outcrop and drill core samples from Obsidian Dome.

Sample Name*	*Density*[a]						*Porosity*					
	ρ_{geo}	±	ρ_{arc}	±	DRE[b]	±	Total	±	Isolated	±	Connected	±
Coarse Vesicular Pumice												
OD42a	809	8	1169	12	2421	12	0.67	0.03	0.36	0.01	0.31	0.03
OD42b	1025	11	1455	16	2421	12	0.58	0.03	0.28	0.01	0.30	0.03
OD42c	758	36	1296	57	2421	12	0.69	0.15	0.27	0.03	0.42	0.16
Fine Vesicular Pumice												
OD44a	1612	6	2309	3	2421	12	0.33	0.01	0.03	0.00	0.30	0.01
OD44b	1581	6	2306	3	2421	12	0.35	0.01	0.03	0.00	0.31	0.01
OD44c	1754	12	1955	1	2421	12	0.28	0.01	0.17	0.00	0.10	0.01
OD44d	1842	8	2257	0	2421	12	0.24	0.01	0.05	0.00	0.18	0.01
OD44e	1628	130	2334	3	2421	12	0.33	0.12	0.02	0.00	0.30	0.12
OD45a	1838	10	2037	1	2421	12	0.24	0.01	0.14	0.00	0.10	0.01
OD45b	1813	4	2078	2	2421	12	0.25	0.01	0.12	0.00	0.13	0.01
OD45c	1769	9	2078	6	2421	12	0.27	0.01	0.12	0.00	0.15	0.01
OD45d	1764	13	2113	1	2421	12	0.27	0.01	0.11	0.00	0.17	0.01
OD45e	1791	29	2191	8	2421	12	0.26	0.02	0.08	0.00	0.18	0.02
OD46a	1692	12	2087	3	2421	12	0.30	0.01	0.11	0.00	0.19	0.01
OD46b	1721	3	2069	2	2421	12	0.29	0.01	0.12	0.00	0.17	0.01
OD46c	1748	8	2163	1	2421	12	0.28	0.01	0.09	0.00	0.19	0.01
OD46d	1741	6	2163	0	2421	12	0.28	0.01	0.09	0.00	0.19	0.01
OD46f	1669	22	2215	1	2421	12	0.31	0.02	0.06	0.00	0.25	0.02
Dense Obsidian												
OD16a	2342	14	2364	1	2421	12	0.03	0.01	0.02	0.00	0.01	0.01
OD16b	2334	31	2368	1	2421	12	0.04	0.01	0.02	0.00	0.01	0.02
OD17a	2351	20	2374	1	2421	12	0.03	0.01	0.02	0.00	0.01	0.01
OD17b	2282	52	2321	1	2421	12	0.06	0.02	0.04	0.00	0.02	0.03
OD17c	2267	9	2305	3	2421	12	0.06	0.01	0.05	0.00	0.02	0.01
OD48b	2356	6	2373	1	2421	12	0.03	0.01	0.02	0.00	0.01	0.01
OD48c	2348	4	2367	0	2421	12	0.03	0.01	0.02	0.00	0.01	0.01
OD48d	2360	6	2376	1	2421	12	0.03	0.01	0.02	0.00	0.01	0.01
OD48e	2351	2	2367	0	2421	12	0.03	0.01	0.02	0.00	0.01	0.01
OD48f	2355	19	2370	0	2421	12	0.03	0.01	0.02	0.00	0.01	0.01
RDO-2A-118	2367	57	2404	1	2421	12	0.02	0.02	0.01	0.00	0.02	0.03
RDO-2A-156	2341	14	2380	1	2421	12	0.03	0.01	0.02	0.00	0.02	0.01
RDO-2A-178	2297	14	2311	1	2421	12	0.05	0.01	0.04	0.00	0.01	0.01
RDO-2A-43	2355	12	2367	2	2421	12	0.03	0.01	0.02	0.01	0.00	0.01
RDO-2A-87	2348	32	2394	1	2421	12	0.03	0.02	0.01	0.00	0.02	0.02
RDO-2B-109	2346	19	2421	12	2421	12	0.03	0.01	0.00	0.01	0.03	0.01

*Letters a-f denote measurements of different cores drilled from the same hand sample; [a]uncertainties are equal to 2σ; [b]DRE is estimated using largest ρ_{arc}.

5.5 Results

5.5.1 Glass and Mineral Compositions

We measured the compositions of 7 crystals from 3 drill core samples, and 51 glass compositions from 4 from drill core samples and 13 outcrop samples (Table 5.1). Glass compositions are homogeneous high-silica rhyolite. Compositions of glasses from the drill core match those sampled from the flow margins within analytical uncertainty. For example, average SiO_2 contents are 75.76 ± 0.95 wt. % for drill core samples and 75.72 ± 1.08 wt. % for outcrop samples. Mineral compositions are consistent with those reported in Vogel et al., (1989).

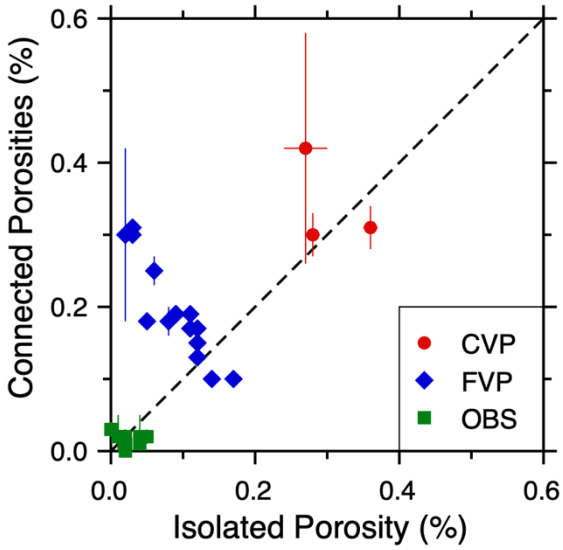

Figure 5.3 Measured connected and isolated porosities for drill core and outcrop samples from Obsidian Dome, including textures from Manley and Fink (1987) such as coarse vesicular pumice (CVP; red circle), fine vesicular pumice (FVP; blue diamond), and dense obsidian (OBS; green square). Error bars represent 2σ uncertainties.

5.5.2 Densities and porosities

Thirty-four geometric (ρ_{geo}) and Archimedean (ρ_{arc}) density measurements were made on 13 samples from drill core and outcrop (Table 5.2). We assumed a dense rock

equivalent (DRE) of 2421 kgm^{-3} which is equal to the largest ρ_{arc}. Samples of coarse vesicular pumice (CVP) have the lowest bulk densities (758 to 1025 kgm^{-3}) and largest connected and isolated porosities (Table 3). Fine vesicular pumice (FVP) samples yielded intermediate densities (1955 to 2334 kgm^{-3}) and porosities, and dense obsidian (OBS) samples had the highest densities (2267 to 2360 kgm^{-3}) and lowest porosities. FVP and CVP samples have greater connected porosities than isolated porosities (Fig. 5.3).

5.5.3 Residual water concentrations

A total of 354 spot analyses were made on 118 samples, including 40 from drill core RDO-2A, 31 from drill core RDO-2B, and 47 from outcrop. A peak was observed at the 3570 cm^{-1} for every sample except for RDO-2A-105, and only three samples had peaks observed at the 5230^{-1} and 4520 cm^{-1} wavenumbers. The average H_2O_{tot} value determined from the 3570 cm^{-1} peak is 0.19 ± 0.09 wt. % for outcrop samples, 0.18 ± 0.09 wt. % for samples from RDO-2A, and 0.31 ± 0.35 wt. % for samples from RDO-2B. A Kruskal-Wallis test comparing the three distributions returns a p value of 1.95×10^{-5}, rejecting the null-hypothesis that the three distributions come from the same distribution at 1% confidence interval (Fig. 5.4A).

5.5.4 Natural cooling rates of obsidian lavas

We measured 30 quantitative cooling rates through T_g at Obsidian Dome (Table 5.3). Twelve cooling rates were identified using samples from drill core RDO-2A, including seven calibrated using multiple C_P measurements, and seven cooling rates were determined using both single and multiple C_P measurements for samples from drill core

RDO-2B. The 11 cooling rates determined for outcrop samples were determined using only a single C_P measurement.

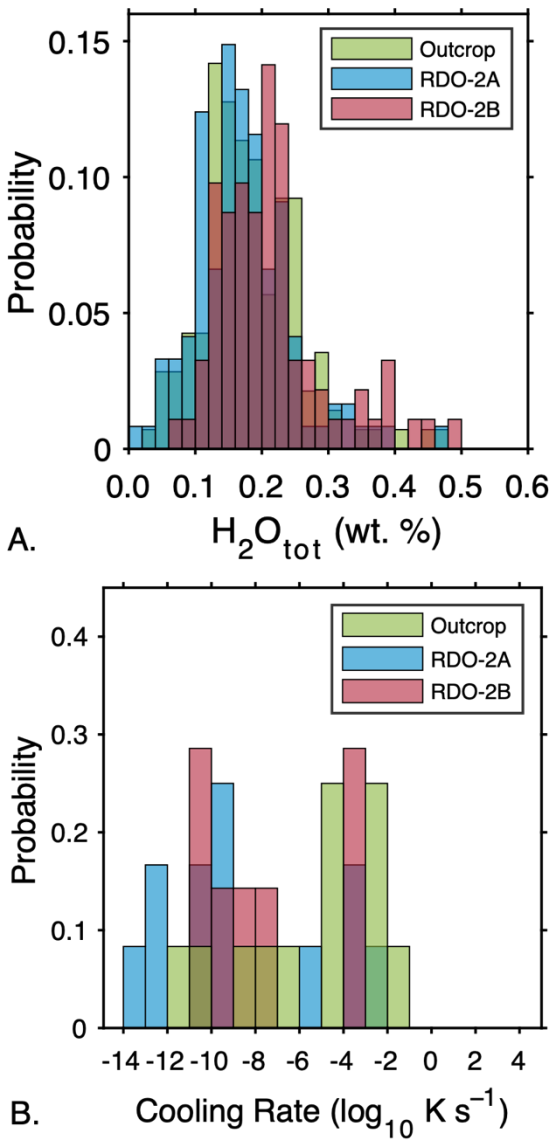

Figure 5.4 Probability density histograms of water contents and cooling rates. (A) H_2O_{tot} values and (B) natural cooling rates for samples collected from drill core RDO-2A, RDO-2B, and outcrop. H_2O_{tot} values are determined using the 3570 cm^{-1} peak for samples from flow margins (n = 141; green) and drill cores RDO-2A (n = 121; blue) and RDO-2B (n = 92; red). Natural cooling rates are determined using a single C_P

Table 5.3 Natural cooling rates determined for samples from Obsidian Dome using single C_P and multiple C_P measurements.

		Single C_P		Multiple C_P	
Sample	Depth (m)	$\log_{10}$ K s^{-1}	±	$\log_{10}$ K s^{-1}	±
Drill Core					
RDO-2A-2.5	0.8	−3.5	3.2	−3.9	3.2
RDO-2A-36.5	11.1	−9.1	5.8	−7.4	3.8
RDO-2A-81	24.7	−12.4	4.2		
RDO-2A-87	26.5	−2.5	4.2	−2.1	2.2
RDO-2A-93	28.4	−9.7	5.2		
RDO-2A-115	35.1	−10.0	5.2	−8.1	2.8
RDO-2A-139	42.4	−10.3	5.7	−11.9	4.2
RDO-2A-145	44.2	−10.5	5.2		
RDO-2A-153	46.6	−5.7	2.5		
RDO-2A-156	47.6	−13.2	3.5	−13.8	2.9
RDO-2A-159	48.5	−12.8	4.0		
RDO-2A-178	54.3	−3.2	5.0	−2.4	2.6
RDO-2B-9	2.3	−3.8	3.7	−2.7	1.8
RDO-2B-41	10.4	−9.0	7.1	−6.0	6.3
RDO-2B-66.5	16.8	−9.3	5.9	−10.4	5.1
RDO-2B-139	35.1	−3.8	3.2	−4.0	2.8
RDO-2B-179	45.3	−7.9	3.3	−8.0	3.1
RDO-2B-200	50.6	−10.7	5.6	−8.4	8.2
RDO-2B-220	55.6	−11.0	5.5	−10.1	5.8
Outcrop					
OD01		−1.4	4.3		
OD02		−3.0	1.7		
OD03		−4.7	3.2		
OD04		−6.4	3.8		
OD05		−2.1	2.8		
OD06		−11.3	5.4		
OD07		−2.9	1.5		
OD08		−4.3	2.7		
OD10		−4.9	2.6		
OD46		−8.6	5.5		
OD48		−7.1	3.6		

An outcrop sample taken from near the summit of Obsidian Dome (OD-01) yielded the fastest measured cooling rate of $10^{-1.4 \pm 4.3}$ K s^{-1} or about 2.6 K min^{-1}. The slowest measured cooling rate comes from sample RDO-2A-156, ~6.7 m above the base of the flow, at $10^{-13.2 \pm 3.5}$ K s^{-1} or about 2 K Ma^{-1}. The top and bottom of RDO-2A cooled at similar rates of $10^{-3.5 \pm 3.2}$ K s^{-1} and $10^{-3.2 \pm 5.0}$ K s^{-1} or ~1 to 2 K h^{-1}. The top of RDO-2B cooled more quickly than the bottom of the flow, making the cooling rate profile as a function of a depth asymmetric in the proximity of the vent. Cooling rate estimates yield a bimodal distribution, with some samples cooling relatively quickly (~10^{-3} K s^{-1} or ~4 K h^{-1}) and the remaining samples cooling very slowly (<1 K per year; Fig. 5.4B).

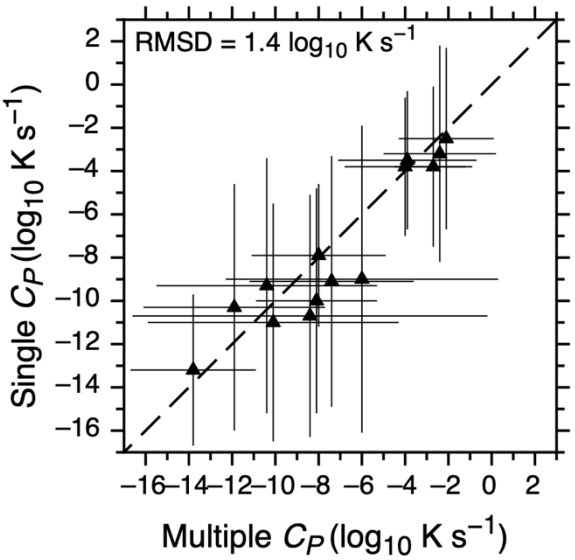

Figure 5.5 Assessment of *CoolMonte*. Fourteen quantitative cooling rates determined using both multiple C_P measurements and single C_P measurements from drill cores RDO-2A and RDO-2B. The global RMSD for all 14 cooling rates is equal to 1.4 $\log_{10}$ K s^{-1}.

Cooling rates determined using a single C_P curve after the method of Kenderes and Whittington (2021) compare well to those determined using multiple C_P

measurements with a global RMSD for 14 samples of ~1.4 $\log_{10}$ K s^{-1} (Fig. 5.5). Uncertainty estimates for both methods also compare well, suggesting the primary source

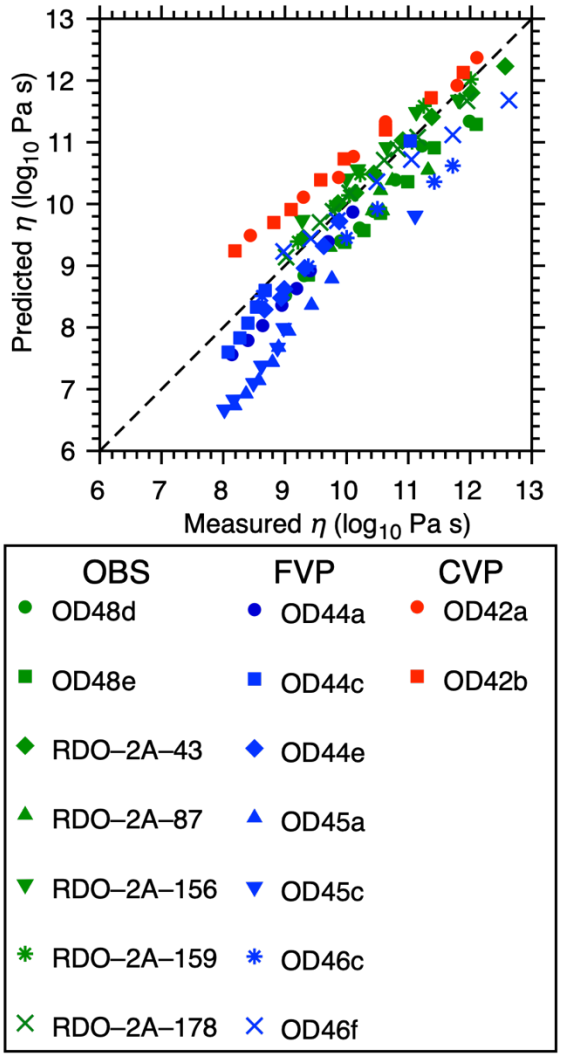

Figure 5.6 Viscosity unity plot comparing measured apparent viscosity values for variably pumiceous obsidians to predicted melt viscosity values using measured H_2O_{tot} values and the model of Romine and Whittington (2015). Dense obsidian (OBS) is reproduced the best, with the viscosity model underestimating the viscosity of FVP, and overestimating the viscosity of CVP at experimental strain rates.

of cooling rate uncertainty is the signal to noise ratio of calorimetric data of natural volcanic glasses.

5.5.5 Apparent viscosities of variably pumiceous rhyolites

We measured the apparent viscosity of seven dense obsidian, seven fine vesicular pumice, and two coarse vesicular pumice samples (Table 5.4). We refer to these as apparent viscosities because FVP and CVP are vesicular, i.e., bubbly suspensions rather than homogeneous liquids. Apparent viscosities of dense obsidian (OBS) ranged from $10^{9.01}$ Pa s at 896.1 °C to $10^{12.57}$ Pa s at 721.6 °C and are reproduced well by the viscosity model of Romine and Whittington (2015; Fig. 5.6) with an RMSD = 0.4 log units consistent with the published uncertainty of the model of 0.43 log units. The apparent viscosities of fine vesicular pumice (FVP) range from $10^{12.63}$ Pa s at 752 °C to $10^{7.66}$ Pa s at 1043.5 °C and are consistently higher than predicted by the viscosity model of Romine and Whittington (2015; Fig. 5.6), with an RMSD of 0.8 log units. Lastly, the measured apparent viscosities of coarse vesicular pumice (CVP) ranged from $10^{12.11}$ Pa s at 719.5 °C to $10^{8.19}$ at 898.5 °C and are consistently lower than predicted by the viscosity model of Romine and Whittington (2015; Fig. 5.6), with an RMSD of 0.7 log units.

The observed differences between predicted and measured viscosity values for samples of FVP and CVP are likely due to the influence of bubbles present in FVP and CVP. Since the bubbles are small in FVP, their effect is more like crystals increasing the apparent viscosity at experimental strain rates. The bubbles in CVP, however, are larger and therefore reduce the apparent viscosity of the sample.

5.5.6 Thermo-rheological evolution of Obsidian Dome

The combination of drill core and outcrop samples from Obsidian Dome enable characterization of the physical properties responsible for flow behaviors as a function of

depth through the entire thickness of the lava, and from the vent to the flow front. Figures 5.7 and 5.8 provide a summary of experimental results as a function of depth through Obsidian Dome near the margin (RDO-2A) and near the vent (RDO-2B).

Drill core RDO-2A is located new the southern flow margin, ~900 m from the primary vent location (Fig. 5.2). Manley and Fink (1987) identified a pseudo-stratigraphy for obsidian lavas, which is well represented in the RDO-2A drill core (Fig. 5.7A). Water concentrations measured using FTIR compare well to those measured using Karl Fischer titration (KFT) from Eichelberger et al. (1986) and are consistently below predicted equilibrium solubility using the solubility model of Liu et al., (2005), where we assumed an emplacement temperature between 700 °C and 900 °C, and estimated pressure using porosity measurements from Eichelberger et al., (1986) with an average DRE of 2421 kg m^{-3} (Fig. 5.7B).

Natural cooling rates are generally faster (~10^{-4} K s^{-1}) at the top and bottom of the flow and slower (~10^{-8} K s^{-1}) in the middle (Fig. 5.7C). There is one exception to the general trend (RDO-2A-87) which is closer in magnitude to rates at the surface and base of the flow. The dashed black line represents predicted cooling rates from a one-dimensional finite difference conductive cooling model of a single 60 m thick flow emplaced on granitic basement at a uniform temperature of 800 °C with temperature dependent thermal properties (Romine et al., 2012). The limiting viscosity at which a lava is unable to continue flowing is often assumed to be 10^{12} Pa s and the temperature at which the lava has a viscosity of 10^{12} Pa s is called *T12.* We estimated the *T12* temperature of the lava as a function of depth using measured H_2O_{tot} values and the viscosity model of Romine and Whittington (2015), since relaxation geospeedometry

Table 5.4 Apparent viscosities of variably pumiceous obsidians.

Dense Obsidian

OD48d		OD48e		RDO-2A-43		RDO-2A-87		RDO-2A-156		RDO-2A-159		RDO-2A-178*	
T (°C)	$\log_{10}\eta$ (Pa s)	T (°C)	$\log_{10}\eta$ (Pa s)	T (°C)	$\log_{10}\eta$ (Pa s)	T (°C)	$\log_{10}\eta$ (Pa s)	T (°C)	$\log_{10}\eta$ (Pa s)	T (°C)	$\log_{10}\eta$ (Pa s)	T (°C)	$\log_{10}\eta$ (Pa s)
720.6	11.99	723.0	12.10	721.6	12.57	800.7	11.32	766.7	11.81	719.2	12.01	720.9	11.95
741.4	11.22	743.5	11.42	742.2	12.02	810.7	10.74	776.8	11.13	740.3	11.25	751.6	11.15
772.5	10.79	774.3	10.99	762.1	11.38	820.5	10.55	808.0	10.65	770.6	11.06	762.0	10.83
802.9	10.44	804.4	10.55	782.5	10.91	840.7	10.42	828.7	10.18	800.8	10.22	771.7	10.61
820.1	10.21	822.2	10.28	813.2	10.44	840.7	10.58	837.5	10.00	820.8	10.04	802.5	10.05
833.7	9.90	834.7	9.97	831.8	10.14	879.5	9.73	879.6	9.28	831.3	9.81	821.1	9.78
872.6	9.31	871.4	9.38	842.3	9.86					869.1	9.21	832.2	9.57
896.1	9.01			879.1	9.30							869.7	9.02

Fine Vesicular Pumice

OD44a		OD44c		OD44e		OD45a		OD45c		OD46c*		OD46f*	
T (°C)	$\log_{10}\eta$ (Pa s)	T (°C)	$\log_{10}\eta$ (Pa s)	T (°C)	$\log_{10}\eta$ (Pa s)	T (°C)	$\log_{10}\eta$ (Pa s)	T (°C)	$\log_{10}\eta$ (Pa s)	T (°C)	$\log_{10}\eta$ (Pa s)	T (°C)	$\log_{10}\eta$ (Pa s)
814.1	10.10	901.2	8.68	823.3	9.88	814.8	9.76	873.9	8.98	762.4	11.72	752.9	12.63
845.1	9.70	921.9	8.54	849.8	9.63	845.6	9.43	900.0	8.88	777.7	11.42	782.3	11.72
877.7	9.41	942.6	8.40	874.8	9.32	878.0	9.06	924.8	8.62	803.9	10.50	804.1	11.05
899.0	9.19	962.7	8.27	899.9	8.99	899.4	8.90	950.4	8.49	833.8	10.00	825.2	10.49
919.8	8.95	982.6	8.08	910.5	8.94	920.0	8.80	975.5	8.17	865.2	9.38	865.1	9.85
946.2	8.64	1002.6	7.91	925.1	8.67	946.3	8.58	991.5	8.02	900.4	8.63	884.6	9.42
966.3	8.40	1022.6	7.73			966.4	8.37					899.1	8.98
986.2	8.14	1043.5	7.66			984.7	8.19						

Coarse Vesicular Pumice

OD42a*		OD42b*	
T (°C)	$\log_{10}\eta$ (Pa s)	T (°C)	$\log_{10}\eta$ (Pa s)
719.5	12.11	751.0	11.37
740.6	11.79	777.6	10.63
771.1	10.63	804.1	9.96
801.5	10.11	823.5	9.58
821.5	9.87	853.4	9.10
841.0	9.30	866.7	8.82
880.8	8.44	898.5	8.19

*Data from Andrews et al., 2020.

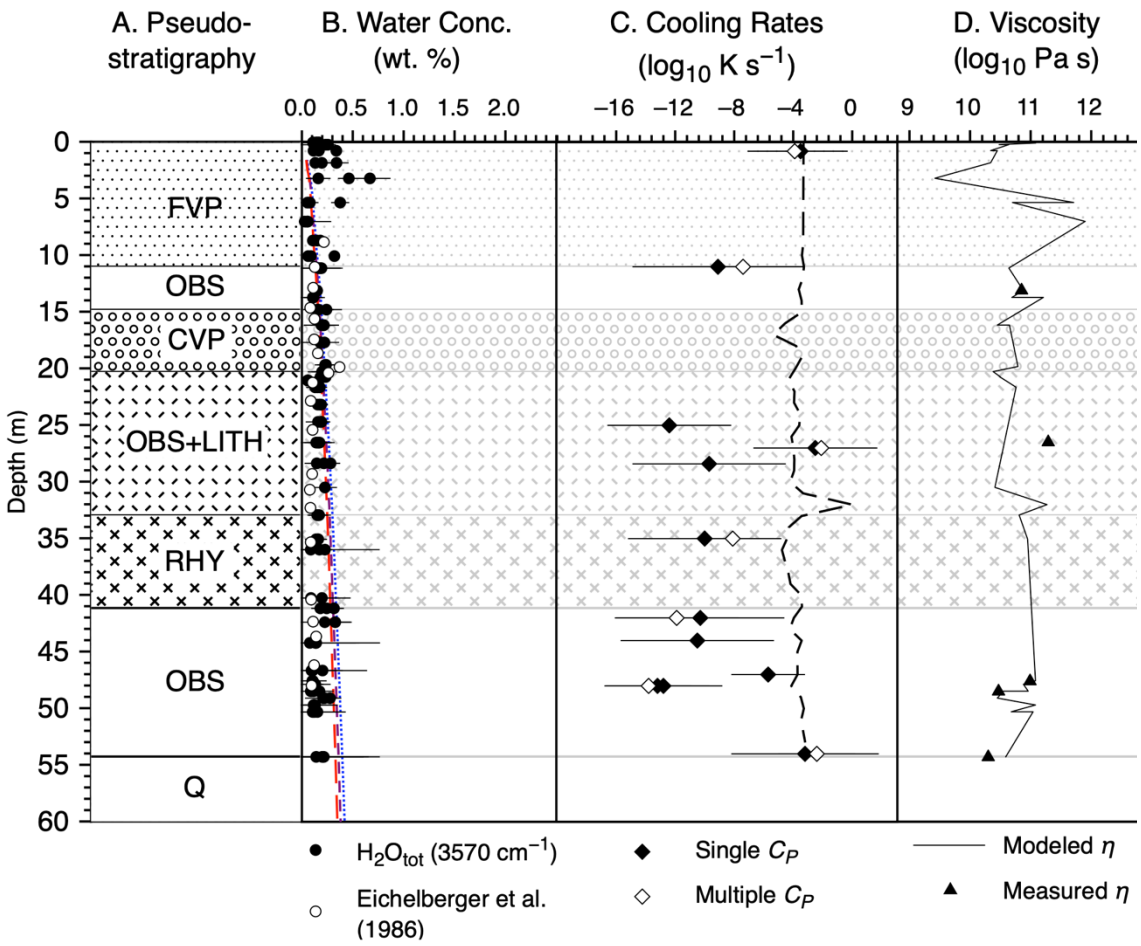

Figure 5.7 Summary figure RDO-2A. Pseudo-stratigraphy, water content, natural cooling rates, and apparent viscosity as a function of depth for drill core RDO-2A near the flow margin at Obsidian Dome. (A) Pseudo-stratigraphy uses the textural terms from Manley and Fink (1987). (B) Water content from FTIR measurements (black circles) with 2σ uncertainties with values from Eichelberger et al., (1986), and predicted solubility at 700°C, 800°C, and 900°C, pressure using the average density of dense obsidian from drill core RDO-2A and porosity values from Eichelberger et al., (1986). (C) Natural cooling rates determined using both single C_P and multiple C_P measurements and modeled cooling rates at *T12* estimated using measured water contents and the model of Romine and Whittington (2015) from a 1D conductive cooling finite difference model with temperature dependent thermal properties. (D) Measured apparent viscosity values from drill core samples, and estimated eruption viscosity using measured water contents, an estimated eruption temperature of 792°C using compositions from Vogel et al., (1989) and the cpx-liq thermometer of Brugman and Till (2019), and the viscosity model of Romine and Whittington (2015). Q = quaternary undifferentiated.

records the cooling rate of volcanic glasses in the T_g region. Predicted cooling rates match experimentally determined cooling rates near the top and bottom of the lava, but do not match the slow cooling measured in the center of the flow, likely due to the release of latent heat (ΔH_{cryst}) while the center of the lava crystallized. Cooling rates determined using a single C_P measurement agree with those determined using multiple C_P measurements, demonstrating the relative precision of using a single C_P measurement to determine natural cooling rates.

Experimental viscosity values at an eruption temperature of 792 °C, estimated using compositions from Vogel et al., (1989) and the liq-cpx thermometer from Brugman and Till (2019), and modeled melt viscosities using the viscosity model of Romine and Whittington (2015) and experimental water contents, are shown as a function of depth in figure 5.7D. The estimated and measured viscosities vary little as a function of depth and experimental viscosity estimates match the model of Romine and Whittington (2015) well, again except for sample RDO-2A-87.

Drill core RDO-2B is located approximately 500 m due west of the summit and primary vent of obsidian dome and was drilled at a dip of 55° and intersected the conduit beneath the vent (Fig. 5.2; Eichelberger et al., 1985). The pseudo-stratigraphy observed in the RDO-2B drill core varies slightly from that observed in RDO-2A, with a thicker crystalline core, fewer dense obsidian layers, and abundant tuffisite dikes present in the basal OBS + BRECCIA unit (Fig. 5.8A). Water concentrations measured using FTIR, again, compare well with those determined using KFT (Eichelberger et al., 1986), but instead of being consistently below solubility limits (Liu et al., 2005), the observed water concentrations occasionally exceed predicted solubility (Fig. 5.8B).

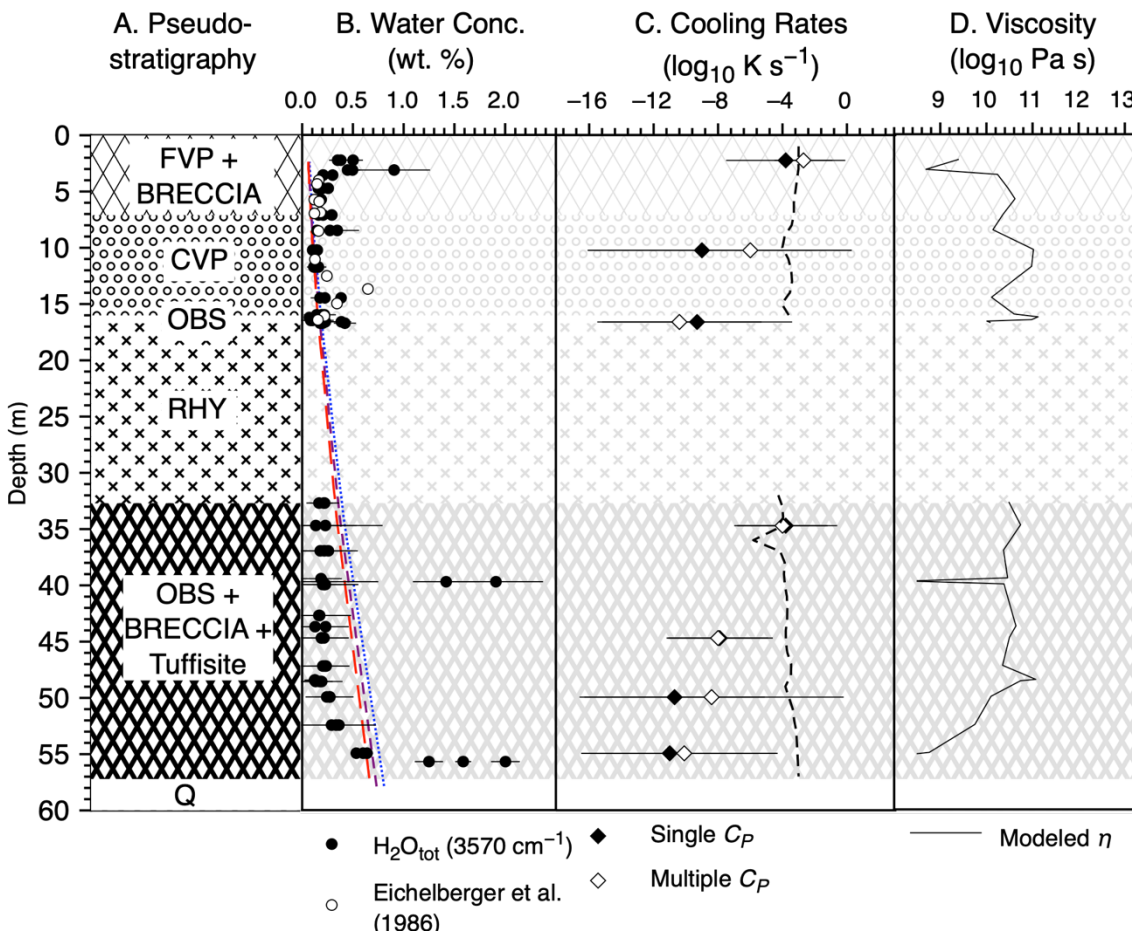

Figure 5.8 Summary figure RD0-2B. Pseudo-stratigraphy, water content, natural cooling rates, and apparent viscosity as a function of depth for drill core RDO-2B near the vent at Obsidian Dome. (A) Pseudo-stratigraphy uses the textural terms from Manley and Fink (1987). (B) Water content from FTIR measurements (black circles) with 2σ uncertainties with values from Eichelberger et al., (1986), and predicted solubility (Liu et al., 2005) at 700°C, 800°C, and 900°C, pressure using the average density of OBS from drill core and porosity values from Eichelberger et al., (1986). (C) Natural cooling rates determined using both single C_P and multiple C_P measurements and modeled cooling rates at *T12* estimated using measured water contents and the model of Romine and Whittington (2015) from a 1D conductive cooling finite difference model with temperature dependent thermal properties. (D) Modeled apparent viscosity (Romine and Whittington, 2015) values at an estimated eruption temperature of 792°C using compositions from Vogel et al., (1989) and the cpx-liq thermometer of Brugman and Till (2019). Q = Quaternary undifferentiated.

The experimentally determined natural cooling rates are less symmetric in drill core RDO-2B, with no observed fast cooling near the base of the flow. Instead, fast cooling is observed at the surface and ~35 m depth (Fig. 5.8C). The rates are comparable to those observed at the top and bottom of drill core RDO-2A, but the rates observed in the center of the flow are slower (~10^{10} K s^{-1}) than those observed in the center of RDO-2A (Fig. 5.4B). Predicted cooling rates again match faster cooling rates well, but overestimate cooling rates in the center of the flow, likely due to ΔH_{cryst} from the crystalline core. Natural cooling rates determined using a single C_P measurement also compare well to those determined with multiple C_P measurements.

No experimental viscosity measurements were completed for samples from drill core RDO-2B, therefore, only melt viscosities estimated using measured H_2O values and the model of Romine and Whittington (2015) are shown. Viscosities are occasionally lower than those estimated for RDO-2A because of the effect of higher concentrations of H_2O in the lava. The steady increase in H_2O near the base of the flow (Fig. 5.8B) can be seen decreasing the viscosity in figure 5.8D.

5.6 Discussion

5.6.1 Emplacement styles at Obsidian Dome

We have shown that differences in textures, H_2O concentrations, and thermal histories record evidence of changes in emplacement styles during the eruption of Obsidian Dome. Exogenous or “tank-tread” emplacement is characterized by volatile contents consistently at or below solubility limits, symmetrical thermal histories, and a smaller crystalline core observed in the RDO-2A drill core, comparable to the early

emplacement dynamics observed at the eruption of Chaitén in 2008-2009 (Pallister et al., 2013). Drill core RDO-2B has water concentrations consistently below or above predicted solubility limits, asymmetrical thermal profiles in cooling rates, and a feedback loop of slower cooling rates in the center promoting crystallization of a thicker rhyolite core buffering cooling through the release of *ΔHcryst*, suggesting late-stage endogenous emplacement.

The transition between these two emplacement styles is thought to be responsible for the generation of block and ash flows, largely from collapse of the flow front exposing a hot interior core that can suffer explosive decompression. The transition was

Figure 5.9 Photograph of extruded spine looking approximately due east from the summit of Obsidian Dome of a spine extruded during emplacement that is approximately 22 m tall and represents the transition between exogenous and endogenous emplacement.

marked by extrusion of a spine during the 2008-2009 eruption of Chaitén (Pallister et al., 2013). A similar spine is preserved near the summit of Obsidian Dome (Fig. 5.9).

5.6.2 Continued volatile loss during emplacement

Preserved water concentrations in samples from drill core RDO-2A and RDO-2B are distinct from one another (Fig. 5.4A) and RDO-2A is like concentrations collected from outcrop. The difference ($p = 1.95 \times 10^{-5}$) between proximal and distal

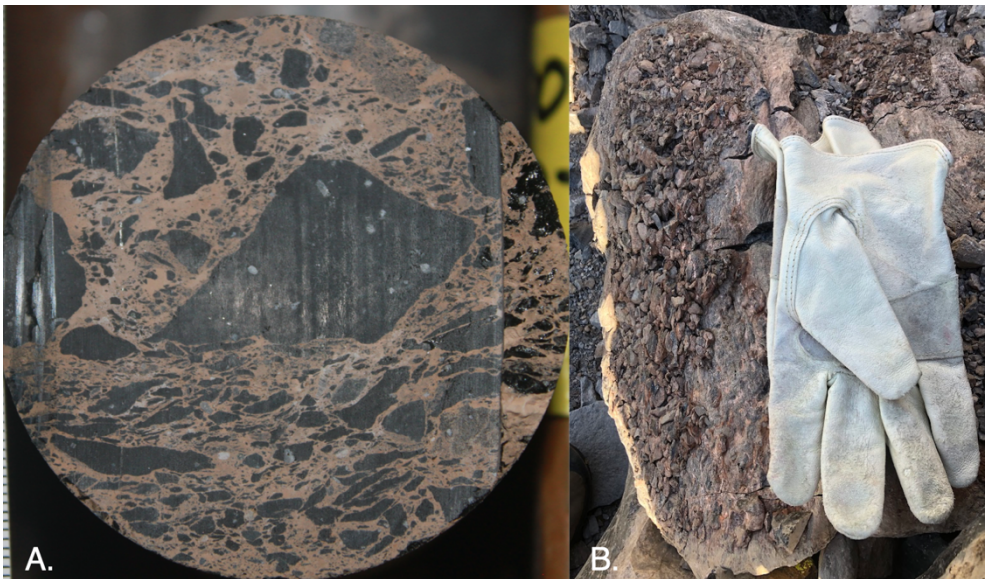

Figure 5.10 Photographs of outgassing textures. (A) Photograph of drill core RDO-2B from 139.6 feet (42.5 m) of a tuffisite vein with angular obsidian clasts within an oxidized ash matrix. Field of view = 5cm. (B) Clasts welded by oxidized ash to the side of an obsidian boulder near the western flow margin of Obsidian Dome.

water concentrations suggest continued volatile loss during lava emplacement at Obsidian Dome. Textural evidence in the form of stretched vesicles in CVP and tuffisite veins also support the idea that silicic lavas continue to lose water during emplacement (Fig. 5.10). Lastly, H_2O_{tot} values from drill core RDO-2A are consistently at or below predicted solubility limits whereas drill core RDO-2B is either below or above predicted solubility providing a driving force for water loss during emplacement (Fig. 5.11). Consequences of

water loss during emplacement can include changes to the physical properties of the lava and therefore emplacement behaviors and can result in explosive decompression if the flow front collapses.

There are primarily two mechanisms capable of removing water from a hydrous rhyolitic lava during emplacement: (1) diffusion of volatile species, and (2) secondary vesiculation. We can estimate diffusion of H_2O in a rhyolite melt with less than 2 wt. % H_2O using the equation from Ni and Zhang (2008):

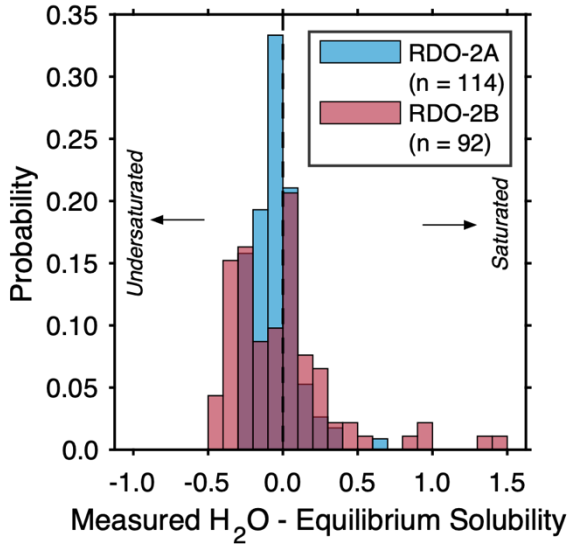

Figure 5.11 Probability density histogram of predicted equilibrium solubility values (Liu et al., 2005) subtracted from H2Otot values measured using FTIR for drill cores RDO-2A (flow margin) and RDO-2B (vent). A value of 0 represents measured volatile contents in equilibrium, values < 0 represent undersaturated samples, and values > 0 represent samples that are super saturated.

$$D_{H2Ot} = \frac{C}{C_0} \exp\left(9.5279 + 1.8875P - \frac{9698.5 + 3625.6P}{T}\right) \quad 5.10$$

where C is the starting concentration of H_2O_{tot} and C_0 is 1 wt. %, P is pressure in GPa, and T is temperature in K. We assume an eruption temperature of 792 °C, pressure of 0.1 MPa, and C is 0.31 wt. % is the average of H_2O_{tot} value from drill core RDO-2B yields

4.74×10^{-13} m^2 s^{-1} for D_{H2Ot}. The time necessary for water to diffuse 1 m under these conditions would be ~ 16 ka.

The time required for water to diffuse through the melt can be significantly reduced by reducing the effective travel distance. Pre-existing fractures can promote water loss by effectively reducing the diffusion distance. For example, water can diffuse across 1 mm in 150 hours or 0.1 mm in 15 hours under the same conditions.

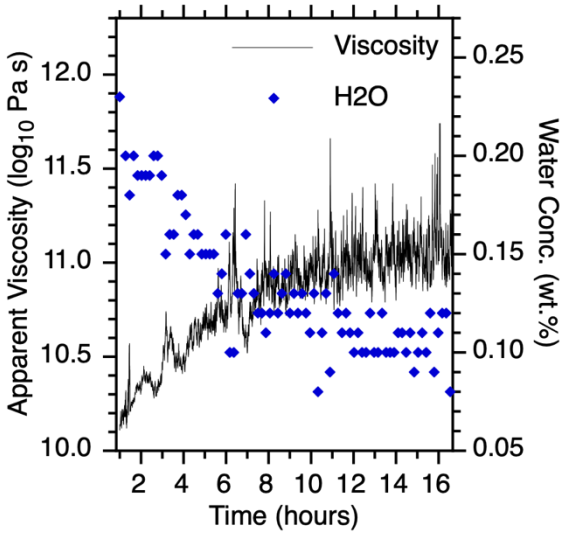

Figure 5.12 Experimental dehydration of sample OD-017a from 0.27 wt. % H_2O_{tot} to ~0.1 wt. %. Sample was held at 800 °C for ~16 hours, black line represents measured change in viscosity as a function of time, and blue diamonds represent estimated water contents using the viscosity model of Romine and Whittington (2015).

We tested this mechanism of water loss by experimentally dehydrating sample OD17a, which had 0 ± 2 % total porosity and 0.27 wt. % H_2O_{tot}, by heating it to and holding it at 800 °C for ~16 hours. We calculated the apparent viscosity of the sample as a function of time, and then inverted the viscosity model of Romine and Whittington (2015) to estimate the water concentration based on the observed change in viscosity (Fig. 5.12). The final water content was estimated to be ~0.1 wt. %, consistent with the

predicted solubility at 800 °C and 0.1 MPa (Liu et al., 2005). An apparent loss of ~ 0.17 wt. % after 16 hours was much faster than predicted by diffusion alone (up to 6800 hours) and corresponds to a diffusion distance of ~300 μm. Additional evidence that fractures accelerated water loss was the visible oxidation of pre-existing fractures in the sample (Fig. 5.13).

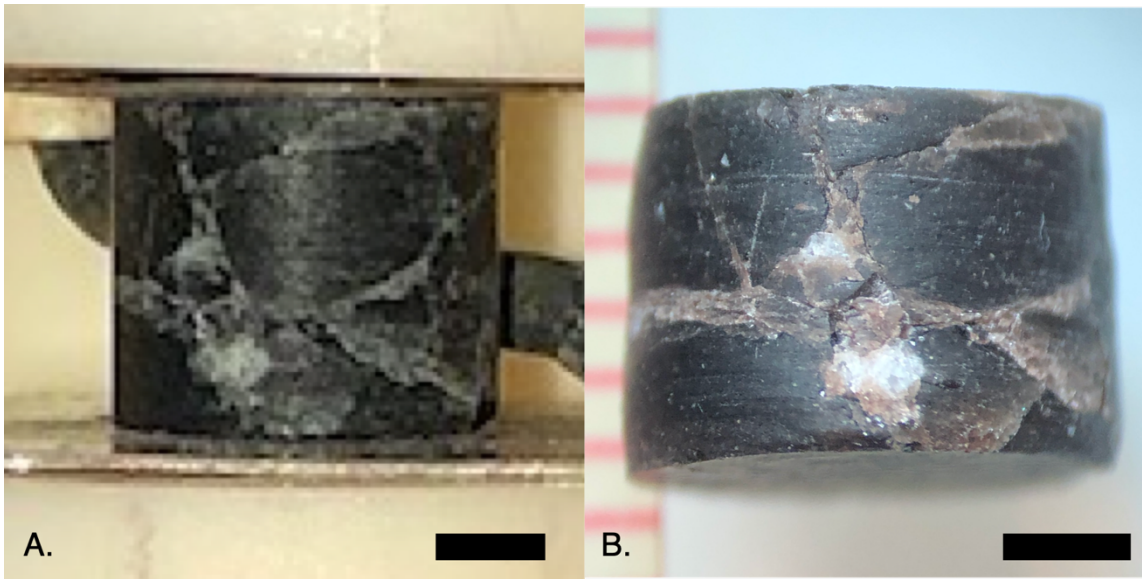

Figure 5.13 Pre- and post-experiment photographs of sample OD-017a. Scale bar = 2 mm.

The last mechanism of water loss is vesiculation. Bubble nucleation and growth is one of the primary mechanisms for triggering fragmentation during explosive volcanic eruptions. However, secondary vesiculation of a largely degassed rhyolite lava has until recently been difficult to explain. Mangan and Sisson (2000) found that an overpressure of >100 MPa was required to trigger homogenous nucleation in rhyolite, which is much greater than conditions during emplacement of marginally degassed obsidian lavas. Wadsworth et al. (2020) argue that a hydrated silicic magma can be efficiently degassed in the conduit, and dry ash particles can then weld or sinter together forming a silicic lava

with up to 0.2 wt. % H_2O. Ryan et al. (2015) showed that even relatively dry obsidian (0.11 wt. %) can vesiculate if held at temperatures ≥900 °C for as little as 20 hours. Even though the eruption temperature at Obsidian Dome is estimated to be only ~792 °C, the average H_2O_{tot} value for samples from drill core RDO-2B is 0.31 wt. %, which is oversaturated at emplacement conditions and capable of driving secondary vesiculation in zones where temperatures are high enough and pre-existing fractures are minimal. After secondary vesiculation water likely escapes through the formation of microcracks evidenced by a higher percentage of connected pore space compared to isolated pore space in CVP and FVP samples (Fig. 5.3).

5.6.3 Emplacement timescale

Changes in volatile content during emplacement can affect the intrinsic melt viscosity (Stevenson et al., 1998; Romine and Whittington, 2015), and the bulk effective viscosity of the material by adding bubbles (e.g., FVP, CVP; Fig. 5.6; Mader et al., 2013). As lava flows across the surface, it is also losing heat continually to the surroundings, increasing its viscosity. Understanding the change in rheology as a function of time is key to understanding the transition between emplacement behaviors, and therefore the hazards associated with them.

We can use *T12*, the estimated eruption temperature, and estimates of natural cooling rates to estimate how long the lava is capable of flowing. Predicted *T12* values vary by ~100 °C controlled primarily by differences in water content. The difference between *T12* and the estimated eruption temperature of 792 °C is between ~40 °C and ~150 °C. There are slow (~10^8 K s^{-1}), and fast (~10^4 K s^{-1}) cooling rates observed in drill

cores RDO-2A and RDO-2B. If we assume the lava cools linearly, a conservative estimate for the time it takes the lava to reach *T12* is as soon as 4 to 17 days and as long as 130 to 480 years. Cooling at the surface is likely non-linear due to radiative heat loss, and therefore the surface of the lava would have cooled more quickly than our estimates. Andrews et al., (2021) estimated that the surface of Obsidian Dome could have cooled in as little as 100 minutes. Leggett et al., (2020) estimated an emplacement time scale of 30 days for Obsidian Dome using flow morphology and block size distributions. Their estimate, however, relies mostly on morphological features that are consistent with exogenous emplacement, suggesting that 30 days might have only captured the first phase of emplacement. Pallister et al., (2013) reports that the exogenous phase during the eruption of Chaitén lasted ~3 months.

5.7 Conclusions

We have shown that Obsidian Dome likely experienced at least two distinct flow styles during emplacement. The initial behavior at Obsidian Dome was exogenous as evidenced by uniformly low H_2O_{tot} values, a symmetrical cooling rate pattern, and generally faster cooling rates. The eruption likely transitioned to emplacement of a spine near the vent, before continuing with endogenous behavior, which can be inferred based on disequilibrium H_2O_{tot} values, slower cooling rates, and asymmetries in the cooling rate profile. Preserved water concentrations in the RDO-2B drill core suggest that water loss continues during emplacement and can play a significant role in modulating the rheology of the flow and therefore emplacement style and hazards.

Chapter 6

6. Conclusion

This work centered on applying relaxational geospeedometry to estimate the thermal histories of obsidian lava flows on a much larger scale than any previous study. Drill cores from Obsidian Dome and Banco Bonito allowed us to constrain natural cooling information for obsidian lavas as thick as 150 m and across a wide range of textures observed at these lavas. However, relaxational geospeedometry is a time-consuming method requiring up to five days to determine a single natural cooling rate. If I had collected all the data necessary to estimate cooling rates for every sample I collected (n = 310), including samples from lavas not included in this work, I would have spent 1550 days or ~4.25 years in the laboratory. If *CoolMonte* had existed at the start of my Ph.D., I could have completed all the required laboratory work in < 1 year.

The societal relevance of this work falls primarily into two categories. First it provides information relevant to volcanological hazards in Long Valley and Valles calderas. Second, it includes technical advances that can affect the broader geological, material, and food sciences.

Eruptions of rhyolitic magmas are some of the largest and most explosive on Earth. However, these “super eruptions” capable of producing hundreds of cubic kilometers of volcanic ash, are relatively rare events happening on the 0.1 to 1 Ma

recurrence intervals. The 767 ka eruption of the Bishop Tuff from Long Valley caldera, and 1.256 Ma eruption of the Bandelier tuff from Valles caldera are two examples of relevant eruptions.

Effusive eruptions of rhyolitic magma have much shorter recurrence intervals from ~10 ka to 10 a. Examples include the eruption of Banco Bonito ~68.3 ka to the most recent eruption at Cordón Caulle, ~50 years after its last eruption. Effusive lavas are classified as local hazards, and rarely threaten population centers. However, the ongoing eruption of Krýsuvík-Trölladyngja, popularly referred to as the Fagradalsfjall eruption in Iceland, has demonstrated that an accessible effusive silicic eruption could be potentially hazardous. Unlike the relatively quiescent eruption in Iceland, an effusive silicic eruption can be accompanied by periods of flow front collapse and block and ash flows, which are hazardous to tourists and onlookers. Coupled with the fact that the USGS has rated the Mono-Inyo chain as one of seven volcanic centers as high to very high risk further emphasizes the importance of this work.

The second societal importance of this work includes technical advances. The theory behind the Tool-Narayanaswamy geospeedometer was originally developed for the purpose of studying the effects of annealing in the commercial glass industry. Therefore, it is within the realm of possibilities that *CoolMonte* could be used in the future by glass scientists interested in evaluating one of the five unknown model parameters for developing increasingly advanced glass materials. Additionally, the furthering our understanding of the viscosity of liquids of many compositions can lead to better models, and therefore easier processing, packaging, and consumption of fluids of various applications.

The rest of this chapter includes a summary of chapters 2-5 and a brief discussion of future work that will build on what I have learned from this work.

6.1 Summary

Chapter 2 is the first attempt to our knowledge of using configurational entropy (S^{conf}) theory to model the temperature dependence of the viscosity of honey. We showed that (1) S^{conf} modeling works exceedingly well for honeys and (2) that a viscosity model capable of modeling the effects of both temperature (T) and composition (X) is achievable using either the Adam-Gibbs or MYEGA equation.

Chapter 3 describes an improved implementation of the Tool-Narayanaswamy geospeedometer that reduces analytical time by roughly a factor of five, while also assessing uncertainties of natural cooling rates using Monte Carlo methods. Our algorithm *CoolMonte* will make relaxational geospeedometry a more accessible method allowing for cooling rate determination to be standard characterization procedure for naturally cooled volcanic glasses.

Chapters 4 and 5 represent case studies of two obsidian lavas that are similar in size and shape to the two most recent effusive eruptions of rhyolite magma at Chaitén in 2008-2009 and Cordón Caulle in 2011-2012. Banco Bonito is an obsidian coulée like the lava at Cordón Caulle. We found no evidence for some of the unique emplacement styles inferred during the eruption of Cordón Caulle preserved in samples collected from the VC-1 drill core, and suggest that secondary vesiculation, not intrusion of younger lava, is the most likely mechanism responsible for emplacement behaviors at Cordón Caulle. Obsidian Dome is an oblate lava like the effusive dome at Chaitén. We have found

evidence of at least two distinct emplacement styles at Obsidian Dome, like what was observed during the eruption of Chaitén. We have also identified continued water loss as an important process for modulating emplacement behaviors and therefore hazards.

6.2 Future Work

Relaxation geospeedometry with the help of *CoolMonte* allows the rapidly quantification of natural cooling rates of volcanic glasses. Experimentally determined cooling rates can be used to verify numerical cooling models and test assumptions about contributions of heat transfer processes including conduction, convection, and radiation. In chapters 4 and 5, we observed significant differences between predicted and experimental cooling rates, especially near the surfaces of Banco Bonito and Obsidian Dome. Experimentally determined near-surface cooling rates were much faster than those predicted by conduction alone, likely due to contributions of radiative and convective cooling at the surface.

Present lava cooling models include the effects of convective heat loss by assuming a constant between 10 to 150 W m^{-2} K^{-1}, for still and windy days. Future work should include convective heat loss experiments to model the effects of forced and free convection more appropriately on the surface cooling rates of lavas of different compositions, textures, and eruption temperatures. Results from these experiments could then be used to potentially reconcile the differences between experimentally determined natural cooling rates and numerical cooling models.

Discrepancies also exist between the predicted and observed cooling rates for the centers of Banco Bonito and Obsidian Dome, tens of meters away from the upper and

lower flow surfaces. Measured cooling rates sometimes imply hundreds of millions of years to cool from eruption temperature to ambient. These discrepancies are likely caused by the addition of latent heat of crystallization (ΔH_{cryst}) which buffers cooling potentially resulting in exceedingly slow cooling rates (e.g., ~10^{-13} K s^{-1}). Attempts were made to include ΔH_{cryst} in our cooling models, however, challenges emerged when trying to identify model crystallization rates, and therefore the appropriate amount of ΔH_{cryst} to include at any given time step. Future work should find a theoretical solution for including ΔH_{cryst} in rhyolitic melts, to reconcile differences between observed natural cooling rates, and those predicted with numerical models. Work will continue on *CoolMonte* to try and improve uncertainty estimates and test the algorithm on a wider range of lava compositions, including basalts from the 2018 eruption of Kilauea.

Lastly, additional measurements of well-characterized honeys are needed to build a predictive viscosity model for honey as a function of temperature (T) and composition (X).

Appendix

A. Code, example data, and supplementary information for *CoolMonte*

A. 1. Data vector, object function, and model parameters.

The input data vector is comprised of the normalized C_P and corresponding T values in K. The variable *iterations* defines the number of combinations of model parameters the user wants *CoolMonte* to output. Variables *lb* and *ub* define the lower and upper bounds of the parameter space. The first column corresponds to variable τ_0 (limiting relaxation time in $\log_{10}$ s), second is ΔH (relaxational enthalpy in kJ mol^{-1}), third is β, fourth is ξ, and the fifth column is cooling rate (q_c in K min^{-1}). Variable q_h is the experimental heating rate in K min^{-1}. The object function is equation 3.6.

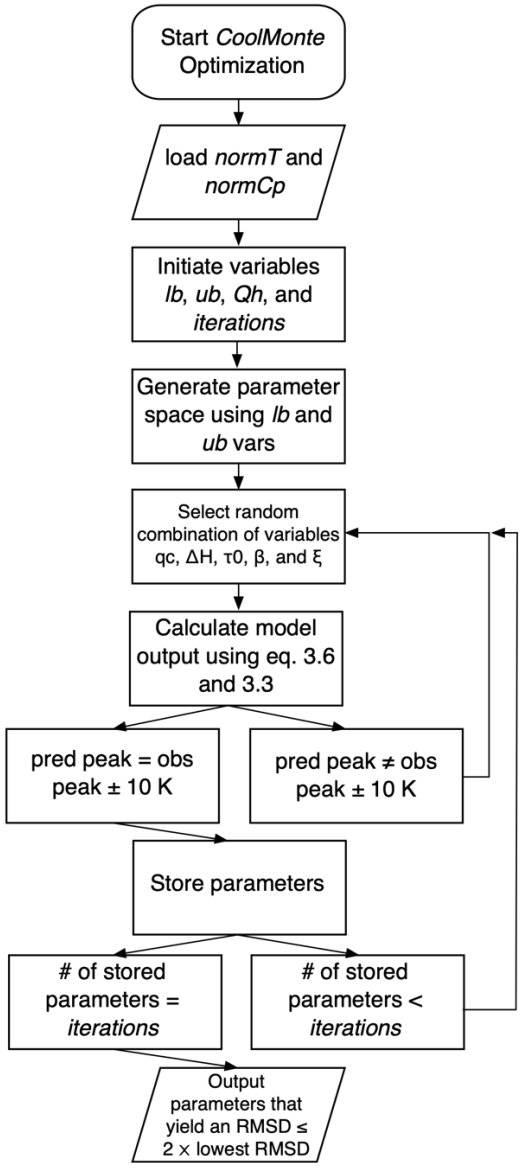

Figure A.1. Flow chart describing the operation of *CoolMonte*.

```
function [Qc, out, params_out] = CoolMonte(normT,normCp,Qh,lb,ub,iterations)
% CoolMonte (Kenderes and Whittington (2021) is a Monte Carlo inspired
% numerical solver for determining natural cooling rates of volcanic
% glasses.
% Updated March 17, 2021
%
% Input Variables:
% normT = Experimental temperature (K) for normalized Cp measurements
% normCp = normalized Cp values from experimental measurements (eq. 3)
% Qh = heating rate in K/min
% lb = lower boundary conditions where [tau0, dH, beta, xsi, qc]
% ub = upper boundary conditions where [tau0, dH, beta, xsi, qc]
%       tau0 = log10 s
%       dH   = kJ/mol
%       beta = 0 to 1
%       xsi  = 0 to 1
%       qc   = K/min
% iterations = the number of successful model permutations with peak
```

```
%       heights +/- 10∞C of the observed Tg peak before algorithm end.
%
% Output Variables:
% params_out = all successful model permutations where:
%       params_out(n,:) = [tau0, dh, beta, xsi, qc, RMSD]
%
% Final distributions are determined by reducing params_out
% out = permutations with RMSD's <= 2 times the lowest RMSD using the code:
% Qc = average cooling rates from 'out' in log10 K/s
%
% Estimated cooling rate (Qc) may vary between this code and the paper due to how
Monte Carlo
% methods function.

% Create a matrix of possible initial guesses based on the upper and lower
% bounds (lb and ub).
xlogA = lb(1):0.001:ub(1);
xkdH = lb(2):0.1:ub(2);
xbeta = lb(3):0.001:ub(3);
xxsi = lb(4):0.001:ub(4);
xQc = log10(abs(lb(5))):-0.001:log10(abs(ub(5)));
xQc = -1.*(10.^xQc);

% Identifies the temperature that corresponds to the largest normalized Cp
% value.
peakT = normT(find(normCp == max(normCp),1),1);

% index variables
[~,a] = size(xlogA);
[~,b] = size(xkdH);
[~,c] = size(xbeta);
[~,d] = size(xxsi);
[~,e] = size(xQc);

% initiates output variable 'params_out'
params_out = zeros(iterations,6);

% for loop continues until a number of model parameter permutations =
% iterations are identified and stored.
for i = 1:iterations
    sz = 0;
    while sz < 1
        x0 = [xlogA(1,randperm(a,1)) xkdH(1,randperm(b,1)) xbeta(1,...
            randperm(c,1)) xxsi(1,randperm(d,1)) xQc(1,randperm(e,1))];
        [Tc, Tfc, Th, Tfh] = Tf(10.^x0(1),1000.*x0(2),x0(4),x0(3),x0(5),Qh);
        [~, dTfdTh] = dTfdT(Tfc,Tc,Tfh,Th);
        peakT_pred = Th(find(dTfdTh == max(dTfdTh),1),1);
        pred = interp1(Th,dTfdTh,normT);
        x0(6) = sqrt(mean((pred-normCp).^2));
        l = (dTfdTh(25,1)-dTfdTh(1,1))/(Th(25,1)-Th(1,1));
        %r = (dTfdTh(801,1)-dTfdTh(775,1))/(Th(801,1)-Th(775,1));
        if peakT_pred <= peakT+10 && peakT_pred >= peakT-10 && l < 1e-7 ...
                && l > -1e-7 %&& r < 1e-7 && r > -1e-7
            sz = 1;
            params_out(i,:) = x0;
        else
        end
        params_out(i,:) = x0;
    end
end
clear params x0 l r rmsd pred peakT_pred

% Reduce params_out to only model permutations <= 2 times the lowest RMSD
params_out = sortrows(params_out,6);
out = find(params_out(:,6) <= 2.*params_out(1,6));
out = params_out(out,:);
Qc = mean(log10(abs(out(:,5)./60))); % in log10 K/s

% Alert for when the algorithm finishes running.
% load handel
% sound(y,Fs)
```

```
%%%%%%%%%%%%%%%%%%%%%%%%%%%%%%%%%%%%%%%%%%%%%%%%%%%%%%%%%%%%%%%%%%%%%%%%%%%%
% Nested functions called by CoolMonte

% Equation 3 from Kenderes and Whittington (2021) takes the
% numeric derivative of the fictive temperature as a function of
% temperature.
    function [dTfdTc, dTfdTh] = dTfdT(Tfc,Tc,Tfh,Th)
    sz = size(Tfc); sz = sz(1,1);
    for n = 1:1:sz
        if n == 1
           dTfdTc(n,1) = 1;
        else
           dTfdTc(n,1) = (Tfc(n,1)-Tfc(n-1,1))./((Tc(n,1)-Tc(n-1,1)));
        end
    end

    sz = size(Tfh); sz = sz(1,1);
    for n = 1:1:sz
        if n == 1
           dTfdTh(n,1) = 0;
        elseif n == sz
           dTfdTh(sz,1) = 1;
        else
           dTfdTh(n,1) = (Tfh(n,1)-Tfh(n-1,1))./((Th(n,1)-Th(n-1,1)));
        end
    end
    end

% Equation 4 from Kenderes and Whittington (2021)
% Non-exponential decay, stretched exponential, or Kohlrausch-Williams-Watts
% function for estimating time necessary for relaxation of glasses
% Updated March 7, 2021
    function [phi] = KWW(t,tau,beta)
    phi = exp(-((t./tau).^beta));
    end

% Equation 5 from Kenderes and Whittington (2021)
% Tool-Narayanaswamy function for estimating characteristic relaxation time
% (tau0) as a function of temperature (T,K) and the fictive temperature (Tf,K)
% accounts for the non-linearity of relaxation.
% Updated March 7, 2021
    function [tau] = TN(A,x,dH,T,Tf)

    HRT = dH/(8.31451*T);
    HRTf = dH/(8.31451*Tf);
    tau = A.*exp((x.*HRT)+((1-x).*HRTf));
    end

% Equation 6 from Kenderes and Whittington (2021)
% TN-Geospeedometer which models the evolution of the fictive temperature
% (Tf) as a function of temperature.
% Updated March 7, 2021
    function [Tc, Tfc, Th, Tfh] = Tf(A,dH,x,beta,Qc,Qh)

        % Assign Parameters

        Temph   = 1300;                          % K        "Starting temperature"
        Templ   = 500;                           % K        "ending temperature"

        % Cooling
        Qc        = Qc/60;          % K/s      "heating/cooling rate" - if cooling
        dTc       = -1;             % K        "temperature step"
        tc        = dTc/Qc;         % s        Convert KWW from Time to Temp
        Tc        = Temph:dTc:Templ; Tc = Tc'; % K
        Tfc       = Temph;
        tauc     = A.*exp((dH./(8.31451*Temph)).*x);
        phic      = (1-KWW(tc,tauc,beta));
        [sz,~]    = size(Tc);

            for n = 2:1:sz
                tauc(n,1)  = TN(A,x,dH,Tc(n,1),Tfc(n-1,1));
```

```
            phic(n,1)  = (1-KWW(tc,tauc(n,1),beta));
            DT         = (Tfc(n-1,1)-Tc(n,1))*phic(n,1);
            Tfc(n,1)   = Tfc(n-1,1)-DT;
        end

    % Heating
    Qh    = Qh/60;          % K/s      "heating/cooling rate" - if cooling -
    dTh   = dTc*-1;         % K        "temperature step"
    th    = dTh/Qh;         % s        Convert KWW from Time to Temp
    Th    = Templ:dTh:Temph; Th = Th'; % K
    Tfh   = Tfc(sz,1);
    tauh  = TN(A,x,dH,Th(1,1),Tfh);
    phih  = 1-KWW(th,tauh,beta);

        for n = 2:1:sz
            tauh(n,1) = TN(A,x,dH,Th(n,1),Tfh(n-1,1));
            phih(n,1) = (1-KWW(th,tauh(n,1),beta));
            DT        = (Tfh(n-1,1)-Th(n,1))*phih(n,1);
            Tfh(n,1)  = Tfh(n-1,1)-DT;
        end
    end
end
```

Figure A.2. Source code for *CoolMonte* written in MATLAB.

Bibliography

Adam, G., and Gibbs, J.H., 1965, On the temperature dependence of cooperative relaxation properties in glass-forming liquids: The Journal of Chemical Physics, v. 43, n. 1, p. 139-146, doi: 10.1063/1.1696442.

Andrews, G.D.M., Kenderes, S.M., Whittington, A.G., Isom, S.L., Brown, S.R., Pettus, H.D., Cole, B.G., and Gokey, K.J., 2021, The fold illusion: The origins and implications of ogives on silicic lavas: Earth and Planetary Science Letters, v. 553, n. 116643, p. 1-14, doi: 10.1016/j.epsl.2020.116643.

Angell, C.A., 1995, Formation of glasses from liquids and biopolymers: Science, v. 267, n. 5206, p. 1924-1935.

Angell, C.A., 1997, Entropy and fragility in supercooling liquids: Journal of Research of the National Institute of Standards and Technology, v. 102, n. 2, p. 171-185.

Al-Mahasneh, M.A, Rababah, T.M., Amer, M., & Al-Omoush, M., 2014, Modeling physical and rheological behavior of minimally processed wild flowers honey: Journal of Food Processing and Preservation, v. 38, p. 21-30 doi: 10.1111/j.1745-4549.2012.00734.x.

Avard, G., and Whittington, A.G., 2012, Rheology of arc dacite lavas: experimental determination at low strain rates: Bulletin of Volcanology, v. 74, p. 1039-1056, doi: 10.1007/s00445-012-0584-2.

Baldridge, W.S., Keller, G.R., Haak, V., Wendlandt, E., Jiracek, G.R., and Olsen, K.H., 2006, Chapter 6 The Rio Grande Rift: Developments in Geotectonics, v. 25, p. 233-275, doi: 10.1016/S0419-0254(06)80014-5.

Becker R., and Döring W., 1935, Kinetische Behandlung der Keimbildung in übersättigten Dämpfen. Annalen der Physik, v. 416, p. 719-752.

Behrens H., Tamic, N., Holtz, F., 2004, Determination of molar absorption coefficient for the IR absorption band of CO2 in rhyolitic glasses: American Mineralogist, v. 89, p. 301-306.

Bottinga, Y., and Weill, D.F., 1972, The viscosity of magmatic silicate liquids; a model calculation: The American Journal of Science, v. 272, n. 5, p. 438-475, doi: 10.2475/ajs.272.5.438.

Bragg, W., and Gibbs, R.E., 1925, The structure of α and β quartz: Proceedings of the Royal Society, v. 109, n. 751, p. 405-427.

Brugman, K.K., and Till, C.B., 2019, A low-aluminum clinopyroxene-liquid geothermometer for high-silica magmatic systems: American Mineralogist, v. 104, p. 996-1004, doi: 10.2138/am-2019-6842.

Carn, S.A., Pallister, J.S., Lara, L., Ewert, J.W., Watt, S., Prata A.J., Thomas, R.J., and Villarosa, G., 2009, The unexpected awakening of Chaitén volcano, Chile: Eos, v. 90, n. 24, p. 205-212.

Castro, J.M., and Dingwell, D.B., 2009, Rapid ascent of rhyolitic magma at Chaitén volcano, Chile: Nature, v. 461, n. 8, p. 780-784, doi: 10.1038/nature08458.

Castro, J.M., Bindeman, I.N., Tuffen, H., and Schipper, C.I., 2014, Explosive origin of silicic lava: textural and δD-H_2O evidence for pyroclastic degassing during rhyolite effusion: Earth and Planetary Science Letters, v. 405, p. 52-61.

Chataway, H.D., 1932, The determination of moisture in honey: Canadian Journal of Research, v. 6, n. 5, p. 532-547, doi: 10.1139/cjr32-041.

Chirife, J., and Buera, M.P., 1997, A simple model for predicting the viscosity of sugar and oligosaccharide solutions: Journal of Food Engineering, p. 33, n. 3-4, p. 221-226.

Cohen, I., and Weihs, D., 2010, Rheology and microrheology of natural and reduced-calorie Israeli honeys as a model for high-viscosity Newtonian liquids: Journal of Food Engineering, v. 100, p. 366-371, doi: 10.1016/j.jfoodeng.2010.04.023.

Cook, G.W., Wolff, J.A. and Self, S., 2016, Estimating the eruptive volume of a large pyroclastic body: the Otowi Member of the Bandelier Tuff, Valles caldera, New

Mexico: Bulletin of Volcanology, v. 78, n. 10, p. 2-11, doi: 10.1007/s00445-016-1000-0.

Cox, W.P., and Merz, E.H., 1958, Correlation of Dynamic and Steady Flow Viscosities: Journal of Polymer Science, v. 28, p. 619-622.

da Silva, V.M., Almeida, R.D., Filho, T., and Resende, J.V.D., 2017, Rheological properties of selected Brazilian honeys as a function of temperature and soluble solid concentration: International Journal of Food Properties, v. 20-S3, p. S2481-S2494, doi: 10.1080/10942912.2017.1370599.

Debenedetti P.G., 1996, Metastable Liquids, Princeton Univ., Princeton, N.J.

DeBolt, M.A., Easteal, A.J., Macedo, P.B., and Moynihan, C.T., 1976, Analysis of structural relaxation in glass using rate heating data: Journal of the American Ceramic Society, v. 59, n 1-2, p. 16-21.

Dingwell D.B., and Webb S.L., 1990, Relaxation in silicate melts. European Journal of Mineralogy, v. 2, p. 427-449.

Ditmars, D.A., Ishihara, S., Chang, S.S., and Bernstein, G., 1982, Enthalpy and heat-capacity standard reference material: Synthetic sapphire (α-Al2O3) from 10 to 2250 K: Journal of Research of the National Bureau of Standards, v. 87, n. 2, p. 159-163.

Eichelberger, J.C., Lysne, P.C., and Younker, L.W., 1984, Research drilling at Inyo Domes, Long Valley Caldera, California: Eos, v. 65, n. 39, p. 1-5.

Eichelberger J.C., Lysne P.C., Miller C.D., and Younker L.W., 1985, Research drilling at Inyo Domes, California: 1985 results. Eos, v. 66, n. 17, p. 1-3.

Eichelberger, J.C., Carrigan, C.R., Westrich, H.R., and Price R.H., 1986, Non-explosive silicic volcanism: Nature, v. 323, n. 16, p. 598-602.

Farquharson, J.I., James, M.R., and Tuffen, H., 2015, Examining rhyolite lava flow dynamics through photo-based 3D reconstructions of the 2011-2012 lava flowfield at Cordón-Caulle, Chile: Journal of Volcanology and Geothermal Research, v. 304, p. 336-348, doi: 10.1016/j.jvolgeores.2015.09.004.

Fawcett, P.J., Heikoop, J., Anderson, R., Hurley, L., Goff, F., Geissman, J.W., Johnson, C., Woldegabriel, G., Allen, C.D., Fessenden, J., 2006, Two mid-Pleistocene glacial cycles (MIS 14 to 10) from lacustrine sediments in the Valles Caldera, New Mexico: American Geophysical Union, Fall Meeting, Abstract PP51B-1137.

Fink, J.H., and Griffiths, R.W., 1998, Morphology, eruption rates, and rheology of lava domes: insights from laboratory models: Journal of Geophysical Research, v. 103, n. B1, p. 527-545.

Fink, J.H., and Manley, C.R., 1987, Origin of pumiceous and glassy textures in rhyolite flows and domes: Geological Society of America Bulletin, Special Paper 212, p. 77-88, doi: 10.1130/SPE212-p77.

Fulcher, G.S., 1925, Analysis of recent measurements of the viscosity of glasses: The Journal of the American Ceramics Society, v. 8, p. 339-355.

Giordano, D., Russell, J.K., and Dingwell, D.B., 2008, Viscosity of magmatic liquids: a model: Earth and Planetary Science Letters, v. 271, p. 123-134, doi: 10.1016/j.epsl.2008.03.038.

Goff, F., Rowley, J., Gardner, J.N., Hawkins, W., and Goff, S., 1986, Initial results from VC-1, first Continental Scientific Drilling Program core hole in Valles caldera, New Mexico: Journal of Geophysical Research, v. 91, n. B2, p. 1742-1752.

Gonnermann H.M., and Manga, M., 2003, Explosive volcanism may not be an inevitable consequence of magma fragmentation: Nature, v. 426, n. 27, p. 432-435.

Gottsmann J., and Dingwell D.B., 2001a, Cooling dynamics of spatter-fed phonolite obsidian flows on Tenerife, Canary Islands: Journal of Volcanology and Geothermal Research, v. 105, p. 323-342.

Gottsmann J., and Dingwell D.B., 2001, The cooling of frontal flow ramps: a calorimetric study on Rocche Rosse rhyolite flow, Lipari, Aeolian Islands, Italy: Terra Nova, v. 13, p. 157-164.

Gottsmann J., and Dingwell D.B., 2002, The thermal history of a spatter-fed lava flow: the 8-ka pantellerite flow of Mayor Island, New Zealand: Bulletin of Volcanology, v. 64, p. 410-422.

Gottsmann J., Giordano, D., and Dingwell, D.B., 2002, Predicting shear viscosity during volcanic processes at the glass transition: a calorimetric calibration: Earth and Planetary Science Letters, v. 198, p. 417-427.

Gottsmann J., Harris A.J.L., and Dingwell D.B., 2004 Thermal history of Hawaiian pahoehoe lava crusts at the glass transition: Implications for flow rheology and emplacement: Earth and Planetary Science Letters, v. 228, p. 343-353.

Harris, A.J.L., Flynn, L.P., Matías, O., Rose, W.I., 2002, The thermal stealth flows of Santiaguito dome, Guatemala: Implications for the cooling and emplacement of dacitic block-lava flows: GSA Bulletin, v. 114, n. 5, p. 533-546.

Hildreth, W. and Fierstein, J., 2017, Geologic Field-Trip guide to Long Valley Caldera, California: Scientific Investigations Report 2017-5022-L.

Hildreth, W. and Mahood, G.A., 1986, Ring-fracture eruption of the Bishop Tuff: GSA Bulletin, v. 97, p. 396-403.

Hildreth, W., and Wilson, C.J.N., 2007, Compositional zoning of the Bishop Tuff: Journal of Petrology, v. 48, n. 5, p. 951-999, doi: 10.1093/petrology/egm007.

Hon, K., Kauahikaua, J., Denlinger, R., and Mackay, K., 1994, Emplacement and inflation of pahoehoe sheet flows: Observations and measurements of active lava flows on Kilauea volcano, Hawaii: GSA Bulletin, v. 106, p. 351-370.

Hui H., Hess K-U., Zhang, Y., Nichols, A.R.L., Peslier, A.H., Lange R.A., Dingwell D.B., and Neal C.R., 2018, Cooling rates of lunar orange glass beads: Earth and Planetary Science Letters, v. 503, p. 88-94.

Junzheng, P., and Changying, J., 1998, General rheological model for natural honeys in China: Journal of Food Engineering, v. 36, p. 165-168.

Kenderes, S.M., and Whittington, A.G., 2021, Faster geospeedometry: A Monte Carlo approach to relaxational geospeedometry for determining natural cooling rates of volcanic glasses: Chemical Geology, v. 581, n. 120385, p. 1-12.

Kohlrausch R. (1854) Theorie des elektrischen Rückstandes in der Leidner Flasche: Annalen der Physik, v. 91, n. 1, p. 56-82 and 179-213.

Ku, H.H., 1966, Notes on the use of propagation of error formulas: Journal of Research of the National Bureau of Standards, v. 70C, n. 4, p. 263-273.

Kulmyrzaev, A., and McClements, D.J., 2000, High frequency dynamic shear rheology of honey: Journal of Food Engineering, v. 45, p. 219-224.

Lara, L., 2008, The 2008 eruption of the Chaitén Volcano, Chile: a preliminary report: Andean Geology, v. 36, n. 1, p. 125-129.

Lavallée Y., Wadsworth F.B., Vasseur J., Russell J.K., Andrews G.D.M., Hess K-U., von Aulock F.W., Kendrick J.W., Tuffen H., Biggin A.J., and Dingwell D.B., 2015, Eruption and emplacement timescales of ignimbrite super-eruptions from thermo-kinetics of glass shards: Frontiers in Earth Science, v. 3, p. 1-11, doi: 10.3389/feart.2015.00002

Lazaridou, A., Biliaderis, C.G., Bacandritsos, N., and Sabatini, A.G., 2004, Composition, thermal and rheological behavior of selected Greek honeys: Journal of Food Engineering, v. 64, p. 9-21, doi: 10.1016/j.jfoodeng.2003.09.007.

Leggett, T.N., Befus, K.S., and Kenderes, S.M., 2020, Rhyolite lava emplacement dynamics inferred from surface morphology: Journal of Volcanology and Geothermal Research, v. 395, n. 106850, p. 1-14.

Liu, Y., Zhang, Y., and Behrens, H., 2005, Solubility of H2O in rhyolitic melts at low pressures and a new empirical model for mixed H2O-CO2 solubility in rhyolitic

melts: Journal of Volcanology and Geothermal Research, v. 143, p. 219-235, doi: 10.1016/j.jvolgeores.2004.09.019.

Lothrop, R.E., 1939, The composition of honey and is utilization-relation of composition and viscosity: American Bee Journal, v. 79, p. 130-133.

Mader, H.M., Llewellin, E.W., and Mueller, S.P., 2013, The rheology of two-phase magmas: A review and analysis: Journal of Volcanology and Geothermal Research, v. 257, p. 135-158.

Magnall, N., James, M.R., Tuffen, H., and Vye-Brown, C., 2017, Emplacing a cooling-limited rhyolite lava flow: similarities with basaltic lava flows: Frontiers in Earth Science, v. 5, n. 44, doi: 10.3389/feart.2017.00044.

Magnall, N., James, M.R., Tuffen, H., Vye-Brown, C., Schipper, C.I., Castro, J.M., and Gerard Davies, A., 2018, The origin and evolution of breakouts in a cooling-limited rhyolite lava flow: GSA Bulletin, doi: 10.1130/B31931.1.

Magnani, M.B., 2004, The Yavapai-Mazatzal boundary: A long-lived tectonic element in the lithosphere of southwestern North America: GSA Bulletin, v. 116, n. 7/8, p. 1137-1142, doi: 10.1130/B25414.1.

Maier C.G., and Kelley K.K., 1932, An equation for the representation of high-temperature heat content data: Journal of the American Ceramic Society, v. 54, n. 8, p. 3243-3246, doi: 10.1021/ja01347a029.

Mangan, M., and Sisson, T., 2000, Delayed, disequilibrium degassing in rhyolite magma: decompression experiments and implications for explosive volcanism: Earth and Planetary Science Letters, v. 183, p. 441-455.

Manley, C.R., and Fink, J.H.,1987, Internal textures of rhyolite flows as revealed by research drilling: Geology, v. 15, p. 549-552.

Maxwell, J.C., 1867, On the dynamical theory of gases: Philosophical Transactions of the Royal Society of London, v. 157, p. 49-88.

Mauro, J.C., Yue, Y., Ellison, A.J., Gupta, P.K., and Allan, D.C., 2009, Viscosity of glass-forming liquids: Proceedings of the National Academies of Science, v. 106, n. 47, p. 19780-19784, doi: 10.1073/pnas.0911705106.

Merle, O., 1998, Internal strain within lava flows from analogue modelling: Journal of Volcanology and Geothermal Research, v. 81, p. 189-206.

Miller C.D., 1985, Holocene eruptions at the Inyo volcanic chain, California: Implications for possible eruptions in Long Valley caldera: Geology, v. 13, p. 14-17.

Milner, S., 1996, Relating the shear-thinning curve to the molecular weight distribution in linear polymer melts: Journal of Rheology, v. 40, p. 303-316.

Mossel, B., Bhandari, B., D'Arcy, B., and Caffin, N., 2000, Use of an Arrhenius model to predict rheological behavior in some Australian honeys: LWT – Food Science and Technology, v. 33, n. 8, p. 545-552, doi: 10.1006/fstl.2000.0714.

Moynihan C.T., Easteal A.J., and DeBolt M.A., 1976, Dependence of the fictive temperature of glass on cooling rate: Journal of the American Ceramics Society, v. 59, n. 1-2, p. 12-16.

Moynihan C.T., 1995, Structural relaxation and the glass transition in (eds.) Stebbins, J.F., McMillan, P.F., and Dingwell, D.B., Structure, Dynamics and Properties of Silicate Melts, Reviews in Mineralogy v. 32, Washington D.C.

Munro, J., 1943, The viscosity and thixotropy of honey: Journal of Economic Entomology, v. 36, n. 5, p. 769-777.

Narayanaswamy, O.S., 1971, A model of structural relaxation in glass: Journal of the American Ceramic Society, v. 54, n. 10, p. 491-498.

Narayanaswamy, O.S., 1988, Thermorheological simplicity in the glass transition: Journal of American Ceramic Society, v. 71, p. 900-904.

Neuville, D.R., & Richet, P., 1991, Viscosity and mixing in molten (Ca, Mg) pyroxenes and garnets. Geochimica et Cosmochimica Acta, v. 55, p. 1011–1019, doi: 10.1016/0016-7037(91)90159-3.

Newman, S., Stolper, E.M., and Epstein, S., 1986, Measurement of water in rhyolitic glasses: Calibration of an infrared spectroscopic technique: American Mineralogist, v. 71, p. 1527-1541.

Ni, H., and Zhang, Y., 2008, H2O diffusion models in rhyolitic melt with new high pressure data: Chemical Geology, v. 250, p. 68-78.

Nichols A.R.L., Potuzak M., and Dingwell D.B., 2009, Cooling rates of basaltic hyaloclastites and pillow lava glasses from the HSDP2 drill core. Geochimica et Cosmochimica Acta, v. 73, p. 1052-1066.

Oroian, M., Amariei, S., Escriche, I., and Gutt, G., 2013, Rheological aspects of Spanish honeys: Food Bioprocess Technology, v. 6, p. 228-241, doi: 10.1007/s11947-011-0730-4.

Pallister, J.S., Diefenbach, A.K., Burton, W.C., Muñoz, J., Griswold, J.P., Lara, L.E., Lowenstern, J.B., and Valenzuela, C.E., 2013, The Chaitén rhyolite lava dome: Eruption sequence, lava dome volumes, rapid effusion rates and source of the rhyolite magma: Andean Geology, v. 40, n. 2, p. 277-294.

Peleg, M., 2017, Temperature-viscosity models reassessed: Critical Reviews in Food Science and Nutrition. doi: 10.1080/10408398.2017.1325836.

Phillips, E. H., Goff, F., Kyle, P.R., McIntosh, W.C., Dunbar, N.W., and Gardner, J.N., 2007, The 40Ar/39Ar age constraints on the duration of resurgence at the Valles caldera, New Mexico: Journal of Geophysical Research, v. 112, n. B08201, doi: 10.1029/2006JB004511.

Potuzak M., Nichols A.R.L., Dingwell D.B., and Clague D.A., 2008, Hyperquenched volcanic glass from Loihi Seamount, Hawaii: Earth and Planetary Science Letters, v. 270, p. 54-62.

Rampp, M., Buttersack, C., and Lüdemann, H-D., 2000, T-dependence of the viscosity and the self-diffusion coefficients in some aqueous carbohydrate solutions: Carbohydrate Research, v. 328, p. 561-572.

Rantzsch U., Haber T., Klimm D., and Kloess G., 2013, The cooling rate of the El'gygytgyn impact glass: Meteoritics and Planetary Science, v. 48, n. 7, p. 1351-1358, doi: 10.1111/maps.12150.

Recondo, M.P., Elizalde, B.E., and Buera, M.P., 2006, Modeling temperature dependence of honey viscosity and of related supersaturated model carbohydrate systems: Journal of Food Engineering, v. 77, p. 126-134, doi: 10.1016/j.jfoodeng.2005.06.054.

Ren, M., and Parker, D.F., 2019, Composition variation and eruption dynamics of the El Cajete series, Valles caldera, New Mexico: International Journal of Earth and Environmental Sciences, v. 4, n. 163, p. 1-12, doi: 10.15344/2456-351X/2019/163.

Richet, P., 1984, Viscosity and configurational entropy of silicate melts: Geochimica et Cosmochimica Acta, v. 48, p. 471-483.

Richet, P., & Bottinga, Y., 1984, Anorthite, andesine, wollastonite, diopside, cordierite and pyrope: thermodynamics of melting, glass transitions, and properties of the amorphous phases: Earth and Planetary Science Letters, v. 67, p. 415-432.

Robert G., Smith, R.A., & Whittington, A.G., 2019, Viscosity of melts in the NaAlSiO4-KAlSiO4-SiO2 system: Configurational entropy modelling: Journal of Non-Crystalline Solids, v. 524, n. 119635, p. 1-20, doi: 10.1016/j.jnoncrysol.2019.119635.

Robie, R.A., and Hemingway, B.S., 1995, Thermodynamic properties of minerals and related substances at 298.15 K and 1 bar (105 Pascals) pressure and high temperature: USGS Bulletin, v. 2131, p. 1-89.

Romine W.L., Whittington A.G., Nabelek P.I., and Hofmeister A.M., 2012, Thermal diffusivity of rhyolitic glasses and melts: effects of temperature, crystals and

dissolved water: Bulletin of Volcanology, v. 74, p. 2273-2287, doi: 10.1007/s00445-012-0661-6.

Romine W.L., and Whittington A.G., 2015, A simple model for the viscosity of rhyolites as a function of temperature, pressure and water content: Geochimica et Cosmochimica Acta, v. 170, p. 281-300, doi: 10.1016/j.gca.2015.08.009.

Ross C.S., and Smith, R.L., 1955, Water and other volatiles in volcanic glasses: American Mineralogist, v. 40, n. 11-12, p. 1071-1089.

Rusiecka M.K., Bilodeau M., and Baker D.R., 2020, Quantification of nucleation delay in magmatic systems: experimental and theoretical approach: Contributions to Mineralogy and Petrology, v. 175, n. 47, p. 1-16, doi: 10.1007/s00410-020-01682-4.

Ryan, A.G., Russell, J.K., Hess, K-U, Phillion, A.B., and Dingwell, D.B., 2015, Vesiculation in rhyolite at low H2O contents: a thermodynamic model: Geochemistry, Geophysics, and Geosystems, doi: 10.1002/2015GC006024.

Schairer J.F., and Bowen N.L., 1956, The system Na2O-Al2O3-SiO2: American Journal of Science, v. 254, p. 129-195.

Scherer G.W., 1984, Use of the Adam-Gibbs equation in the analysis of structural relaxation: Journal of the American Ceramic Society, v. 67, n. 7, p. 504-511.

Schipper, C.I., Castro, J.M., Tuffen, H., James, M.R., and How, P., 2013, Shallow vent architecture during hybrid explosive-effusive activity at Cordón Caulle (Chile, 2011-12): Evidence from direct observations and pyroclast textures: Journal of Volcanology and Geothermal Research, v. 262, p. 25-37.

Sehlke, A., & Whittington, A.G., 2016, The viscosity of planetary tholeiitic melts: A configurational entropy model: Geochimica et Cosmochimica Acta, v. 191, p. 277-299, doi:10.1016/j.gca.2016.07.027.

Self, S., Keszthelyi, L., and Thordarson, Th., 1998, The importance of pahoehoe: Annual Review Earth and Planetary Science, v. 26, p. 81-110.

Shaw, H.R., 1972, Viscosities of magmatic silicate liquids: an empirical method of prediction: American Journal of Science, v. 272, p. 870-893.

Soesanto, T., and Williams, M.C., 1981, Volumetric interpretation of viscosity of concentrated and dilute sugar solutions: Journal of Physical Chemistry, v. 85, p. 3338-3341.

Sopade, P.A., Halley, P., Bhandari, B., D'Arcy, B., Doebler, C., and Caffin, N., 2002, Application of the Williams-Landel-Ferry model to the viscosity-temperature relationship of Australian honeys: Journal of Food Engineering, v. 56, p. 67-75.

Steffe, J.F., 1992, Introduction to Rheology. In Food Processing Engineering (p. 10). East Lansing, MI, Freeman Press.

Stevenson R. J., Dingwell, D.B., Webb, S.L., and Bagdassarov, N.S., 1995, The equivalence of enthalpy and shear stress relaxation in rhyolitic obsidians and quantification of the liquid-glass transition in volcanic processes: Journal of Volcanology and Geothermal Research, v. 68, p. 297-306.

Stevenson R. J., Bagdassarov N. S., Dingwell D. B., and Romano C., 1998, The influence of trace amounts of water on the viscosity of rhyolites: Bulletin of Volcanology, v. 60, p. 89–97.

Stolper, E., 1982, Water in silicate glasses: an infrared spectroscopic study: Contributions to Mineralogy and Petrology, v. 81, p. 1-17.

Tammann, G. & Hesse, W., 1926, Die abhängigkeit der viscosität von der temperature bie unterkühlten flüssigkeiten: Zeitschrift für anorganische und allegmeine Chemie, v. 156, p. 245-257.

Taylor, B.E., Eichelberger, J.C., and Westrich, H.R., 1983, Hydrogen isotopic evidence of rhyolitic magma degassing during shallow intrusion and eruption: Nature, v. 306, n. 8, p. 541-545.

Telis, V.R.N., Telis-Romero, J., Mazzotti, H.B., and Gabas, A.L., 2007, Viscosity of aqueous carbohydrate solutions at different temperatures and concentrations: International Journal of Food Properties, v. 10, n. 1, p. 185-195, doi: 10.1080/10942910600673636.

Tool A.Q., 1946, Relation between inelastic deformability and thermal expansion of glass in its annealing range: Journal of the American Ceramic Society, v. 29, p. 240-253.

Toplis M.J., Dingwell, D.B., Hess, K-U., & Lenci, T., 1997, Viscosity, fragility, and configurational entropy of melts along the join SiO2-NaAlSiO4: American Mineralogist, v. 82, p. 979-990.

Toplis, M., 1998, Energy barriers to viscous flow and the prediction of glass transition temperatures of molten silicates: American Mineralogist, v. 83, p. 480-490.

Turnbull D. and Fisher J.C., 1949, Rate of nucleation in condensed systems. Journal of Chemical Physics, v. 17, p. 71-73.

Tuffen, H., Dingwell, D.B., and Pinkerton, H., 2003, Repeated fracture and healing of silicic magma generate flow banding and earthquakes? Geology, v. 31, n. 12, p. 1089-1092.

Tuffen, H., James, M.R., Castro, J.M., and Schipper, C.I., 2013, Exceptional mobility of an advancing rhyolitic obsidian flow at Cordón Caulle volcano in Chile: Nature Communications, v. 4, n. 2709, p. 1-7, doi: 10.1038/ncomms3709.

Urbain, G., Bottinga, Y., & Richet, P. (1982). Viscosity of liquid silica, silicates and alumino-silicates. Geochimica et Cosmochimica Acta, 46-6, 1061-1072.

Ventura, G., 2004, The strain path and kinematics of lava domes: An example from Lipari (Aeolian Islands, Southern Tyrrhenian Sea, Italy): Journal of Geophysical Research, v. 109, n. B01203, doi: 10.1029/2003JB002740.

Vogel, D.H., 1921, Temperaturabhängigkeitsgesetz der viskosität von flüssigkeiten. Physikalische Zeitschrift, v. 22, p. 645-646.

Vogel T.A., Eichelberger, J.C., Younker, L.W., Schuraytz, B.C., Horkowitz, J.P., Stockman, H.W., and Westrich, H.R., 1989, Petrology and emplacement dynamics of intrusive and extrusive rhyolites of Obsidian Dome, Inyo Craters volcanic chain, eastern California: Journal of Geophysical Research, v. 94, n. B12, p. 17937-17956.

Volmer M. and Weber A.Z., 1926, Nucleus formation in supersaturated systems: Zeitschrift für Physikalische Chemie, v. 119, p. 277-301.

Wadsworth, F.B., Llewellin, E.W., Vasseur, J., Gardner, J.E., and Tuffen, H., 2020, Explosive-effusive volcanic eruption transitions caused by sintering: Science Advances, v. 6, p. 1-7.

Walker, G.P.L., 1972, Compound and simple lava flows and flood basalts: Bulletin Volcanologique, v. 35, n. 3, p. 579-590.

Webb S.L., 1992, Shear, volume, enthalpy, and structural relaxation in silicate melts: Chemical Geology, v. 96, p. 449-457.

White, J.W., 1975, Composition of honey. In Crane, E., (Ed.), Honey: a Comprehensive Survey (p. 157-206). Heinemann, London.

White, J.W., 1978, Honey: Advances in Food Research, v. 24, 287-374.

Whittington, A.G., Bouhifd, M.A., & Richet, P., 2009, The viscosity of hydrous NaAlSi3O8 and granitic melts: Configurational entropy models: American Mineralogist, v. 94, p. 1-16.

Whittington A.G., Hellwig B.M., Behrens H., Joachim B., Stechern A., and Vetere F., 2009, The viscosity of hydrous dacitic liquids: implications for the rheology of evolving silicic magmas: Bulletin of Volcanology, v. 71, p. 185-199, doi: 10.1007/s00445-008-0217-y.

Whittington A.G., Richet P., and Polian A., 2012, Water and the compressibility of silicate glasses: A Brillouin spectroscopic study: American Mineralogist, v. 97, p. 455-467.

Wilding, M.C., Webb, S.L., and Dingwell, D.B., 1995, Evaluation of a relaxation geospeedometer for volcanic glasses: Chemical Geology, v. 125, p. 137-148.

Wilding M., Webb S., Dingwell D., Ablay G., and Marti J., 1996a, Cooling rate variation in natural volcanic glasses from Tenerife, Canary Islands: Contributions to Mineralogy and Petrology, v. 125, p. 151-160.

Wilding M., Webb S., Dingwell D.B., 1996b, Tektite cooling rates: Calorimetric relaxation geospeedometry applied to a natural glass: Geochimica et Cosmochimica Acta, v. 60, n. 6, p. 1099-1103.

Wilding M., Dingwell D., Batiza R., and Wilson L., 2000, Cooling rates of hyaloclastites: applications of relaxation geospeedometry to undersea volcanic deposits: Bulletin of Volcanology, v. 61, p. 527-536.

Wilding M.C., Smellie J.L., Morgan S., Lesher C.E., and Wilson L., 2004, Cooling process recorded in subglacially erupted rhyolite glasses: Rapid quenching, thermal buffering, and the formation of meltwater: Journal of Geophysical Research, v. 109, n. B08201, p. 1-13, doi: 10.1029/2003JB002721.

Williams, M.L., Landel, R.F., & Ferry, J.D., 1955, The temperature dependence of relaxation mechanisms in amorphous polymers and other glass-forming liquids: Journal of the American Chemical Society, v. 77, p. 3701-3707, doi: 10.1021/ja01619a008.

Williams G., and Watts D.C., 1969, Non-symmetrical dielectric relaxation behavior arising from a simple empirical decay function: Transactions of the Faraday Society, v. 66, p. 80-85.

Wisniewski, P.A., and Pazzaglia, F.J., 2002, Epeirogenic controls on Canadian River incision and landscape evolution, Great Plains of northeastern New Mexico: The Journal of Geology, v. 110, p. 437-456.

Wolff J.A., Brunstad K.A., and Gardner J.N., 2011, Reconstruction of the most recent volcanic eruptions from the Valles caldera, New Mexico: Journal of Volcanology and Geothermal Research, v. 199, p. 53-68.

Wolff, J.A., and Ramos, F.C., 2014, Processes in caldera-forming high-silica rhyolite magma: Rb-Sr and Pb isotope systematics of the Otowi Member of the Bandelier Tuff, Valles, Caldera, New Mexico, USA: Journal of Petrology, v. 55, n. 2, p. 345-375, doi: 10.1093/petrology/egt070.

Yanniotis, S., Skaltsi, S., and Karaburnioti, S., 2006, Effect of moisture content on the viscosity of honey at different temperatures: Journal of Food Engineering, v. 72, p. 372-377, doi: 10.1016/j.jfoodeng.2004.12.017.

Yue, Y.Z., 2009, The iso-structural viscosity, configurational entropy and fragility of oxide liquids. Journal of Non-Crystalline Solids, v. 355, p. 737-744.

Yue Y.Z., Christiansen J.deC., and Jensen S.L., 2002, Determination of the fictive temperature for a hyperquenched glass: Chemical Physics Letter, v. 357, p. 20-24.

Zaitoun, S., Ghzawi, A.A-M., Al-Malah, K.I.M., and Abu-Jdayil, B., 2001, Rheological properties of selected light colored Jordanian honey: International Journal of Food Properties, v. 4, n. 1, p. 139-148, doi: 10.1081/JFP-100002192.

Zhang, Y., Belcher, R., Ihinger, P.D., Wang, L., Xu, Z., and Newman, S., 1997, New calibration of infrared measurement of dissolved water in rhyolitic glasses: Geochimica et Cosmochimica Acta, v. 61, n. 15, p. 3089-3100.

Zimmerer, M.J., Lafferty, J., and Coble, M.A., 2016, The eruptive and magmatic history of the youngest pulse of volcanism at the Valles caldera: Implications for successfully dating late Quaternary eruptions: Journal of Volcanology and Geothermal Research, v. 310, p. 50-57, doi: 10.1016/j.jvolgeores.2015.11.021.

Vita

Stuart Michael Kenderes was born in Dearborn, MI, raised in Independence, KY, is the product of the American public school system, and the first in his family to pursue a Ph.D. He attended Western Kentucky University where he started as a political science major before graduating with honors with a degree in Geology. He attended Illinois State University's field camp and completed a Keck Geology Consortium research experience for undergraduates with Drs. David H. Malone (ISU) and John P. Craddock (Macalester), focused on an enigmatic igneous rock that was spatially and temporally related to the Heart Mountain Detachment. After graduation he worked for a small consulting company exploring for domestic fluorite resources in the Illinois-Kentucky fluorite district. After two cycles of graduate school applications, he was admitted from the waitlist to the University of Missouri where he started his master's degree under advisement of Dr. Martin Appold. The subject of his master's thesis was to measure the concentration of fluorine in fluid inclusions hosted in sphalerite from the Illinois-Kentucky fluorite district. While completing his master's degree, Stuart worked for one year at the Illinois State Geological Survey under the supervision of Shane Butler, F. Brett Denny, Joe Devera, and Mary Seid. Stuart began his doctoral research with Dr. Alan Whittington in the fall of 2016.

Stuart will be moving to Bloomington, IN with his wife and cat named Sid and will *hopefully* be starting a post doc at IUPUI with Dr. Catharine Macris in the fall.